eXPRESS Polymer Letters Vol.7, No.8 (2013) 651
Available online at www.expresspolymlett.com
DOI: 10.3144/expresspolymlett.2013.61

Editorial corner – a personal view

Medical plastics: Serving healthcare

P. Krawczak[*]

Department of Polymers and Composites Technology & Mechanical Engineering, Ecole Nationale Supérieure des Mines de Douai, 941 rue Charles Bourseul, CS 10838, 59508 DOUAI, France

Recently, plastics containing phtalates and bisphenol A have been criticized for their possible toxicity and harmful effect on human health. To be fair, it is worth underlining that healthcare industry also takes huge benefits from plastics. The promising potential of polymers was identified a long time ago and is actually not denied.

Plastics are commonly used for a wide range of medical applications such as surgical implants, bioresorbable items (closures, tissue patches and scaffolding …), tubing (heart and brain catheters …) or packaging (sterile barriers to gases and fluids, protection from touch and airborne contamination …). Besides, polymeric materials allow progress in medical devices development (blood containers, inhalers ...) and drug delivery. For instance, plastics may be ideal candidates for replacing metal in minimally invasive medical devices, compatible with medical imaging thanks to their X-ray transparency and nonmagnetic properties. Also, polymeric foams are used to manufacture oral drug delivery systems that are expected to increase the pharmaceutical ingredients' release rate. Novel bioresorbable, edible and non toxic biopolymers allow active ingredients such as beneficial bacteria to be administered orally as food components. New polymers resistant to bacterial attachment (stopping biofilm formation), therefore able to prevent hospital-acquired infections, are in the research stage. Several other examples could be mentioned, such as innovative polymer systems with outstanding retention of aesthetic and mechanical properties after repeated sterilization. However, in medical/healthcare applications as in other high-tech domains, the challenge is also to reconcile competing complex requirements, to face growing demands on performance and quality while keeping cost-efficiency. Here, new manufacturing technologies or optimised equipments and processes are helping to achieve tight precision, down-sizing of parts, elimination of assembly labour costs, or warrant increased production speed or better process reliability. At last, as medical plastics are often quite expensive, design of products and devices using the least material possible is also an issue.

In spite of ever more stringent regulations and requirements for marketing authorization, medical technology and healthcare industry undoubtedly constitute an attractive business field, offering interesting high added-value outlets for the plastics industry, and a fertile ground for scientists and engineers.

Prof. Dr. Patricia Krawczak
Member of International Advisory Board

---

[*] Corresponding author, e-mail: patricia.krawczak@mines-douai.fr

eXPRESS Polymer Letters Vol.7, No.8 (2013) 652–666
Available online at www.expresspolymlett.com
DOI: 10.3144/expresspolymlett.2013.62

Viscoelastic behaviour and fracture toughness of linear-low-density polyethylene reinforced with synthetic boehmite alumina nanoparticles

D. Pedrazzoli[1], R. Ceccato[1], J. Karger-Kocsis[2,3], A. Pegoretti[1]*

[1]University of Trento, Department of Industrial Engineering and INSTM Research Unit, Via Mesiano 77, 38123 Trento, Italy
[2]MTA–BME Research Group for Composite Science and Technology, Muegyetem rkp. 3., H-1111 Budapest, Hungary
[3]Department of Polymer Engineering, Faculty of Mechanical Engineering, Budapest University of Technology and Economics, Műegyetem rkp. 3., H-1111 Budapest, Hungary

Received 1 March 2013; accepted in revised form 14 April 2013

Abstract. Aim of the present study is to investigate how synthetic boehmite alumina (BA) nanoparticles modify the viscoleastic and fracture behaviour of linear low-density polyethylene. Nanocomposites containing up to 8 wt% of untreated and octyl silane-functionalized BA nanoparticles, were prepared by melt compounding and hot pressing.

The BA nanoparticles were finely and unformly dispersed within the matrix according to scanning electron microscopy inspection. The results of quasi-static tensile tests indicated that nanoparticles can provide a remarkable stiffening effect at a rather low filler content. Short term creep tests showed that creep stability was significatively improved by nanofiller incorporation. Concurrently, both storage and loss moduli were enhanced in all nanocomposites, showing better result for surface treated nanoparticles.

The plane-stress fracture toughness, evaluated by the essential work of fracture approach, manifested a dramatic increase (up to 64%) with the BA content, with no significant differences among the various types of BA nanoparticles.

Keywords: *nanocomposites, fracture and fatigue, mechanical properties, thermal properties*

1. Introduction

Increasing efforts are devoted to the research of thermoplastic nanocomposites exhibiting improved and novel properties. Most of these studies are focused on the investigation of correlations between structural features and mechanical properties. A large body of research has been developed on polar nanofillers (such as silicas, metal oxides, metal salts, layered silicates, etc.) which have been successfully added to thermoplastic matrices in order to improve their thermal, mechanical and rheological performances [1–8]. On the other hand, these nanofillers are generally poorly dispersed in apolar thermoplastics (such as polyolefins), thus limiting the beneficial effects of nanofiller addition on the thermo-mechanical properties. Different strategies have been adopted in order to improve the dispersability of polar nanofillers, such as the direct incorporation of the filler during the in-situ synthesis of the polymer [9], the addition of the filler during melt mixing [10, 11] or the dispersion of the filler by solution techniques [12]. However, in order to attain a qualitatively fine dispersion of the nanofiller within the matrix, a surface treatment of the filler should be considered [13–15], or a polymeric compatibilizer should be added during melt mixing [5, 16–19].

Due to its combination of low cost, high chemical resistance and relatively good mechanical proper-

---

*Corresponding author, e-mail: alessandro.pegoretti@unitn.it ties, polyethylene is one of the most largely used polyolefin. In particular, linear low-density polyethylene (LLDPE) is widely used for film production in the packaging industry, especially because of its high tear and impact strength [20]. Dorigato *et al.* [2, 21, 22] studied the effect of various kinds of amorphous silica nanoparticles on the viscoelastic and fracture behaviour of LLDPE based composites. Elastic moduli of the prepared composites resulted to be strictly related to the surface area of the filler rather than by its dimensions. Tensile properties at yield and at break increased with the surface area of the nanofiller and were positively affected by the presence of an organosilane on the surface of the nanoparticles. Furthermore, the application of the essential work of fracture (EWF) approach showed that the introduction of fumed silica nanoparticles produced an evident toughening [22]. Moreover, it has been also proven that the addition of surface treated silica particles to a polypropylene matrix can lead to a certain improvement of the thermo-mechanical properties of the matrix itself and a remarkable increase of the fiber/matrix adhesion when E-glass fibers are added [23].

Boehmite (BA) with chemical composition AlO(OH) is a quite inexpensive mineral component of the aluminum ore bauxite. It can also be produced synthetically in particulates with different aspect ratios. Their primary particle size is in the range of tens of nanometers. The recent interest for using BA fillers to produce thermoplastic nanocomposites is fuelled by the fact that they can be finely dispersed on nanoscale by both traditional and water-assisted melt compounding techniques [24–30].

The present work aims at investigating the effect of BA addition on the viscoelastic behaviour of LLDPE. Particular emphasis has been devoted to the study of the fracture toughness evaluated by the EWF approach.

2. Experimental section

2.1. Materials and samples preparation

The matrix used in this work was a Flexirene® CL10 linear low-density polyethylene (MFI at 190°C and 2.16 kg = 2.6 g/10 min, M_n = 27 000 g·mol^{-1}, density = 0.918 g·cm^{-3}), produced by Versalis S.p.A. (Mantova, Italy) using Ziegler-Natta catalysis and butene as a comonomer (C_4-LLDPE). This type of linear low density polyethylene, containing antioxidants, is suitable for cast extrusion of thin films with high optical properties.

Two different grades of untreated BA, namely Disperal® 40 (BA-D40) and Disperal® 80 (BA-D80) (supplied by Sasol GmbH, Hamburg, Germany) were used as fillers. Their nominal primary crystallite sizes are 40 and 72 nm, respectively (Table 1). Moreover, a silane surface treated BA (Disperal® 40 octylsilane treated, BA-D40 OS), characterized by the same primary crystallite size as Disperal® 40 was also used.

LLDPE chips were used as received while the BA fillers were dried at 80°C for 12 h prior to use. The samples were prepared by melt compounding in a Brabender® Plasti-Corder internal mixer (T = 170°C, n = 50 rpm, t = 15 min) followed by compression moulding using a Collin® P200E hot press (T = 170°C, P = 2 MPa, t = 15 min), to shape square plane sheets with a thickness of about 0.5 mm. The filler content was varied between 0 and 8 wt%.

The unfilled matrix was denoted as LLDPE, while the coding of the nanocomposites indicated the matrix, the filler type, and the filler weight amount, as well. For instance, a sample filled with 4 wt% of Disperal® 40 is coded as LLDPE-D40-4.

2.2. Experimental techniques

2.2.1. Filler characterization

Density measurements were carried out through a helium pycnometer (Micromeritics® Accupyc 1330,

Table 1. Physical properties of BA nanoparticles utilized in this work

Filler	Density[a] [g·cm^{-3}]	BET surface area[b] [m^2·g^{-1}]	Particle size d50[b] [µm]	Crystallite size[c] [nm]
BA–D40	3.007±0.004	105.0	50	38
BA–D40 OS	3.010±0.025	105.0	50	40
BA–D80	3.018±0.004	88.0	80	72

[a] Measurements were performed by using a Micromeritics Accupy® 1330 helium pycnometer (T = 23°C).

[b] Khumalo VM, Karger-Kocsis J., Thomann R.: Polyethylene/synthetic boehmite alumina nanocomposites: Structure, thermal and rheological properties. eXPRESS Polymer Letters. 2010, **4**(5):264–274.

[c] Measurements were performed by XRD analyses and applying the Sherrer equation.

Note that BET surface area, primary particle size and crystallite size of BA-D40 OS were assumed to be the same of BA-D40 due to lack of information in the datasheet.

Norcross USA), at a temperature of 23°C, in a testing chamber with a volume of 3.5 cm^3.

X-Ray diffraction measurements on BA powders were performed by a Rigaku® 3D Max X-ray diffractometer, scanning the samples in a 2θ range between 3 and 67°, at a 2θ step of 0.1°. The wavelength of the X-ray source was 0.1541 nm.

2.2.2. Spectroscopy analyses

Cryogenic fracture surfaces of unfilled LLDPE and LLDPE nanocomposites were observed at various magnifications by using a Zeiss Supra 40 (Berlin, Germany) field emission scanning electron microscope (FESEM), at an acceleration voltage between 1 and 2 kV.

IR spectroscopy was performed on the nanofillers and on 80 µm thick nanocomposite films in a wave number interval between 650 and 4000 cm^{-1}, setting a resolution of 2 cm^{-1} for a total number of 64 co-added scans.

2.2.3. Diffraction analysis

X-ray diffraction analysis was performed through a Rigaku® 3D Max powder diffractometer, in Bragg-Brentano geometry, using CuK_α radiation (0.1541 nm) and a curved graphite monochromator in the diffracted beam. Typical scans adopted the following parameters: 2θ range between 3 and 67°, sampling interval 0.1°, counting time 4 s.

2.2.4. Rheology measurements

Melt rheology of neat LLDPE and of nanocomposites was analyzed by a Rheoplus MCR 301 rheometer (Anton Paar Physics, Ostfildern, Germany) under controlled strain conditions. The test geometry was cone-plate (cone angle = 1°) with a diameter of the plates of 25 mm. Compression molded disks of around 0.6 mm thickness were placed between the plates at 180°C. The gap width was set to 0.5 mm by squeezing the LLDPE disk. Frequency sweep tests were carried out at 180°C. During the measurement a small amplitude (1%) oscillatory shear was applied to the samples. The storage and loss shear moduli (G' and G'', respectively) and the dynamic viscosity $|\eta^*|$ were measured as a function of angular frequency (ω) in the range 0.01–100 rad/s.

2.2.5. Thermal analyses

Differential scanning calorimetry (DSC) tests were carried out by a DSC Q2000 (TA Instruments-Waters LLC, New Castle, USA) differential scanning calorimeter under a constant nitrogen flow of 50 $ml\cdot min^{-1}$. Samples were heated up to 200°C at a rate of $10°C\cdot min^{-1}$ and cooled to 0°C at a cooling rate of $10°C\cdot min^{-1}$. A second heating scan was then performed at $10°C\cdot min^{-1}$. The melting enthalpy of 100% crystalline polyethylene has been considered equal to $\Delta H^0 = 290\ J\cdot g^{-1}$ [31]. The crystallinity χ_c of nanocomposite samples was estimated by taking the weight fraction of LLDPE in the composites into account. The melting temperatures T_{m1} and T_{m2} were recorded during the first and second heating scan, respectively. The crystallization enthalpy ΔH_c was measured by integrating the heat flow curve during the cooling scan.

Thermogravimetric analyses (TGA) were carried out through a Q5000 IR thermogravimetric analyzer (TA Instruments-Waters LLC, New Castle, USA) imposing a temperature ramp between 40 and 700°C at a heating rate of $10°C\cdot min^{-1}$ under a constant nitrogen flow of 25 $ml\cdot min^{-1}$.The onset of degradation temperature ($T_{d,onset}$) was determined by the point of intersection of the tangents to the two branches of the thermogravimetric curve, while the maximum rate of degradation temperature ($T_{d,max}$) was determined from the peak maxima in the first derivative of weight loss curve.

2.2.6. Mechanical tests

Uniaxial tensile tests were performed with an Instron® 4502 (Norwood, USA) tensile machine on samples of at least five ISO 527 type 1BA specimens. The tests were carried out at a crosshead speed of 0.25 $mm\cdot min^{-1}$ up to a maximum axial deformation of 1%. The strain was recorded by using a resistance extensometer Instron® model 2620-601 with a gage length of 12.5 mm. In accordance to ISO 527 standard, the elastic modulus was measured as a secant value between deformation levels of 0.05 and 0.25%. Uniaxial tensile properties, such as stress at yield (σ_y), stress at break (σ_b) and strain at break (ε_b) were determined at a higher crosshead speed (50 $mm\cdot min^{-1}$) without extensometer.

Dynamic mechanical thermal analysis (DMTA) was carried out with a DMA Q800 testing machine (TA Instruments®-Waters LLC, New Castle, USA) on rectangular specimens 25 mm long, 5 mm wide and 0.5 mm thick. The samples were analyzed over a temperature range between –130 and 80°C, imposing a heating rate of $3°C\cdot min^{-1}$ and a frequency of

1 Hz. A preload of 0.2 MPa and a maximum strain of 0.05% were set for each test. The most important viscoelastic functions (E', E'', $\tan\delta$) were recorded at different temperatures. By the same apparatus, short term (3600 s) tensile creep tests at 30°C were also performed at a constant applied stress (σ_0) of 1 MPa (i.e 10% of the stress at yield of unfilled LLDPE).

The plane stress fracture toughness of neat LLDPE and nanocomposites was assessed through the essential work of fracture (EWF) method under tensile conditions. According to this approach [32], the total fracture energy (W_f) spent to bring a pre-cracked body to complete failure can be partitioned into an essential work (W_e) required in the fracture zone to create new fracture surfaces and a non-essential work (W_p) dissipated in the outer plastic zone and required to yield the material. It can be easily derived that the essential work of fracture should be proportional to the ligament length (L), whereas the non-essential work of fracture should be proportional to L^2 see Equation (1):

$$W_f = W_e + W_p = w_f \cdot L \cdot B = w_e \cdot L \cdot B + w_p \cdot \beta \cdot L^2 \cdot B \qquad (1)$$

which can be written as shown by Equation (2):

$$w_f = w_e + \beta \cdot w_p \cdot L \qquad (2)$$

where B is the specimen thickness, β is a shape factor, w_e is the specific essential work of fracture, w_p is the specific non-essential work of fracture. The quantities w_e and $\beta \cdot w_p$ are determined by a linear interpolation of a series of experimental data of w_f obtained by testing specimens having different ligament lengths. The quantity w_p can be explicitly deduced for some shapes of the outer plastic zone with known β e.g., for circular, elliptical and diamond-type zones β is given by $\pi/4$, $\pi \cdot h/(4L)$, and $h/(2L)$, respectively, where h is the height of the corresponding zone [33].

Furthermore, the specific total work of fracture (w_f, see Equation (3)) can be divided into a specific work of fracture for yielding (w_y) and a specific work of necking (w_n) [33]:

$$w_f = w_y + w_n = (w_{e,y} + \beta' \cdot w_{p,y} \cdot L) + (w_{e,n} + \beta'' \cdot w_{p,n} \cdot L) \qquad (3)$$

Double-edge-notched-tensile (DENT) specimens (width 30 mm, height 80 mm, thickness 0.5 mm, distance between the grips 50 mm) were tested with an Zwick® Z005 tensile machine. At least four tests were conducted for every ligament length, and five different ligament lengths between 5 and 13 mm were tested at a crosshead speed of 10 mm·min^{-1}. The notches were prepared by using a home-made apparatus mounting a razor blade, in order to obtain a very sharp crack tip. From SEM images it was possible to estimate an average crack tip radius of less than 20 µm. The exact ligament lengths were measured with a profile projector with an accuracy of 0.01 mm.

In order to study the fracture behaviour of the material at high strain rate levels, tensile impact tests were carried out with a CEAST® (Norwood, USA) tensile impact instrumented pendulum. A striker of mass 3.65 kg and initial angular position of 63° reached an impact speed of 2 m·s^{-1} and a total impact energy of 7.3 J. Specific tensile energy to break (TEB) was obtained by Equation (4):

$$TEB = \frac{1}{A}\left[V_0 \int_0^{\mathrm{tr}} F\mathrm{d}t - \frac{1}{2m}\left(\int_0^{\mathrm{tr}} F\mathrm{d}t\right)^2\right] \qquad (4)$$

where A is the cross section of the specimen, m is the striker mass and V_0 is the impact speed.

3. Results and discussion

3.1. Morphology

SEM pictures taken from the cryogenic surfaces of LLDPE composites with 4 wt% BA are represented in Figure 1. The nanofiller appears quite homogeneously dispersed in the case of LLDPE-D40-4 composite, altough some agglomerates are clearly recognizable. On the other hand, the silane coupling agent present on the surface of BA D40 OS nanoparticles does not seem to affect the filler dispersion in the polymer matrix (Figure 1b). Similar finding was recently reported on the BA dispersion in poly(ε-caprolactone) [34]. As already observed by Brostow *et al.* [35], although the dispersion is not affected by the surface treatment of BA nanoparticles, a better polymer–filler interaction takes place due to replacement of hydroxide surface groups of the nanoparticles with organic ones. The hypothesis of an improved adhesion is consistent with the increment of the mechanical performance as reported later. In the case of LLDPE-D40 OS nanocomposites, wetting of the particles by the polymer matrix is clearly improved by the coupling treatment, making the interface between two phases

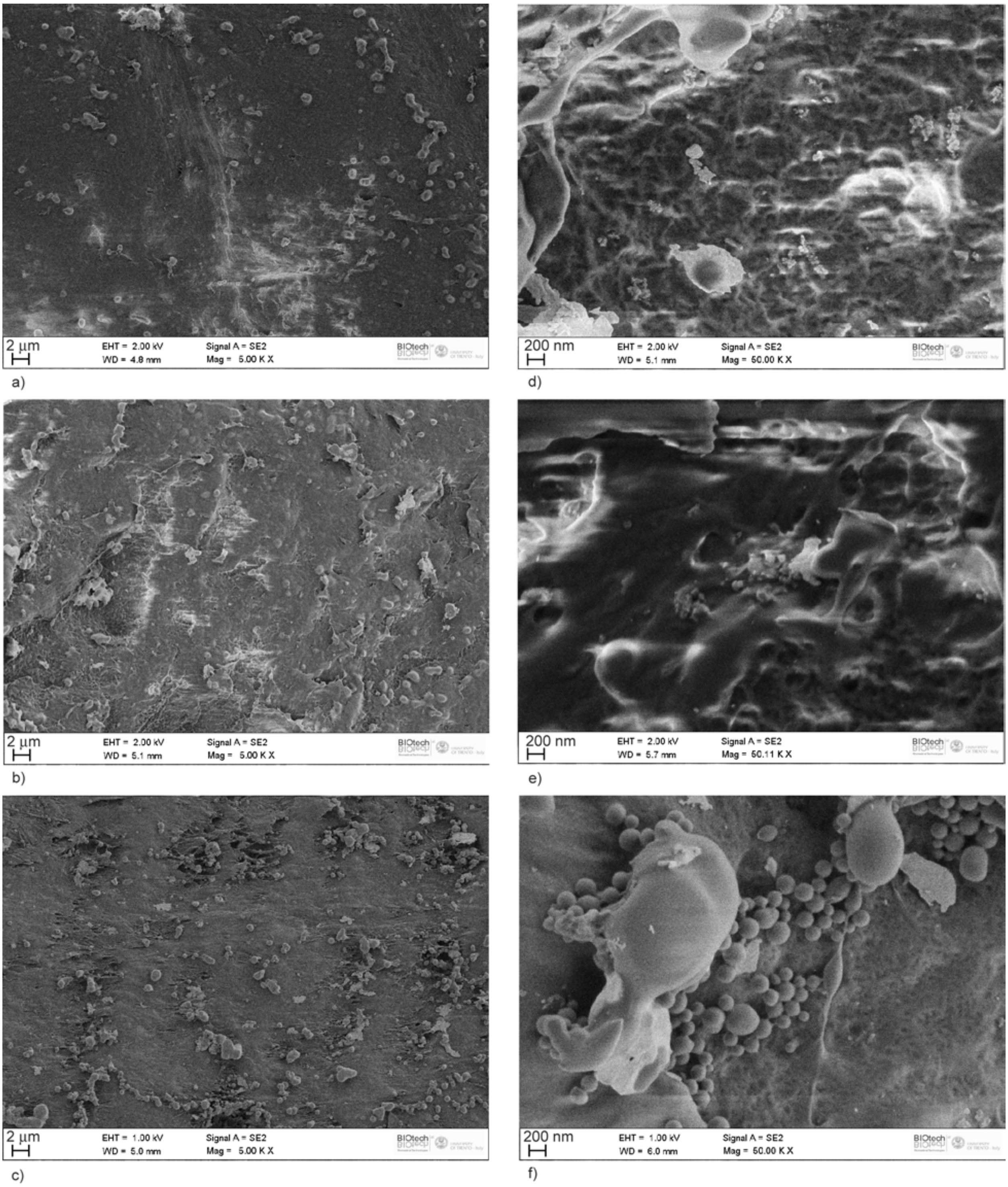

Figure 1. SEM image of the fracture surface of (a, d) LLDPE-D40-4, (b, e) LLDPE-D40 OS-4 and (c, f) LLDPE-D80-4 taken at 5 k× (a, b, c) and 50 k× (d, e, f)

almost undistinguishable. The enhancement of the interfacial adhesion can be explained by a decrease in surface energy of the filler with silane coupling agents, that leads to a better compatibility with the apolar LLDPE matrix. SEM pictures taken at higher magnification confirm the presence of both aggregates and agglomerates within the matrix (Figure 1d–1f). In particular, the aggregates of BA give perfectly spherical submicronic particles in the case of LLDPE-D80-4 composite (Figure 1f). As reported by Droval, this is probably due to a memory form effect coming from the aerosol droplets before drying, resulting in each particle considered as a highly concentrated nanocrystallites boehmite aggregates linked together through a water-rich amorphous phase [36].

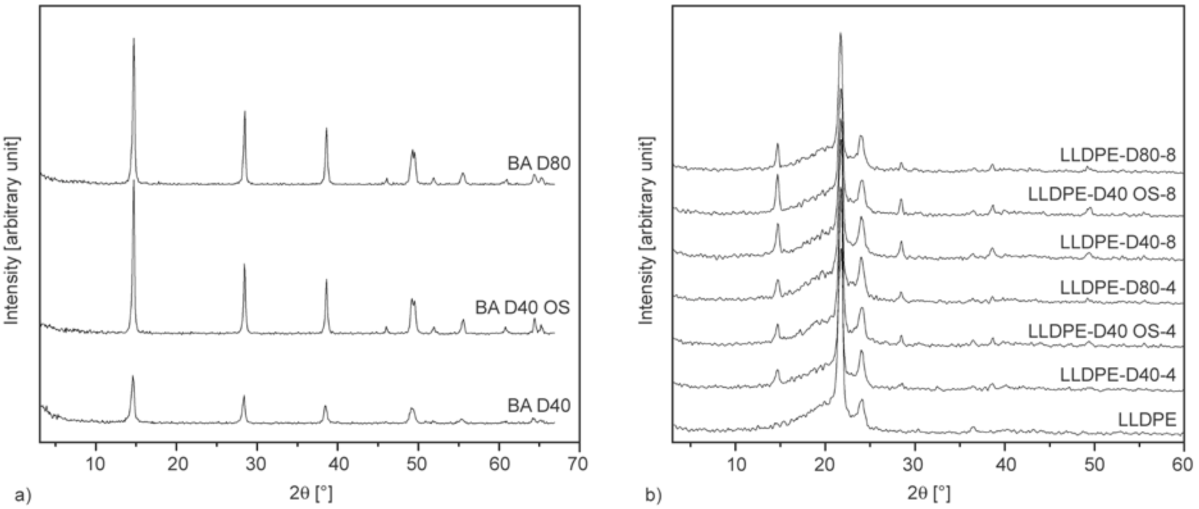

Figure 2. XRD diffractogram of (a) BA nanopowders and (b) LLDPE and LLDPE-BA-4 nanocomposites in comparison

The XRD diffractograms of BA nanopowders and LLDPE nanocomposites are given in Figure 2a and 2b, respectively. In the X-ray diffractograms of BA nanopowders, the peaks (*hkl* plan) at $2\theta = 14.7°$ (020), $2\theta = 28.4°$ (120), $2\theta = 38.7°$(031), $2\theta = 49.2°$ (200), $2\theta = 55.5°$ (151) indicate the presence of the typical orthorhombic crystalline form of BA. The average crystallite size, calculated by the Scherrer's equation [37], is about 38, 40 and 72 nm for BA-D40, BA-D40 OS and BA-D80, respectively, in good accordance to the data reported in the material datasheet [26]. According to XRD diffractograms of LLDPE nanocomposites, the intensity of the signals of all peaks increases with the nanofiller amount. Furthermore, for a given filler content, a stronger signal was found for LLDPE-D40 OS-x nanocomposites with respect to LLDPE-D40-x and LLDPE-D80-x. Most likely, the surface functionalization induced a higher BA crystallinity with respect to untreated BA, or BA for silane modification was taken from another production batch.

The IR spectra of BA nanopowders correspond to those reported for boehmite in the literature [28, 38]. The OH stretching (ν_{OH}) bands are at 3290 and 3091 cm^{-1}, while OH bending (δ_{OH}) appears at 1151 and 1077 cm^{-1}, the γ_{OH} band is at 751 cm^{-1}, symmetrical and asymmetrical Al–O bonds stretching are at 638 and 529 cm^{-1} (Figure 3a).

Representative IR spectra of neat LLDPE, LLDPE-D40-4, LLDPE-D40 OS-4 and LLDPE-D80-4 nanocomposites are compared in Figure 3b. All the spectra of LLDPE-BA nanocomposites are similar with marginal differences in intensity due to the different BA crystallite size. Furthermore, only slight differences are attributable to BA surface functionalization. In particular, formation of small peaks is

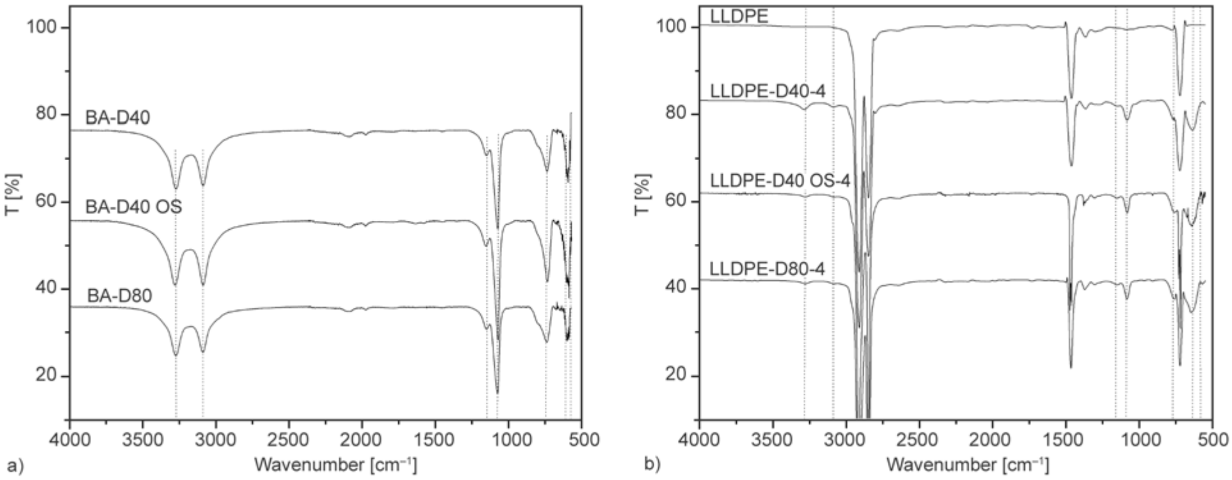

Figure 3. FTIR spectra of (a) BA nanopowders in comparison and (b) LLDPE and LLDPE-BA-4 nanocomposites

observed in the 800–1700 cm^{-1} region, which are commonly referred to the presence of silane coupling agents [39].

3.2. Rheological behavior

The effect of the filler addition on the isothermal frequency dependence of the dynamic shear storage modulus (G') and complex viscosity ($|\eta^*|$) is reported in Figure 4a for unfilled LLDPE and LLDPE composites filled with 4 wt% BA. A general decrease in both G' and $|\eta^*|$can be detected for all LLDPE-BA nanocomposites over the whole frequency range. Furthermore, a similar decrease of both G' and $|\eta^*|$ is also recorded in the case of composites filled with 8 wt% BA (Figure 4b). Noteworthy, the lowering in viscosity is very beneficial for the material processing. For the sake of completeness, some instabilities of the samples are observed at low frequencies, mainly regarding the determination of G' values. This experimental drawback probably occurs due to the adopted cone-plate configuration.

Incorporation of nanofillers in thermoplastics is generally associated to a marked increase in the melt viscosity, at least in the range of low frequencies. Furthermore, a significative enhancement in G' is generally observed. These changes are usually assigned to a pseudo solid-like transition caused by the dispersed nanoparticles [40–46]. Nevertheless, the lowering of both $|\eta^*|$ and G' by BA addition to LLDPE contradicts such general trend. It is interesting to observe that Khumalo *et al*. [26] reported the same rheological behaviour for polyethylene/synthetic boehmite alumina nanocomposites. In particular, a decrease in both G' and $|\eta^*|$ was recorded for LDPE-BA and HDPE-BA nanocomposites with respect to the neat matrices. Also Blaszczak *et al*. [47] studied the rheological beha€iour of LDPE-BA nanocomposite and found that the addition of BA produces a decrease in $|\eta^*|$ compared to that of unfilled LDPE. A possible explanation is based on the fact that, as a result of good adhesion between the polymer matrix and the mineral filler, the polymer melt with filler flows more uniformly, thus at a lower viscosity despite adding solid filler [47]. Moreover, since LLDPE is a highly branched polymer whose chains would tend to get entangled, apparently even poorly bonded plain BA particles fill in the spaces between chain branches and enable an easier flow.

3.3. Thermal properties

As evidenced by DSC analysis, the addition of BA produces a moderate increase of the crystallization temperature for all kinds of boehmite, but no particular dependence of nucleating effect on the BA type is evidenced (Table 2). However, the crystallization peak temperature seems to approach a plateau for boehmite content as high as 4 wt%. The nucleating effect of boehmite was already reported in previous papers for polyethylenes [26] and poplypropylene [27], showing a different nucleating efficiency depending on the crystallite size of boehmite nanofiller.

Concurrently, the melting temperature recorded during the second scan (T_{m2}) is slightly higher for LLDPE nanocomposites, while the crystallinity (χ_{c}) does not seem to have a direct correlation with the nanofiller addition.

The thermal resistance parameters as detected by TGA measurements are also reported in Table 3.

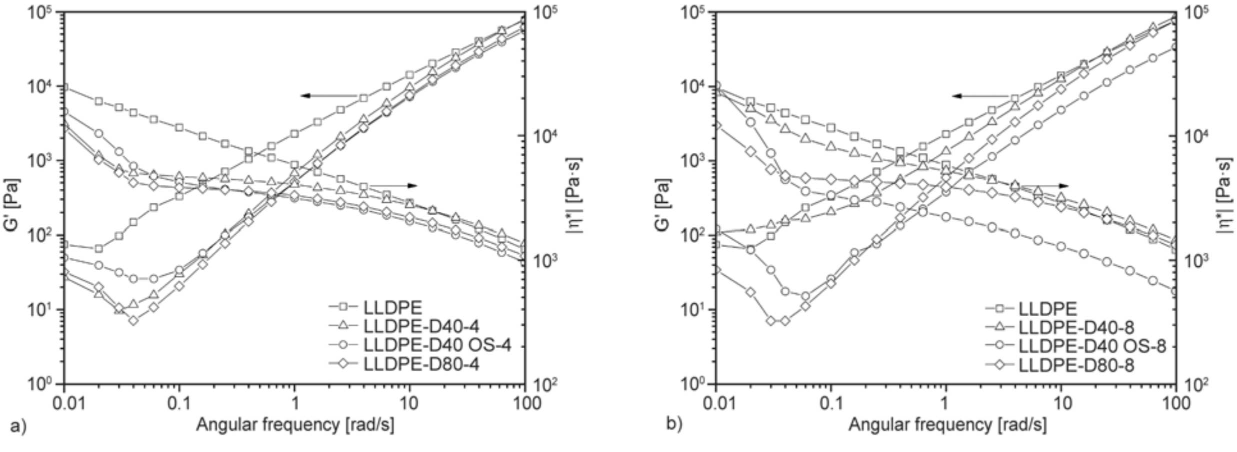

Figure 4. Complex viscosity $|\eta^*|$ and storage modulus (G') with respect to angular frequency (ω) for (a) LLDPE and LLDPE-BA-4 nanocomposites and (b) LLDPE and LLDPE-BA-8 nanocomposites

Table 2. Melting and crystallization characteristics of unfilled LLDPE and relative nanocomposites from DSC measurements

Sample	T_{m1} [°C]	ΔH_{m1} [J/g] (χ_{m1} [%])	T_c [°C]	ΔH_c [J/g] (χ_c [%])	T_{m2} [°C]	ΔH_{m2} [J/g] (χ_{m2} [%])
LLDPE	118.0	102.4 (35.3)	104.2	98.4 (33.9)	117.5	98.4 (33.9)
LLDPE-D40-1	119.5	100.8 (35.1)	111.1	100.3 (34.9)	121.3	100.6 (35.0)
LLDPE-D40-4	121.0	102.8 (36.9)	111.7	98.5 (35.4)	120.8	98.8 (35.5)
LLDPE-D40-8	120.9	98.5 (36.9)	111.2	94.5 (35.4)	120.8	95.2 (35.7)
LLDPE-D40 OS-1	118.9	100.4 (35.0)	104.7	99.3 (34.6)	118.1	99.9 (34.8)
LLDPE-D40 OS-4	121.1	101.2 (36.4)	111.9	99.9 (35.9)	119.1	100.4 (36.1)
LLDPE-D40 OS-8	121.0	98.1 (36.8)	111.2	94.2 (35.3)	119.1	94.7 (35.5)
LLDPE-D80-1	120.6	103.2 (35.9)	110.4	98.6 (34.3)	119.3	98.6 (34.3)
LLDPE-D80-4	121.1	101.2 (36.4)	111.4	99.1 (35.6)	121.2	99.5 (35.7)
LLDPE-D80-8	120.3	98.1 (36.8)	110.5	94.6 (35.5)	121.1	94.9 (35.6)

Table 3. TGA parameters on unfilled LLDPE and relative nanocomposites

Sample	$T_{d,\,onset}$ [°C]	$T_{d,\,max}$ [°C]	Char [%]
LLDPE	457.0	477.1	0.3
LLDPE-D40-1	459.9	477.3	2.7
LLDPE-D40-4	461.7	479.7	3.3
LLDPE-D40-8	463.6	481.4	7.4
LLDPE-D40 OS-1	459.1	478.3	2.2
LLDPE-D40 OS-4	459.7	478.4	3.2
LLDPE-D40 OS-8	461.5	480.1	8.2
LLDPE-D80-1	460.7	480.0	2.1
LLDPE-D80-4	461.0	480.7	3.8
LLDPE-D80-8	462.1	480.3	7.7

When considering LLDPE-boehmite nanocomposites, both $T_{\text{d,onset}}$ and $T_{\text{d,max}}$ markedly increase with the filler content, showing a slightly higher efficiency in LLDPE-D80 samples. Improved thermal and thermo-oxidative stability due to the addition of BA has been already reported for polyethylenes (PEs) [26] and polypropylene (PP) [27, 28]. Nevertheless, future research is required in order to clarify the mechanism of improvement of thermal and thermo-oxidative stability in polyolefines by BA incorporation.

3.4. Tensile mechanical properties and impact strength

As reported in Table 4, the addition of BA nanoparticles produces a significant increase of the elastic modulus of the LLDPE matrix, reaching an improvement of 69% for systems filled with 8 wt% of BA D40, compared to unfilled LLDPE.

The stiffening effect induced by nanofiller incorporation is most often attributed to the formation of a rigid interphase between the matrix and the particles. Nevertheless, it has also been recently pro-

Table 4. Quasi-static tensile properties at yield and at break and tensile energy to break (*TEB*)

Sample	Tensile modulus [MPa]	Tensile strength at yield [MPa]	Tensile strength at break [MPa]	Elongation at break [%]	TEB [J/mm²]
LLDPE	200±6	11.7±0.2	21.6±1.0	1390±91	0.63±0.08
LLDPE-D40-1	218±13	11.8±0.1	19.6±0.4	1259±40	0.63±0.07
LLDPE-D40-4	262±13	12.2±0.4	16.8±0.5	1124±69	0.69±0.11
LLDPE-D40-8	337±12	12.3±0.4	15.1±1.1	964±41	0.70±0.06
LLDPE-D40 OS-1	250±18	11.3±0.2	22.1±0.9	1330±33	0.73±0.05
LLDPE-D40 OS-4	279±22	12.9±0.2	21.1±0.6	1249±32	0.84±0.07
LLDPE-D40 OS-8	306±10	13.4±0.2	19.8±0.3	1040±35	0.87±0.11
LLDPE-D80-1	218±17	12.1±0.3	22.8±0.4	1336±38	0.63±0.05
LLDPE-D80-4	246±10	12.4±0.2	19.4±0.4	1135±54	0.93±0.09
LLDPE-D80-8	302±19	13.3±0.1	19.7±1.3	1043±102	0.90±0.08

posed that nanoparticles aggregation can be another mechanism responsible for stiffness increase in polymer nanocomposites. A new approach developed by Dorigato *et al.* [21, 48] was adopted in order to model the elastic properties of LLDPE-BA nanocomposites taking into account the stiffening effect provided by rigid nanoparticles forming primary aggregates, with the hypothesis that part of the polymer matrix is mechanically constrained within the aggregates. In order to implement the model, the Poisson's ratio of matrix and filler were chosen as 0.44 and 0.23, respectively, while the elastic modulus of BA was considered equal to 385 GPa in according to literature data [49].

The relative elastic modulus of the LLDPE-BA composites is plotted in Figure 5 as a function of the filler volume fraction, along with the fitting curves generated by the adopted model. It can be noticed that the proposed model can predict quite well the elastic modulus of LLDPE-D40-x and LLDPE-D80-x composites over the whole range of filler concentration. Furthermore, the significative increase of the elastic modulus detected for nanocomposites is associated to enhanced *α* values, which indicates the fraction of matrix constrained by nanoparticles. As already noticed by Dorigato *et al.* [20] when applying the model to the case of LLDPE filled with fumed silica nanoparticles, there exists an apparent correlation between the *α* parameter and filler surface area (Table 1). Indeed, the smaller the particle, the higher the surface area and the stronger the propensity to agglomerate, leading to more extensive primary aggregates formed during manufacturing of finer BA filler.

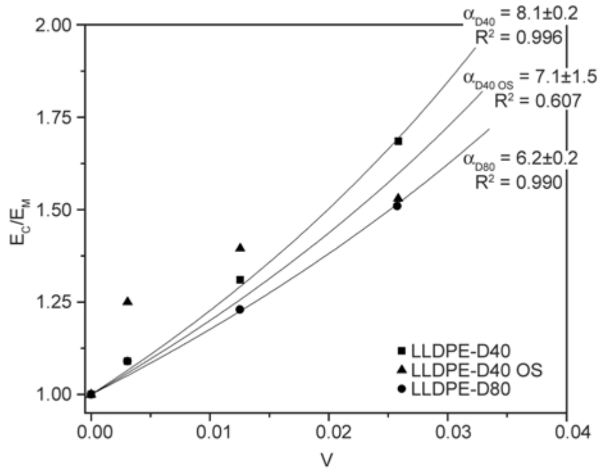

Figure 5. Relative elastic modulus of LLDPE-BA nanocomposites as a function of the filler volume content, with fitting of experimental data in according to the model proposed by Dorigato *et al.* [21] (continuous line). Note that the error bars of data are not represented for clarity reasons.

On the other hand, the proposed model does not satisfactory fit the case of LLDPE-D40 OS-x systems, probably due to a better polymer–filler interaction which produces superior interface properties especially at low nanofiller contents. As already observed from SEM micrographs, the surface functionalization of filler does not significatively affect the filler dispersion but improves the interface properties between matrix and filler.

If the ultimate mechanical properties are considered, it can be observed that the yield stress increases proportionally to the filler content while the stress at break decreases for all kinds of BA nanocomposites, probably because of the filler agglomeration and stronger interaction [16]. For the same reason the elongation at break of nanocomposite is lower than that of neat LLDPE. A similar behavior was reported by Khumalo for the tensile yield and strength of LDPE/BA nanocomposites [51]. Both yield stress and stress at break are slightly higher in LLDPE-D40 OS-x and LLDPE-D80-x samples with respect to LLDPE-D40-x.

When the load is applied at high speed through tensile impact tests, the introduction of BA nanoparticles leads to an interesting increase of the tensile energy at break (TEB). The toughening effect is more intense as the nanoparticles are surface functionalized, in accordance with the conclusions reached under quasi-static tensile loading (Table 4). While the presence of an organic modifier on the surface of the nanoparticles seems to not affect the tensile properties at break under quasi-static conditions, tensile energy at break under impact test is remarkably improved in the case of BA40 OS filled nanocomposites. Rong *et al.* [52, 53] and Wu *et al.* [54] already found that the addition of small amount of modified nanoparticles (SiO_2 or $CaCO_3$) could improve the fracture toughness of polypropylene more effectively than the untreated ones, probably due to a better filler/matrix interaction which produces a delaying the shear yielding of the matrix and favours the filler-matrix load transfer mechanism.

Furthermore, the addition of BA D80 and BA D40 OS produces a stronger enhancement in *TEB* than that of BA D40. This can be attributed to the higher yield stress and stress at break measured for the former samples with respect to the latter ones.

3.5. Viscoelastic behaviour

In Figure 6 the isothermal creep compliance of unfilled LLDPE and its nanocomposites containing 4 wt% BA, under a constant load of 1 MPa and at 30°C, is reported, while in Table 5 the elastic (D_e) viscoelastic and total components of the creep compliance after 2000 s (D_{ve2000} and D_{t2000}, respectively) are summarized. The introduction of BA nanoparticles leads to a significant improvement of the creep stability of the material. It is generally believed that nanoparticles can effectively restrict the motion of polymer chains, influencing the stress transfer at a nanoscale, with positive effects on the creep stability of the material [55]. The addition of BA-D40 OS nanoparticles provides further creep reduction compared to the untreated one. This is probably due to the better restriction of molecular chains during the viscoelastic flow, affected by the BA surface functionalization.

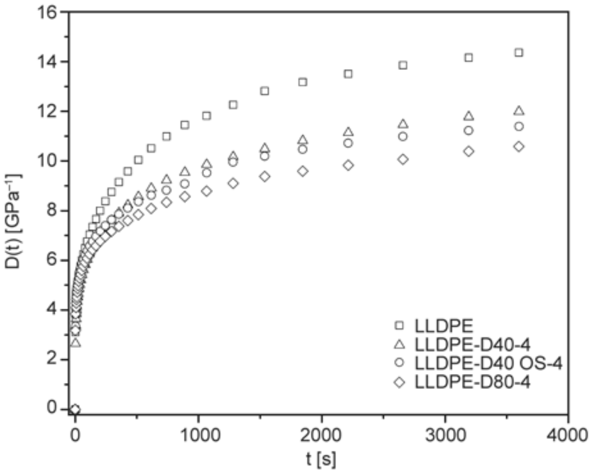

Figure 6. Creep compliance ($D(t)$) of LLDPE and LLDPE-BA-4 nanocomposites ($T = 30°C$, $\sigma_0 = 1$ MPa)

The dynamic-mechanical response of LLDPE is also markedly affected by the addition of BA nanoparticles. The storage modulus (E') increases significantly as the BA content increases, probably due to the restrictions of the molecular chains motion (Table 5), thus indicating that the incorporation of BA nanoparticles remarkably enhances stiffness

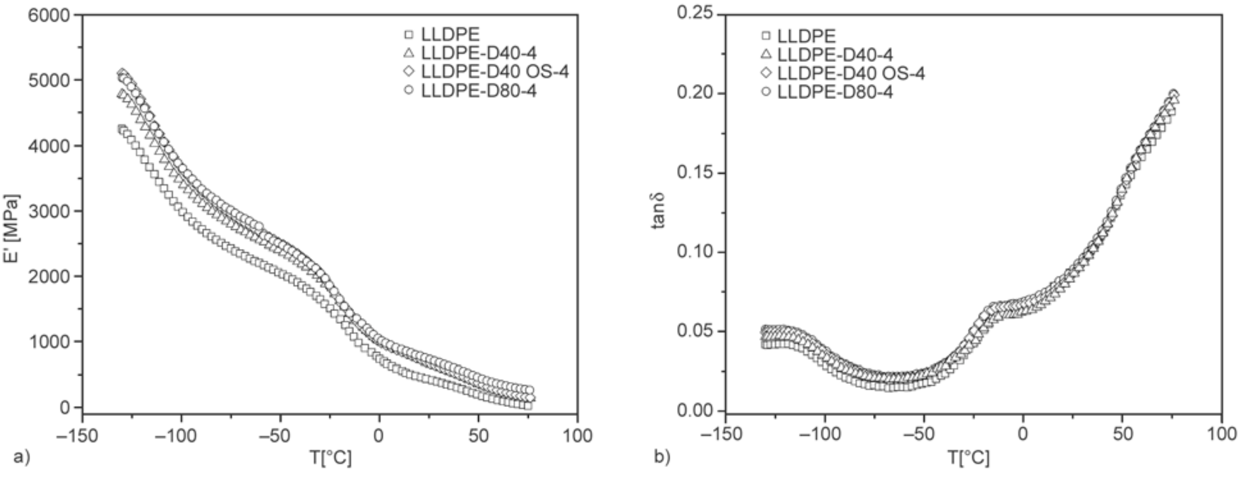

Figure 7. Dynamic mechanical properties of unfilled LLDPE and relative nanocomposites ($f = 1$ Hz): (a) Storage modulus (E') and (b) Loss tangent ($\tan\delta$)

Table 5. Creep compliance data and dynamic mechanical properties of LLDPE and relative nanocomposites ($f = 1$ Hz)

Sample	D_e [GPa^{-1}]	D_{ve2000} [GPa^{-1}]	D_{t2000} [GPa^{-1}]	E′ (–130°C) [MPa]	E′ (23°C) [MPa]	E″ (23°C) [MPa]	T_g [°C]
LLDPE	5.96	7.39	13.35	4236	416	26.0	–110.5
LLDPE-D40-1	5.91	5.74	11.65	4448	590	50.8	–108.2
LLDPE-D40-4	5.72	5.30	11.02	4784	684	56.8	–104.7
LLDPE-D40-8	5.44	4.80	10.24	4942	686	61.7	–103.4
LLDPE-D40 OS-1	5.86	5.65	11.51	4429	540	48.3	–110.3
LLDPE-D40 OS-4	5.70	4.89	10.59	5102	695	58.4	–107.3
LLDPE-D40 OS-8	4.85	2.78	7.63	5258	737	62.2	–105.7
LLDPE-D80-1	5.80	5.45	11.25	4796	617	53.0	–107.8
LLDPE-D80-4	5.43	4.27	9.70	5031	755	59.1	–104.0
LLDPE-D80-8	4.73	4.24	8.97	5627	764	63.8	–103.8

and load bearing capability of the material. The addition of BA-D80 produces the highest enhancement in E'. On the other hand, nanofiller incorporation produces only marginal effect on E'', without dependence on the BA grade. The glass transition temperature (T_g), evaluated in correspondence of the $\tan\delta$ peak, was higher for all nanocomposites with respect to unfilled LLDPE, thus reflecting the restriction of the motion of polymer chains induced by the nanofillers incorporation. Moreover, the T_g increase indicates an effective interfacial interaction between the BA nanoparticles and the LLDPE matrix [13]. Comparison plots of the storage modulus (E') and loss factor ($\tan\delta$) are reported in Figure 7a and 7b, respectively, as a function of temperature for unfilled LLDPE and its nanocomposites containing 4 wt% BA.

3.6. Fracture toughness

The EWF method was applied to characterize the plane stress fracture toughness. At first, the preconditions necessary for the application of the EWF methodology were verified [32]. In particular, the validity criterion verifies that all tests were conducted under plane-stress state. Furthermore, all the specimens exhibited delayed yielding (i.e. the ligament yielding is fully yielded when the crack starts to propagate), with subsequent ductile fracture, showing a large plastic deformation zone surrounding crack tip. Moreover, most specimens manifested evident necking after yielding, in agreement with Equation (3). Since the force – displacement curves of specimens with different ligament lengths were geometrically similar (self-similarity), the fracture mechanism was probably independent on the ligament length (Figure 8).

Interestingly, in all samples including nanocomposites, the area under the curve after the maximum force is higher than that prior to maximum force, thus indicating slow crack propagation with high energy absorption, typical of ductile materials [33]. The addition of BA nanoparticles to LLDPE did not modify these general features.

The elliptical shape of the stress-whitened zone formed during tensile EWF test performed on LLDPE nanocomposites was similar to that of neat LLDPE with slight variation in the height of the zone. The elliptical shape can be characterised by a shape factor β, estimated as $\pi\cdot h/(4L)$, where h is the height of whitened zone while L is the ligament length. The total specific essential work of fracture (w_e), the specific essential work of fracture at yielding ($w_{e,y}$) and the specific essential work of fracture for necking ($w_{e,n}$) were obtained by linear fits and summarized in Table 6. In general, a noticeable improvement of w_e can be observed as the BA content increases for all kinds of BA nanoparticles, whereas $\beta\cdot w_p$ values slightly decrease upon BA addition. These results clearly indicate that BA addition siginficatively toughens the LLDPE matrix [33].

Moreover, partitioned components of the specific essential work of fracture, such as the yielding-related component ($w_{e,y}$) and EWF for necking-related component ($w_{e,n}$), also show an improvement in all nanocomposites when compared to unfilled LLDPE. In particular, the improvement in $w_{e,y}$ is probably due to the higher yield stress of nanocomposites with respect to neat LLDPE, while

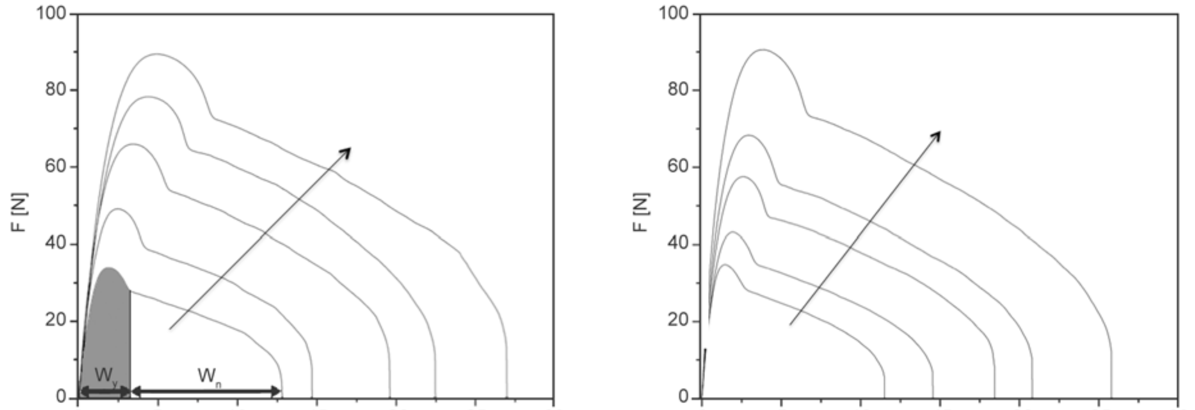

Figure 8. Load–displacement (F–u) curves of (a) LLDPE and (b) LLDPE-D40-8 nanocomposites. The arrow indicates increasing ligament length. The partitioning between yielding and necking works of fracture is indicated in (a).

Table 6. Specific EWF properties of LLDPE and relative nanocomposites

Sample	w_e [kJ/m^2]	β w_p [MJ/m^3]	β	$w_{e,y}$ [kJ/m^2]	β' $w_{p,y}$ [MJ/m^3]	$w_{e,n}$ [kJ/m^2]	β'' $w_{p,n}$ [MJ/m^3]
LLDPE	26.7±3.6	12.7±0.4 (0.983)	0.32±0.04	2.7±0.3	2.78±0.03 (0.997)	24.2±3.6	9.9±0.4 (0.992)
LLDPE-D40-1	26.1±3.3	12.9±0.4 (0.986)	0.27±0.03	3.1±0.5	2.72±0.05 (0.992)	23.1±3.3	10.2±0.2 (0.990)
LLDPE-D40-4	34.1±3.5	11.8±0.4 (0.981)	0.23±0.02	3.5±0.5	2.34±0.06 (0.988)	30.4±3.5	9.5±0.4 (0.993)
LLDPE-D40-8	42.2±3.1	11.0±0.3 (0.983)	0.22±0.02	5.6±0.5	1.92±0.06 (0.985)	36.5±3.1	9.1±0.2 (0.990)
LLDPE-D40 OS-1	29.0±2.0	12.6±0.2 (0.994)	0.28±0.03	2.8±0.5	2.80±0.05 (0.993)	26.1±2.1	9.8±0.4 (0.991)
LLDPE-D40 OS-4	39.1±2.0	11.6±0.2 (0.993)	0.27±0.04	4.3±0.8	2.18±0.09 (0.970)	34.9±2.1	9.4±0.3 (0.995)
LLDPE-D40 OS-8	42.7±2.6	10.5±0.3 (0.986)	0.27±0.03	5.6±0.3	1.96±0.04 (0.993)	37.0±2.6	8.5±0.4 (0.991)
LLDPE-D80-1	28.1±1.3	12.8±0.2 (0.998)	0.27±0.02	2.8±0.3	2.80±0.04 (0.997)	25.2±1.4	10.0±0.3 (0.993)
LLDPE-D80-4	34.0±2.3	11.9±0.3 (0.992)	0.26±0.02	4.4±0.5	2.32±0.06 (0.988)	29.8±2.4	9.6±0.2 (0.993)
LLDPE-D80-8	43.7±1.2	10.8±0.1 (0.997)	0.25±0.02	5.8±0.4	2.15±0.04 (0.992)	37.8±1.3	8.7±0.3 (0.991)

The values in brackets correspond to R^2 values obtained from the linear regression of the data.

the change in $w_{e,n}$ might arise because of an improved crack propagation resistance in nanocomposites [56]. Only marginal differences are appreciable when comparing values of w_e and $\beta \cdot w_p$ in samples filled with different types of BA nanoparticles. On the other hand, the samples LLDPE-D40 OS-x and LLDPE-D80-x show generally higher $w_{e,y}$ values due to the higher yield stress measured with respect to that of LLDPE-D40-x samples.

4. Conclusions

LLDPE based nanocomposites were prepared through melt compounding and hot pressing using different kinds of BA nanoparticles in order to assess the role of the filler crystallite size and surface treatment on the viscoleastic and fracture response of the material.

In particular, both untreated and octylsilane surface treated BA nanoparticles with crystallite size of 40 nm were used to produce the nanocomposites. Furthermore, as means of comparison, other samples were produced with untreated BA particles with primary crystallite size of 74 nm. BA particles were finely and homegenously dispersed in LLDPE though in agglomerated form. The nanoscale dispersion of BA was practically not affected by the surface treatment. BA filling did not affect the crystallinity of the nanocomposites though BA acted as nucleant. Presence of BA slightly enhanced the resistance to thermo-oxidative degradation of the LLDPE matrix. Incorporation of BA was accompanied with an increase in both tensile modulus and yield strength, and with some reduction in both ultimate tensile strength and elongation at break. The tensile impact energy was prominently improved with increasing amount of BA. Larger crystallite particle size and surface treatment of BA yielded further enhancement in this property. Surprisingly, the melt viscosity was reduced by BA nanofillers.

Short term creep tests showed that creep stability was significatively enhanced by nanofiller incorporation. Concurrently, both storage and loss modulus were increased in all nanocomposites. The plane-stress specific essential work of fracture showed a considerable increase (up to 64 %) with the BA content but no significant difference depending on the BA type.

Acknowledgements

This work was performed in the framework of a bilateral cooperation agreement between Italy and Hungary (HU11MO8).

References

[1] Dorigato A., Pegoretti A., Penati A.: Linear low-density polyethylene/silica micro- and nanocomposites: Dynamic rheological measurements and modelling. Express Polymer Letters, **4**, 115–129 (2010).
DOI: 10.3144/expresspolymlett.2010.16

[2] Dorigato A., Pegoretti A., Kolařík J.: Nonlinear tensile creep of linear low density polyethylene/fumed silica nanocomposites: Time-strain superposition and creep prediction. Polymer Composites, **31**, 1947–1955 (2010). DOI: 10.1002/pc.20993

[3] Fu Y. F., Hu K., Li J., Sun Z. H. Y., Zhang F. Q., Chen D. M.: Influence of nano-SiO_2 and carbon fibers on the mechanical properties of POM composites. Mechanics of Composite Materials, **47**, 659–662 (2012). DOI: 10.1007/s11029-011-9245-3

[4] Paul D. R., Robeson L. M.: Polymer nanotechnology: Nanocomposites. Polymer, **49**, 3187–3204 (2008). DOI: 10.1016/j.polymer.2008.04.017

[5] Mirzazadeh H., Katbab A. A., Hrymak A. N.: The role of interfacial compatibilization upon the microstructure and electrical conductivity threshold in polypropylene/expanded graphite nanocomposites. Polymers for Advanced Technologies, **22**, 863–869 (2011). DOI: 10.1002/pat.1589

[6] Kalaitzidou K., Fukushima H., Drzal L. T.: Multifunctional polypropylene composites produced by incorporation of exfoliated graphite nanoplatelets. Carbon, **45**, 1446–1452 (2007). DOI: 10.1016/j.carbon.2007.03.029

[7] Baldi F., Bignotti F., Fina A., Tabuani D., Riccò T.: Mechanical characterization of polyhedral oligomeric silsesquioxane/polypropylene blends. Journal of Applied Polymer Science, **105**, 935–943 (2007). DOI: 10.1002/app.26142

[8] Wu J., Mather P. T.: POSS polymers: Physical properties and biomaterials applications. Polymer Reviews, **49**, 25–63 (2009). DOI: 10.1080/15583720802656237

[9] Mehrabzadeh M., Kamal M. R., Quintanar G.: Maleic anhydride grafting onto HDPE by *in situ* reactive extrusion and its effect on intercalation and mechanical properties of HDPE/clay nanocomposites. Iranian Polymer Journal, **18**, 833–842 (2009).

[10] Giannelis E., Krishnamoorti R., Manias E.: Polymer-silicate nanocomposites: Model systems for confined polymers and polymer brushes. Advances in Polymer Science, **138**, 108–147 (1999). DOI: 10.1007/3-540-69711-x_3

[11] Li B., Zhong W-H.: Review on polymer/graphite nanoplatelet nanocomposites. Journal of Materials Science, **46**, 5595–5614 (2011). DOI: 10.1007/s10853-011-5572-y

[12] Kalaitzidou K., Fukushima H., Drzal L. T.: A new compounding method for exfoliated graphite–polypropylene nanocomposites with enhanced flexural properties and lower percolation threshold. Composites Science and Technology, **67**, 2045–2051 (2007). DOI: 10.1016/j.compscitech.2006.11.014

[13] Rong M. Z., Zhang M. Q., Pan S. L., Lehmann B., Friedrich K.: Analysis of the interfacial interactions in polypropylene/silica nanocomposites. Polymer International, **53**, 176–183 (2004). DOI: 10.1002/pi.1307

[14] Zou H., Wu S., Shen J.: Polymer/silica nanocomposites: Preparation, characterization, properties, and applications. Chemical Reviews, **108**, 3893–3957 (2008). DOI: 10.1021/cr068035q

[15] Zhou R-J., Burkhart T.: Polypropylene/SiO_2 nanocomposites filled with different nanosilicas: Thermal and mechanical properties, morphology and interphase characterization. Journal of Materials Science, **46**, 1228–1238 (2011). DOI: 10.1007/s10853-010-4901-x

[16] Bikiaris D. N., Vassiliou A., Pavlidou E., Karayannidis G. P.: Compatibilisation effect of PP-g-MA copolymer on iPP/SiO_2 nanocomposites prepared by melt mixing. European Polymer Journal, **41**, 1965–1978 (2005). DOI: 10.1016/j.eurpolymj.2005.03.008

[17] Lin O., Mohd Ishak Z., Akil H. M.: Preparation and properties of nanosilica-filled polypropylene composites with PP-methyl POSS as compatibiliser. Materials and Design, **30**, 748–751 (2009). DOI: 10.1016/j.matdes.2008.05.007

[18] Liu S-P., Ying J-R., Zhou X-P., Xie X-L., Mai Y-W.: Dispersion, thermal and mechanical properties of polypropylene/magnesium hydroxide nanocomposites compatibilized by SEBS-*g*-MA. Composites Science and Technology, **69**, 1873–1879 (2009). DOI: 10.1016/j.compscitech.2009.04.004

[19] Mohebby B., Fallah-Moghadam P., Ghotbifar A. R., Kazemi-Najafi S.: Influence of maleic-anhydride-polypropylene (MAPP) on wettability of polypropylene/wood flour/glass fiber hybrid composites. Journal of Agricultural Science and Technology, **13**, 877–884 (2011).

[20] Kontou E., Niaounakis M.: Thermo-mechanical properties of LLDPE/SiO_2 nanocomposites. Polymer, **47**, 1267–1280 (2006). DOI: 10.1016/j.polymer.2005.12.039

[21] Dorigato A., Dzenis Y., Pegoretti A.: Nanofiller aggregation as reinforcing mechanism in nanocomposites. Procedia Engineering, **10**, 894–899 (2011). DOI: 10.1016/j.proeng.2011.04.147

[22] Dorigato A., Pegoretti A.: Fracture behaviour of linear low density polyethylene – fumed silica nanocomposites. Engineering Fracture Mechanics, **79**, 213–224 (2012). DOI: 10.1016/j.engfracmech.2011.10.014

[23] Pedrazzoli D., Pegoretti A.: Silica nanoparticles as coupling agents for polypropylene/glass composites. Composites Science and Technology, **76**, 77–83 (2013). DOI: 10.1016/j.compscitech.2012.12.016

[24] Halbach T. S., Mülhaupt R.: Boehmite-based polyethylene nanocomposites prepared by *in-situ* polymerization. Polymer, **49**, 867–876 (2008).
DOI: 10.1016/j.polymer.2007.12.007

[25] Halbach T. S., Thomann Y., Mülhaupt R.: Boehmite nanorod-reinforced-polyethylenes and ethylene/1-octene thermoplastic elastomer nanocomposites prepared by *in situ* olefin polymerization and melt compounding. Journal of Polymer Science Part A: Polymer Chemistry, **46**, 2755–2765 (2008).
DOI: 10.1002/pola.22608

[26] Khumalo V. M., Karger-Kocsis J., Thomann R.: Polyethylene/synthetic boehmite alumina nanocomposites: Structure, thermal and rheological properties. Express Polymer Letters, **4**, 264–274 (2010).
DOI: 10.3144/expresspolymlett.2010.34

[27] Streller R. C., Thomann R., Torno O., Mülhaupt R.: Isotactic poly(propylene) nanocomposites based upon boehmite nanofillers. Macromolecular Materials and Engineering, **293**, 218–227 (2008).
DOI: 10.1002/mame.200700354

[28] Bocchini S., Morlat-Thérias S., Gardette J-L., Camino G.: Influence of nanodispersed boehmite on polypropylene photooxidation. Polymer Degradation and Stability, **92**, 1847–1856 (2007).
DOI: 10.1016/j.polymdegradstab.2007.07.002

[29] Siengchin S., Karger-Kocsis J.: Structure and creep response of toughened and nanoreinforced polyamides produced via the latex route: Effect of nanofiller type. Composites Science and Technology, **69**, 677–683 (2009).
DOI: 10.1016/j.compscitech.2009.01.003

[30] Siengchin S., Karger-Kocsis J., Apostolov A. A., Thomann R.: Polystyrene–fluorohectorite nanocomposites prepared by melt mixing with and without latex precompounding: Structure and mechanical properties. Journal of Applied Polymer Science, **106**, 248–254 (2007).
DOI: 10.1002/app.26474

[31] Brandrup J., Immergut E. H., Grulke E. A.: Polymer handbook. Wiley, New York (1999).

[32] Williams J. G., Rink M.: The standardisation of the EWF test. Engineering Fracture Mechanics, **74**, 1009–1017 (2007).
DOI: 10.1016/j.engfracmech.2006.12.017

[33] Bárány T., Czigány T., Karger-Kocsis J.: Application of the essential work of fracture (EWF) concept for polymers, related blends and composites: A review. Progress in Polymer Science, **35**, 1257–1287 (2010).
DOI: 10.1016/j.progpolymsci.2010.07.001

[34] Tuba F., Khumalo V. M., Karger-Kocsis J.: Essential work of fracture of poly(ε-caprolactone)/boehmite alumina nanocomposites: Effect of surface coating. Journal of Applied Polymer Science, in press (2013).
DOI: 10.1002/APP.39004

[35] Brostow W., Datashvili T., Huang B., Too J.: Tensile properties of LDPE + boehmite composites. Polymer Composites, **30**, 760–767 (2009).
DOI: 10.1002/pc.20610

[36] Droval G., Aranberri I., Ballestero J., Verelst M., Dexpert-Ghys J.: Synthesis and characterization of thermoplastic composites filled with γ-boehmite for fire resistance. Fire and Materials, **35**, 491–504 (2011).
DOI: 10.1002/fam.1068

[37] Azároff L. V.: Elements of X-ray crystallography. New York, McGraw-Hill (1968).

[38] Kiss A. B., Keresztury G., Farkas L.: Raman and i.r. spectra and structure of boehmite (γ-AlOOH). Evidence for the recently discarded $D^{17}{}_{2h}$ space group. Spectrochimica Acta Part A: Molecular Spectroscopy, **36**, 653–658 (1980).
DOI: 10.1016/0584-8539(80)80024-9

[39] Brostow W., Datashvili T.: Chemical modification and characterization of boehmite nanoparticles. Chemistry and Chemical Technology, **2**, 27–32 (2008).

[40] Abdel-Goad M., Pötschke P.: Rheological characterization of melt processed polycarbonate-multiwalled carbon nanotube composites. Journal of Non-Newtonian Fluid Mechanics, **128**, 2–6 (2005).
DOI: 10.1016/j.jnnfm.2005.01.008

[41] Cassagnau P.: Melt rheology of organoclay and fumed silica nanocomposites. Polymer, **49**, 2183–2196 (2008).
DOI: 10.1016/j.polymer.2007.12.035

[42] Ganß M., Satapathy B. K., Thunga M., Weidisch R., Pötschke P., Jehnichen D.: Structural interpretations of deformation and fracture behavior of polypropylene/multi-walled carbon nanotube composites. Acta Materialia, **56**, 2247–2261 (2008).
DOI: 10.1016/j.actamat.2008.01.010

[43] Renger C., Kuschel P., Kristoffersson A., Clauss B., Oppermann W., Sigmund W.: Rheology studies on highly filled nano-zirconia suspensions. Journal of the European Ceramic Society, **27**, 2361–2367 (2007).
DOI: 10.1016/j.jeurceramsoc.2006.08.022

[44] Sarvestani A. S.: Modeling the solid-like behavior of entangled polymer nanocomposites at low frequency regimes. European Polymer Journal, **44**, 263–269 (2008).
DOI: 10.1016/j.eurpolymj.2007.11.023

[45] Sepehr M., Utracki L. A., Zheng X., Wilkie C. A.: Polystyrenes with macro-intercalated organoclay. Part II. Rheology and mechanical performance. Polymer, **46**, 11569–11581 (2005).
DOI: 10.1016/j.polymer.2005.10.032

[46] Wu D., Wu L., Wu L., Zhang M.: Rheology and thermal stability of polylactide/clay nanocomposites. Polymer Degradation and Stability, **91**, 3149–3155 (2006).
DOI: 10.1016/j.polymdegradstab.2006.07.021

[47] Blaszczak P., Brostow W., Datashvili T., Lobland H. E. H.: Rheology of low-density polyethylene + Boehmite composites. Polymer Composites, **31**, 1909–1913 (2010).
DOI: 10.1002/pc.20987

[48] Dorigato A., Dzenis Y., Pegoretti A.: Filler aggregation as a reinforcement mechanism in polymer nanocomposites. Mechanics of Materials, **61**, 79–90 (2013). DOI: 10.1016/j.mechmat.2013.02.004

[49] Bansal N. P.: Handbook of ceramic composites. New York, Kluwer (2005).

[50] Dzenis Y.: Effect of aggregation of a dispersed rigid filler on the elastic characteristics of a polymer composite. Mechanics of Composite Materials, **22**, 12–19 (1986). DOI: 10.1007/BF00606002

[51] Khumalo V. M., Karger-Kocsis J., Thomann R.: Polyethylene/synthetic boehmite alumina nanocomposites: Structure, mechanical, and perforation impact properties. Journal of Materials Science, **46**, 422–428 (2010). DOI: 10.1007/s10853-010-4882-9

[52] Rong M. Z., Zhang M. Q., Zheng Y. X., Zeng H. M., Walter R., Friedrich K.: Irradiation graft polymerization on nano-inorganic particles: An effective means to design polymer-based nanocomposites. Journal of Materials Science Letters, **19**, 1159–1161 (2000). DOI: 10.1023/A:1006711326705

[53] Rong M. Z., Zhang M. Q., Zheng Y. X., Zeng H. M., Walter R., Friedrich K.: Structure–property relationships of irradiation grafted nano-inorganic particle filled polypropylene composites. Polymer, **42**, 167–183 (2001). DOI: 10.1016/S0032-3861(00)00325-6

[54] Wu C. L., Zhang M. Q., Rong M. Z., Friedrich K.: Tensile performance improvement of low nanoparticles filled-polypropylene composites. Composites Science and Technology, **62**, 1327–1340 (2002). DOI: 10.1016/S0266-3538(02)00079-9

[55] Bondioli F., Dorigato A., Fabbri P., Messori M., Pegoretti A.: Improving the creep stability of high-density polyethylene with acicular titania nanoparticles. Journal of Applied Polymer Science, **112**, 1045–1055 (2009). DOI: 10.1002/app.29472

[56] Yang W., Xie B-H., Shi W., Li Z-M., Liu Z-Y., Chen J., Yang M-B.: Essential work of fracture evaluation of fracture behavior of glass bead filled linear low-density polyethylene. Journal of Applied Polymer Science, **99**, 1781–1787 (2006). DOI: 10.1002/app.22708

eXPRESS Polymer Letters Vol.7, No.8 (2013) 667–672
Available online at www.expresspolymlett.com
DOI: 10.3144/expresspolymlett.2013.63

Low-dielectric, nanoporous polyimide thin films prepared from block copolymer templating

C. Wang, T. M. Wang, Q. H. Wang[*]

State Key Laboratory of Solid Lubrication, Lanzhou Institute of Chemical Physics, Chinese Academy of Sciences, 730000 Lanzhou, P. R. China

Received 23 February 2013; accepted in revised form 19 April 2013

Abstract. In this paper, a new method to the preparation of low-dielectric nanoporous polyimide (PI) films was addressed, based on the self-assembly structures of PS-b-P4VP/poly(amic acid) (PAA, precursor of PI) blends. It is found the microphase-separation structure of PS-b-P4VP/PAA is a precondition of the formation of nanoporous structures, which could be achieved by solvent annealing. Nanoporous PI films with spherical pore size of ~11 nm were obtained by thermal imidization followed by the removal of the PS-b-P4VP block copolymer. The porosity of the nanoporous PI films could be controlled by the weight fraction of the PS-b-P4VP block copolymer. The dielectric properties of the nanoporous PI films were studied, and it was found that the introduction of nanopores could effectively reduce the dielectric constant from 3.60 of dense PI films to 2.41 of nanoporous PI films with a porosity of 26%, making it promising in microelectronic devices. The fabrication method described here could be extended to other polymer systems.

Keywords: *nanomaterials, block copolymer, dielectric constant, nanoporous polyimide, thin films*

1. Introduction

With the development of microelectronic devices becoming smaller and lighter, new low dielectric constant materials are needed to replace the current wire insulator of silicon dioxide, thereby reducing the signal delays and electrical power loss in the new generations of large scale integrated circuits [1–3]. Nanoporous polyimide (PI) material, combining the high performance of PI and the lowest dielectric constant of air void ($k \approx 1$), is thought to be the most promising candidate for use as a next-generation of interlayer dielectrics [4]. Therefore, considerable attention has been focused on the preparation of low-dielectric nanoporous PI films. Besides normal template like poly(ethylene oxide)–polyhedral oligosilsesquioxane (PEO–POSS) nanoparticles [5], silicon nanowires [6], poly[styreneco-(4-vinylpyridine)] (PSVP) nanospheres [7], were used to prepare nanoporous PI films, Hedrick and his coworkers have opened a route to the fabrication of nanoporous PI films. The approach they established involves the preparation of block copolymers consisting of a thermally labile block and highly temperature-stable PI block. The block copolymer could be self-assembled into nanoscale domains with labile block as dispersed phase and PI block as matrix. Pore formation can be accomplished by thermolysis of the labile blocks, which leaves pores of sizes and shapes that correspond to those present in the initial copolymer's morphology [8, 9]. Thanks to their contribution and several other works on the preparation of nanoporous PI films with low dielectric constant based on various PI-based copolymer has been reported [10–13]. However, the synthetic procedures and processing are relatively complicated, furthermore, thermal degradation of the labile com-

---

[*]Corresponding author, e-mail: wangqh@licp.cas.cn

ponent reduces the molecular weight and certain critical mechanical properties of the resulting nanoporous films.

In this study, we described a new method to the preparation of low-dielectric nanoporous PI films using block copolymer as template. Based on the self-assembly structures of block copolymer and poly(amic acid) (PAA, precursor of PI) blends, nanoporous PI films could be obtained after the removal of the block copolymer. Compared to the method Hedrick reported, complex synthetic procedures are avoidable, and the mechanical properties of resultant nanoporous PI films are little influenced because the nanopores come from the simple removal of block copolymer. In this way, the porosity of resultant nanoporous PI films could be controlled by changing of the weight content of block copolymer, thus adjusting the dielectric constant of the films

2. Experimental procedures

2.1. Materials

PS-b-P4VP block copolymer (M_n PS:P4VP = 11800:15000 g/mol and polydispersity of 1.04) was purchased from Polymer Source Inc., Canada, and used as received. 3,3′,4,4′-biphenyltetracarboxylic dianhydride (BPDA), 4,4′-oxydianiline (ODA), and N-Methy1-2-pyrrolidone (NMP), benzene were analytical chemical reagents and purchased from Tianjin Chemical Reagents Company, Tianjin, China.

2.2. Synthesis of poly(amic acid) homopolymer

PAA homopolymer was prepared by solution polymerization in NMP. Into a reaction flask fitted with a mechanical stirrer and Ar inlet were charged 1.8 g of ODA and 30 g of NMP. Stirring was begun, and after the ODA has dissolved, 2.698 g of BPDA powder was added gradually to the stirring solution of the diamine over 40 min. The reaction mixture was reacted at 0°C for 24 h in Ar atmosphere to yield a viscous PAA solution.

2.3. Preparation of nanoporous polyimide thin films

The procedure used to fabricate nanoporous PI films is summarized in Figure 1. The block copolymer PS-b-P4VP and PAA homopolymer was first dissolved in NMP, to make polymer solution with a concentration of 5 wt%. The NMP solution containing 5 wt% polymer mixtures was stirred for more than 24 h at room temperature. PS-b-P4VP/PAA blends in films with a thickness of ~100 nm, were prepared on a silicon wafer by spin-coating at 2000 rpm for 4 min, followed by drying under vacuum at room temperature to remove the residual NMP. The as-spun PS-b-P4VP/PAA films were solvent annealed in a saturated mixture vapor of benzene and NMP at 80°C to achieve self-assembly microstructures. The self-assembled PS-b-P4VP/PAA films were thermally treated to convert PAA to PI at an elevated temperature: 120°C (1 h), 180°C (1 h), 250°C (1 h), and 300°C (1 h). Then, nanoporous PI films with a thickness of ~100 nm, were obtained after the removal of PS-b-P4VP block copolymer by solvent extraction in dichloromethane for 24 h at 50°C.

2.4. Characterization

AFM studies were operated at a Nanoscope IIIa multimode atomic force microscope (Digital Instruments, VEECO, USA) at the tapping mode. Transmission electron microscope (JEM-2010, JEOL Ltd., Japan) operating at an accelerating voltage of 200 kV was used to examine the morphology of PS-b-P4VP/PAA and nanoporous PI films. Films for TEM were prepared on silicon substrates having a thick layer of silicon oxide. These films were floated onto the surface of a 5 wt% hydrofluoric acid solution, transferred to a water bath, and then picked up by a Cu grid. To clearly observe the interior structures of PS-b-P4VP/PAA, iodine was employed as staining agent to selectively contrast PAA chains and P4VP blocks. The samples were placed in vapors of iodine crystals for 2 h at 35°C. The porosity (V) of the nanoporous PI thin films was obtained by calculating from refractive index according to the Maxwell-Garnett modeling as shown by Equation (1) [14]:

$$V = 1 - \left[\frac{(n_\mathrm{p}^2 - 1)(n_\mathrm{s}^2 + 2)}{(n_\mathrm{p}^2 + 2)(n_\mathrm{s}^2 - 1)}\right] \tag{1}$$

where n_p and n_s is refractive index of nanoporous and dense PI thin films, respectively. The dielectric constant of the nanoporous PI films was determined using the Maxwell equation, Equation (2) [15]:

$$\varepsilon \cong 1.1 \cdot n^2 \tag{2}$$

where n is the refractive index. The refractive index was measured with a variable-angle multi-wave-

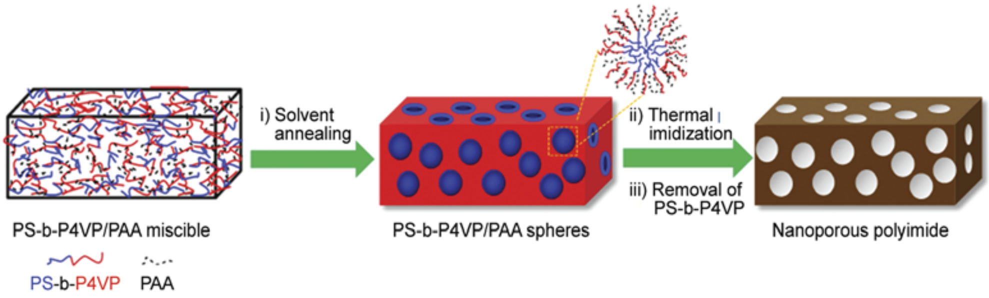

Figure 1. Schematic figure of fabrication of nanoporous PI films

length ellipsometer (L116E, Gaertner Ltd., USA) with wavelengths at 632.8 nm.

3. Results and discussion

Prior to discussion, it should be noted that there exists a strong interpolymer hydrogen-bonding interaction between PAA and P4VP blocks, leading to the formation of P4VP/PAA complex (Figure 2). The selective adsorption of PAA on P4VP blocks could increase the interaction parameter difference between PS and P4VP/PAA phases, resulting in the strong segregated microphase separation [16]. TEM was performed to explore the interior structure of the PS-b-P4VP/PAA thin film. After I_2 staining, the PAA and P4VP microdomains are dark, and the PS components appear light. For the directly spin-coated thin film, it is noticed that Figure 3a represents a homogenous phase. During the formation of PS-b-P4VP/PAA films by spin-coating from NMP solution, not any microphase-separation structures could be obtained due to non-selectivity of NMP and high solvent evaporation rate [17]. We have attempted to prepare porous PI films from the directly spin-coated PS-b-P4VP/PAA film after conversion of PAA into PI and removal of PS-b-P4VP, but it failed. The results demonstrate that the miscible phase of the as-spun PS-b-P4VP/PAA film could not produce any porous structures. The PS-b-P4VP/PAA blends thin film was solvent-annealed in benzene/NMP vapor mixture to achieve microphase-separation [17]. As shown in Figure 3b, it represents a microphase-separation structure consisted of PS spherical domains dispersed within P4VP/PAA matrix.

Figures 4a-c show the AFM images of self-assembled PS-b-P4VP/PAA films with different PAA wt%. It is found spherical microphase-separation structures as well as few of wire-like structures formed. Although PAA weight content in the three PS-b-P4VP/PAA films is different, the diameter of spherical microphase-separation structures, ~19 nm, is nearly the same. The self-assembled PS-b-P4VP/PAA films were thermally treated to convert PAA to PI. FIIR results as shown in Figure 5 confirmed the successful imidization of PAA. Figures 4d–4f describe the AFM images of the resultant PS-b-P4VP/PI films after thermal imidization. Compared to PS-b-P4VP/PAA films, wire-like structures disappear and size of spherical structures increased to ~31 nm. During the conversion of PAA to PI by

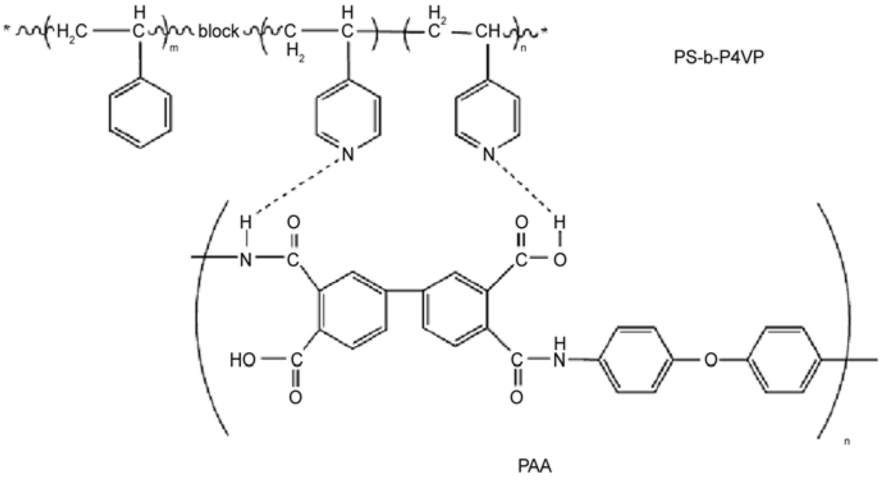

Figure 2. Schematic representation of possible interactions between PAA and PS-b-P4VP block copolymer

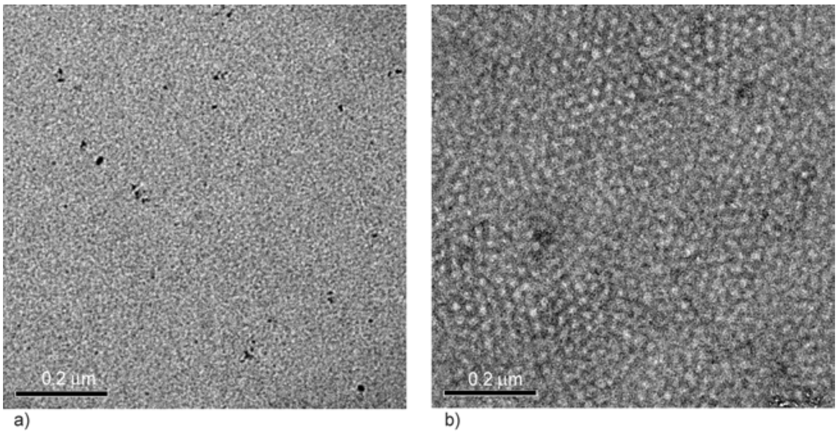

Figure 3. TEM images of PS-b-P4VP/PAA blends thin film with PAA wt% of 50% (a) before and (b) after solvent annealing in benzene/NMP mixture vapor

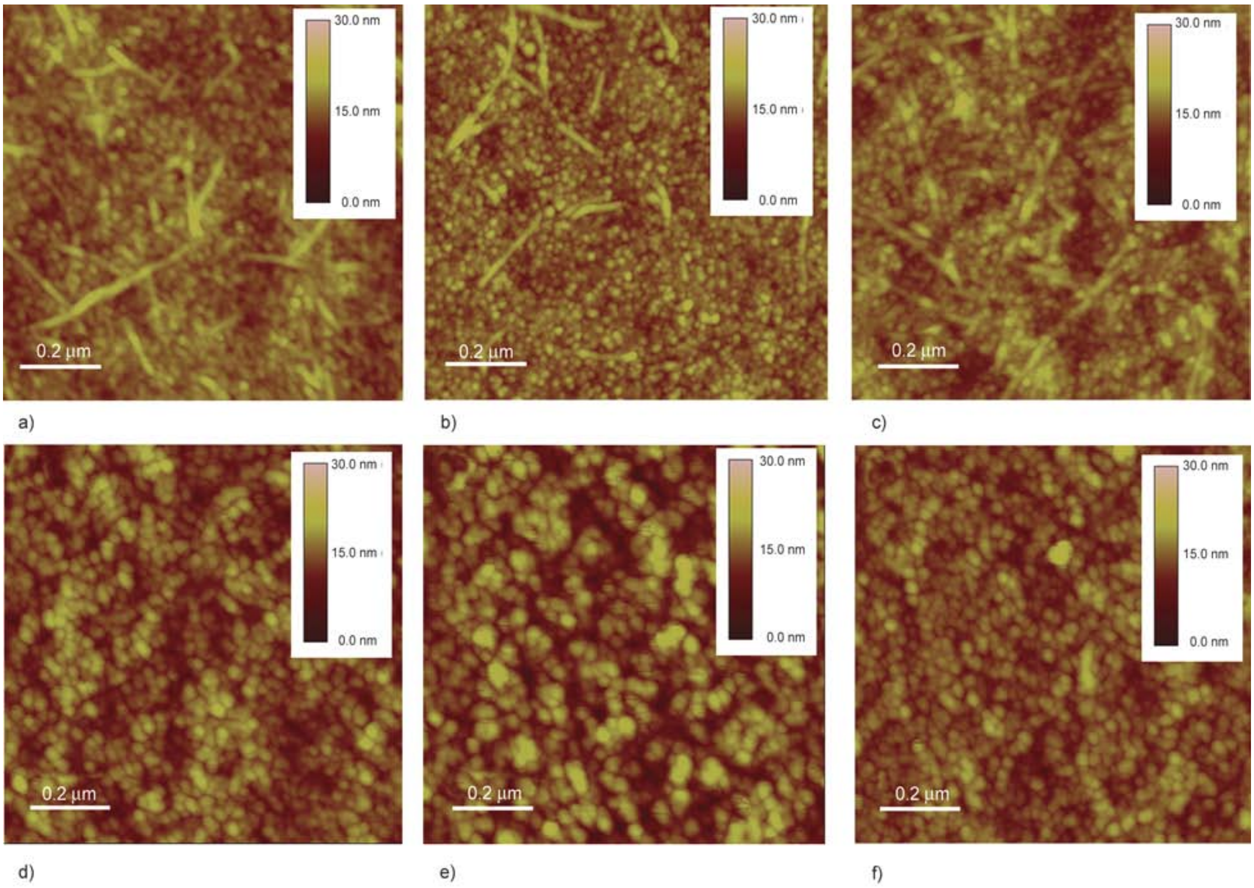

Figure 4. AFM images of PS-b-P4VP/PAA self-assembled films with different PS-b-P4VP wt% of (a) 40%, (b) 50% and (c) 60%. (d), (e) and (f) are AFM images of resultant PS-b-P4VP/PI films after thermal imidization

thermal annealing, PI chains were separated from P4VP blocks because the inter-polymer hydrogen-bonding interaction between PAA and P4VP blocks was destroyed, thus leading to the increase of sphere size and disappearance of wire-like structures.

Nanoporous PI films could be obtained from PS-b-P4VP/PI films after removal of PS-b-P4VP block copolymer by solvent extraction in dichloromethane. Here, solvent extraction of PS-b-P4VP was used to replace traditional thermal decomposition to prevent the collapse of the porous structure during thermolysis at high temperature. As shown in Figure 5, disappearance of the peak at 697 cm^{-1}, corresponding to carbon-nitrogen distortion vibration of the pyridine ring, revealed the complete removal of PS-b-P4VP block copolymer. Figure 6 demonstrates the TEM images of the resultant PI

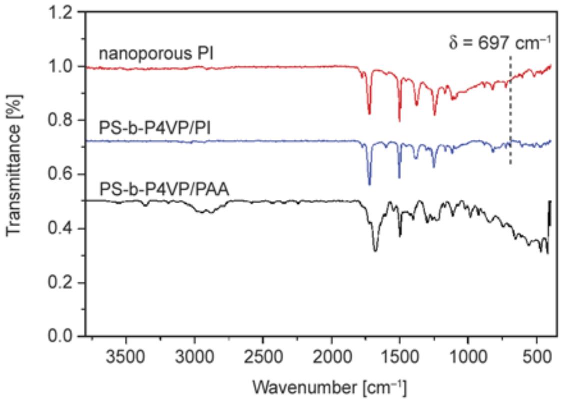

Figure 5. FT-IR spectrums of PS-b-P4VP/PAA, PS-b-P4VP/PI and nanoporous PI thin films

Table 1. Refractive index, porosity and dielectric constant of nanoporous PI films prepared from PS-b-P4VP/PAA blends films with different PS-b-P4VP wt%

Sample	Refractive index	Porosity^{a}	Dielectric constant
PI	1.81	–	3.60
$PI_{40\%}$	1.60	0.20	2.82
$PI_{50\%}$	1.55	0.26	2.64
$PI_{60\%}$	1.48	0.34	2.41

^{a}Determined according to Maxwell-Garnett modeling [14]

films. The nanoscale pores of the films are clearly evident with the white areas. Low contrast in the TEM image could be attributed to the overlapping of projections of nanopores in the thickness direction. Nanoporous structures with nearly the same diameter of ~11 nm were found, formed in three kinds of PI films. It reveals that the weight content of PS-b-P4VP block copolymer did not have any obvious influence on the pore size of resultant nanoporous PI films. It should be noted, in our study here, only three kinds of PS-b-P4VP/PAA films and as-prepared nanoporous PI films were discussed, because the other PS-b-P4VP/PAA films with PS-b-P4VP wt% not in the range of 40~60% could not form proper microphase-separated structures to fabricate nanoporous PI films.

The closed and nanoscale pores of the prepared PI films allow potential applications in microelectronic devices. Table 1 demonstrates the porosity and dielectric constant of the nanoporous PI films. It can be seen the porosity of the films could be adjusted by PS-b-P4VP weight content in PS-b-P4VP/PAA blends films. As the result shows, the dielectric constant of the films decreases with the increasing porosity. The dielectric constant varies from 2.82 to 2.41 for the nanoporous PI films, significantly lower than that of the dense PI film (3.60). It indicates that the incorporation of nanopores successfully reduces the dielectric constant of PI films.

4. Conclusions

Nanoporous PI films with low dielectric constant were prepared, based on the microphase-separated structures of PS-b-P4VP/PAA. The incorporation of nanopores could effectively reduce the dielectric constant of the resultant PI films. Porosity of the nanoporous PI films could be controlled by the weight content of PS-b-P4VP block copolymer, thereby adjusting the dielectric constant of the films. The low dielectric constant of the prepared nanoporous PI films make it promising in the microelectronics.

Since block copolymer have the ability to self-assembly into versatile nanoscale morphologies, it is expected multifarious nanoporous structures could be prepared and the effect of these structures on the dielectric property of the nanoporous PI films could

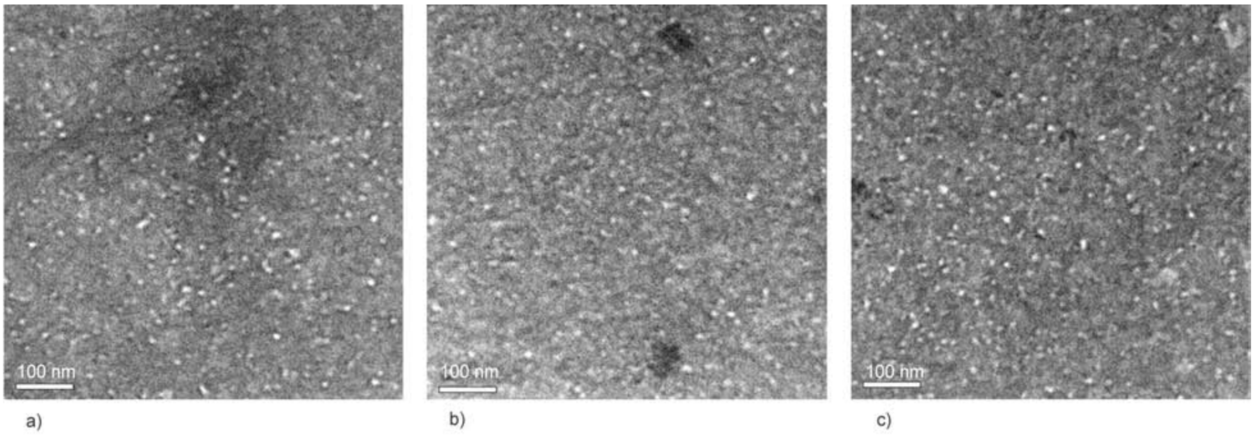

Figure 6. TEM images of nanoporous PI films obtained from PS-b-P4VP/PAA self-assembled films with different PS-b-P4VP wt% of (a) 40%, (b) 50% and (c) 60% after removal of PS-b-P4VP

be studied in the future work. The method described here is simple and controllable, which could be applied to the other polymer systems.

Acknowledgements

The authors would like to acknowledge the financial support of the National Science Foundation for Distinguished Young Scholars of China (Grant No.51025517) and the National Defense Basic Scientific Research Project (A1320110011).

References

[1] Homma T.: Low dielectric constant materials and methods for interlayer dielectric films in ultralarge-scale integrated circuit multilevel interconnections. Materials Science and Engineering R: Reports, **23**, 243–285 (1998).
DOI: 10.1016/S0927-796X(98)00012-6

[2] Geng Z., Lu Y., Zhang S., Jiang X., Huo P., Luan J., Wang G.: Synthesis and characterization of novel adamantane-based copoly(aryl ether ketone)s with low dielectric constants. Polymer International, in press (2013).
DOI: 10.1002/pi.4515

[3] Cho E-B., Mandal M., Jaroniec M.: Periodic mesoporous benzene–silicas prepared using boric acid as catalyst. Chemistry of Materials, **23**, 1971–1976 (2011).
DOI: 10.1021/cm200166f

[4] Zhao G., Ishizaka T., Kasai H., Oikawa H., Nakanishi H.: Fabrication of unique porous polyimide nanoparticles using a reprecipitation method. Chemistry of Materials, **19**, 1901–1905 (2007).
DOI: 10.1021/cm062709w

[5] Lee Y-J., Huang J-M., Kuo S-W., Chang F-C.: Low-dielectric, nanoporous polyimide films prepared from PEO–POSS nanoparticles. Polymer, **46**, 10056–10065 (2005).
DOI: 10.1016/j.polymer.2005.08.047

[6] Kim W., Lee M-K.: Fabrication of a porous polyimide membrane using a silicon nanowire array as a template. Materials Letters, **63**, 933–936 (2009).
DOI: 10.1016/j.matlet.2009.01.060

[7] Xu Z-K., Liu Z-M., Xiao L., Dai Q-W., Kou R-Q.: Polyimide/poly(styrene-co-4-vinylpyridine) nanocomposite films as precursors for the preparation of polyimide nanofoams. Journal of Dispersion Science and Technology, **23**, 519–527 (2002).
DOI: 10.1081/DIS-120014020

[8] Olson D. A., Chen L., Hillmyer M. A.: Templating nanoporous polymers with ordered block copolymers. Chemity of Materials, **20**, 869–890 (2008).
DOI: 10.1021/cm702239k

[9] Wang Y., Li F.: An emerging pore-making strategy: Confined swelling-induced pore generation in block copolymer materials. Advanced Materials, **23**, 2134–2148 (2011).
DOI: 10.1002/adma.201004022

[10] Hedrick J. L., Miller R. D., Hawker C. J., Carter K. R., Volksen W., Yoon D. Y., Trollsås M.: Templating nanoporosity in thin-film dielectric insulators. Advanced Materials, **10**, 1049–1053 (1998).
DOI: 10.1002/(SICI)1521-4095(199809)10:13<1049::AID-ADMA1049>3.0.CO;2-F

[11] Hedrick J. L., Russell T. P., Labadie J. W., Lucas M., Swanson S. A.: High temperature nanofoams derived from rigid and semi-rigid polyimides. Polymer, **36**, 2685–2697 (1995).
DOI: 10.1016/0032-3861(95)93645-3

[12] Hedrick J. L., Russell T. P., Sanchez M., DiPietro R., Swanson S.: Polyimide nanofoams from caprolactone-based copolymers. Macromolecules, **29**, 3642–3646 (1996).
DOI: 10.1021/ma950903q

[13] Hedrick J. L., Carter K. R., Labadie J., Miller R. D., Volksen W., Hawker C. J., Yoon D. Y., Russell T. P., McGrath J. E., Briber R. M.: Nanoporous polyimides. in ‘Advances in polymer science: Progress in polyimide chemistry’ (ed.: H. R. Kricheldorf), Springer-Verlag, Berlin, Vol 141, 1–43 (1999).
DOI: 10.1007/3-540-49814-1_1

[14] Nitta S. V., Pisupatti V., Jain A., Wayner P. C., Gill W. N., Plawsky J. L.: Surface modified spin-on xerogel films as interlayer dielectrics. Journal of Vacuum Science and Technology B, **17**, 205–212 (1999).
DOI: 10.1116/1.590541

[15] Matsumoto T.: Nonaromatic polyimides derived from cycloaliphatic monomers. Macromolecules, **32**, 4933–4939 (1999).
DOI: 10.1021/ma9903862

[16] Wang C., Wang T., Pei X., Wang Q.: Shell–core–corona aggregates formed from poly(styrene)-poly(4-vinylpyridine) block copolymer induced by added homopolymer via interpolymer hydrogen-bonding. Polymer, **50**, 5268–5275 (2009).
DOI: 10.1016/j.polymer.2009.09.028

[17] Wang C., Wang T., Wang Q.: Solvent annealing assisted self-assembly of hydrogen-bonded interpolymer complexes of AB block copolymer/C homopolymer in thin film. Polymer, **51**, 4836–4842 (2010).
DOI: 10.1016/j.polymer.2010.08.047

eXPRESS Polymer Letters Vol.7, No.8 (2013) 673–682
Available online at www.expresspolymlett.com
DOI: 10.3144/expresspolymlett.2013.64

Electrically conductive epoxy nanocomposites containing carbonaceous fillers and *in-situ* generated silver nanoparticles

A. Dorigato[1*], *G. Giusti*[1], *F. Bondioli*[2], *A. Pegoretti*[1]

[1]University of Trento, Department of Industrial Engineering and INSTM Research Unit , Via Mesiano 77, 38123 Trento, Italy
[2]University of Modena and Reggio Emilia, Department of Engineering 'Enzo Ferrari', Via Vignolese 905, 41125 Modena, Italy

Received 25 February 2013; accepted in revised form 21 April 2013

Abstract. An epoxy resin was nanomodified with *in-situ* generated silver nanoparticles (Ag) and with various amounts of carbon black (CB) and carbon nanofibers (NF), in order to increase the electrical conductivity of the matrix. Differential scanning calorimetry tests revealed how the addition of both CB and NF led to a slight decrease of the glass transition temperature of the material, while electron microscopy evidenced how the dimension of CB aggregates increased with the filler content. Both flexural modulus and stress at yield were decreased by CB addition, and the introduction of Ag nanoparticles promoted an interesting improvement of the flexural resistance. CB resulted to be more effective than NF in decreasing the electrical resistance of the materials down to 10^3 Ω·cm. Therefore, a rapid heating of the CB-filled samples upon voltage application was observed, while Ag nanoparticles allowed a stabilization of the temperature for elevated voltage application times.

Keywords: *nanocomposites, epoxy, nanoparticles, nanofibers*

1. Introduction

Due to their low density and good adhesive and mechanical properties, epoxy resins are among the most widespread matrices for structural composites. Because of their chemical versatility and the possibility to tailor the glass transition temperature by using different epoxy bases and/or chain extenders, they were often applied in several technological applications [1]. Furthermore, it has been widely proven that the addition of metal and carbon based nanofillers, such as metal nanopowders, graphite nanoplatelets (GnPs), carbon black (CB) and carbon nanofibers (NFs) could dramatically improve the mechanical behavior and the electrical conductivity of the resulting materials [2–4]. The electrical behavior of these systems can be successfully explained considering the percolation theory [5]. Above a given filler content (i.e. the percolation threshold), the conductive particles form a continuous network through the insulating matrix and the resistivity is harshly decreased by several orders of magnitude. For instance, in a recent work of our group, the thermomechanical properties and the electrical monitoring capability under ramp and creep conditions of an epoxy matrix nanomodified with different amounts of CB and NF was investigated [6]. The best formulation was then used to prepare glass fiber reinforced laminates to be tested under ramp and creep conditions, with a continuous monitoring of their deformational and damage behavior through electrical measurements [7].

---

[*]Corresponding author, e-mail: andrea.dorigato@ing.unitn.it

Recently, different kinds of polymeric materials have been utilized for the preparation of shape memory materials (SMMs). These materials have the peculiar property of 'remembering' their original shape to which they return when subjected to external stimuli [8, 9]. Among them, shape memory alloys (SMAs) and shape memory polymers (SMPs) are the most important ones at present, and their efficacy is strictly connected to their final application [10]. They have been widely applied as smart textiles and apparels [11], intelligent medical devices [12], heat shrinkable packages for electronics [13], high performance water–vapor permeability materials [14], self-deployable structures [15], and microsystems [16]. SMPs can recover their original (or permanent) shapes under appropriate external stimuli, such as heating [1, 8, 16, 17], cooling [18], light [19, 20], electric field [21–26], magnetic field [27–29], water [30], pH, specific ions or enzyme [31]. However, the demand to avoid external heaters has led to a new generation of electrically conducting SMPs filled with conductive nanoparticles, such as carbon nanotubes [21, 22], carbon particles [23, 26], conductive fiber [24] and nickel zinc ferrite ferromagnetic particles.

Taking into account these considerations, the objective of the present work is to characterize the thermal, mechanical and electrical properties of new epoxy based nanocomposites whose amine hardener was nanomodified with *in-situ* reduced silver nanoparticles. Moreover, various amounts of carbon based nanofillers (CB and NF) were dispersed in the polymer matrix in order to evaluate possible synergistic effects. This paper represents the first step of a wider characterization activity focused on the selection of the most promising filler compositions for the preparation of nanofilled polymers with electrically induced shape memory behavior.

2. Experimental

2.1. Materials

A DER 330 epoxy base (density = 1.16 g/mL, epoxy equivalent = 176–185 g/eq), supplied by Dow Chemical Company (Midland, USA), and a Jeffamine D-400 amine hardener (molecular weight = 430 Da, density = 0.972 g/mL, amine equivalent = 115 g/eq), supplied by Huntsman (Everberg, Belgium), were utilized as components of the epoxy system. The same hardener, modified with silver nanoparticles (Ag), was obtained through the *in-situ* reduction of silver nitrate ($AgNO_3$, Sigma Aldrich) [32]. Typically, the reaction solutions were prepared by dissolving 13.3 g of $AgNO_3$ in 100 g of hardener kept at 55°C. After 6 hours, the obtained suspension is characterized by a strong UV visible absorption band at 410 nm characteristic of Ag^0 (here not reported). The shape and the dimensions of the particles were also evaluated by TEM. The obtained images showed that the synthesized powder was nanostructured and presented crystals having rather uniform spherical shape and size in the range from 2 to 5 nm (Figure 1). Thermogravimetric tests evidenced how the nanomodified hardener was characterized by an Ag content of 8.6 wt%.

Ketjenblack EC600JD carbon black (CB) was supplied by Akzo Nobel Chemicals Spa (Arese, Italy). This nanofiller is constituted by fine aggregates of spherical particles with typical dimension of around 40 nm. The specific surface area (SSA) of CB nanoparticles, measured following BET procedure, was 1353 m^2/g, while the density assessed by helium pycnometry was about 1.95 g/cm^3. Vapour grown carbon nanofibers (1195JN) have been supplied by NanoAmor Inc. (Houston, USA). According to the product data sheet, these fibres have a length of 5–40 μm, a core diameter of 0.5–10 nm and an outside diameter of 240–500 nm. The SSA values of NF resulted to be 29 m^2/g, while a density of 1.78 g/cm^3 was evaluated. All materials were used as received.

As far as the preparation of the samples is concerned, different amounts of CB and NF were manually mixed with the epoxy base for 5 minutes. The mixture was then ultrasonicated by using a Hielscher

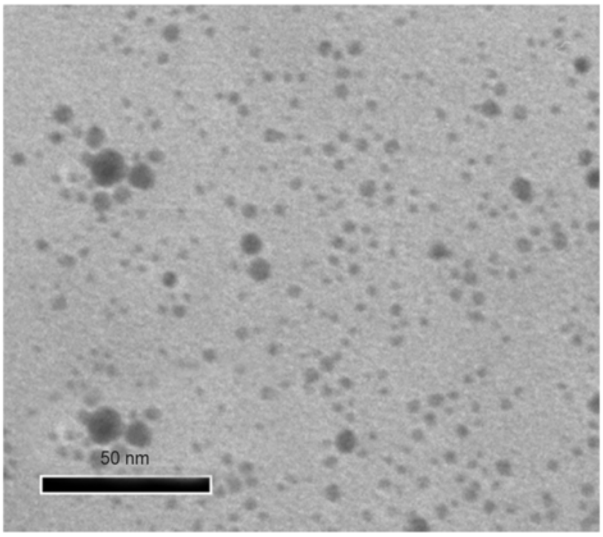

Figure 1. TEM image of the amine hardener with Ag nanoparticles

sonicator for 10 minutes applying a specific power of 100 W/m^2. The stoichiometric amount of hardener was then added to the mixture and manually mixed for 5 minutes. In the case of neat epoxy, a base/hardener ratio of 100/63.9 was utilized, while for the Ag nanomodified epoxy the presence of silver nanoparticles within the hardener led to a stoichiometric ratio of 100/70. After the degassing process, the compounded materials were poured in silicone molds and cured for 2 h at 40°C + 3 h at 110°C + 2 h at 130°C. In this way, neat epoxy and relative nanocomposites with CB or NF amounts between 1 and 4 wt% were prepared. In order to evaluate the effect of the silver nanoparticles within the epoxy matrix, the same samples were prepared by using the Ag nanomodified matrix. In the Results and discussion section, neat epoxy and the Ag nanomodified matrix were designated as EP and EP+Ag, respectively. Nanofilled samples were denoted indicating the nanofiller amount, the nanofiller type and the presence (or not) of Ag nanoparticles within the matrix. For instance, 1CB refers to the nanocomposite sample with a CB amount of 1 wt%, while 1CB+Ag indicates the same nanocomposite prepared by using the Ag nanomodified epoxy.

2.2. Experimental techniques

Morphology of the cryofractured surfaces of the nanofilled samples was investigated by a Zeiss Supra 40 field emission scanning electronic microscope (FESEM), at an acceleration voltage of about 1 kV and a pressure of 10^{-6} Torr. The surfaces of the samples were metalized with a silver paste before the observations. The glass transition temperature (T_g) was evaluated by differential scanning calorimetry (DSC) tests, performed with a Mettler DSC30 apparatus (Schwerzenbach, Switzerland). A thermal cycle from –20 to 160°C, at a heating rate of $10°C\cdot min^{-1}$ under a nitrogen flow of $100\ mL\cdot min^{-1}$, was adopted. Flexural tests for the determination of elastic modulus (E) and flexural stress at yield ($\sigma_{y,f}$) were performed at 23°C and at relative humidity of 50% according to ASTM 790-10 standard by using an Instron® 4502 testing machine (Norwood, Massachusetts, USA). Rectangular samples, 2 mm thick and 5 mm wide, were tested setting a distance between the supports of 40 mm and a testing speed of 1.33 mm/min (maximum strain rate of $0.01\ min^{-1}$). At least five specimens were tested for each sample. Electrical bulk resistance measurements were performed at 23°C and at relative humidity of 50% in direct current mode. A model 6517A 6 1/2-digit electrometer/high resistance system, by Keithley Instruments Inc. (Cleveland, Ohio, USA) was used for electrical measurement in a 2-point test configuration. In order to decrease the contact resistance, the sample surfaces in contact with the electrodes were painted with a silver coating. Measurements were carried out on rectangular samples (cross section of 5 mm × 2 mm, length of 30 mm), and at least five specimens were tested for each composition. When the electrical resistance was lower than $10^5\ \Omega$, measurements were carried out under an applied voltage of 10 V, and the resistance values were measured after a time lapse of 60 s, in order to minimize time-dependent effects. When the electrical resistance was between 10^5 and $10^{12}\ \Omega$, measurements were carried out under an applied voltage of 100 V. When the electrical resistance was higher than $10^{12}\ \Omega$, measurements with an applied voltage of 1000 V were taken on square film samples (length of 95 mm and thickness of 2 mm). In this latter case coaxial electrodes were used in order to minimize the amount of current flowing through the surface. In order to evaluate the Joule effect produced by the current flowing through the samples upon voltage application, surface temperature measurements were performed. The same equipment and configuration used for electrical resistivity measurements was adopted, and various voltages ranging from 100 to 220 V were applied. The increase of the temperature produced by the electrical heating of the samples was monitored through an Optris® LaserSight infrared digital thermometer, acquiring an experimental point every 30 s.

3. Results and discussion

3.1. Microstructure

It is well known that the thermal and the mechanical behavior of nanocomposite samples is directly influenced by the dispersion state of the nanofiller within the matrix. In Figure 2a–2h) FESEM images of the fracture surfaces of the prepared nanocomposites are reported. As it is often claimed in the scientific literature [6, 7], the microstructure of CB nanocomposite system is characterized by the presence of primary particles arranged in aggregates and agglomerates, homogeneously distributed within the polymer matrix. 1CB system is characterized by the presence of tiny and pale primary particles with

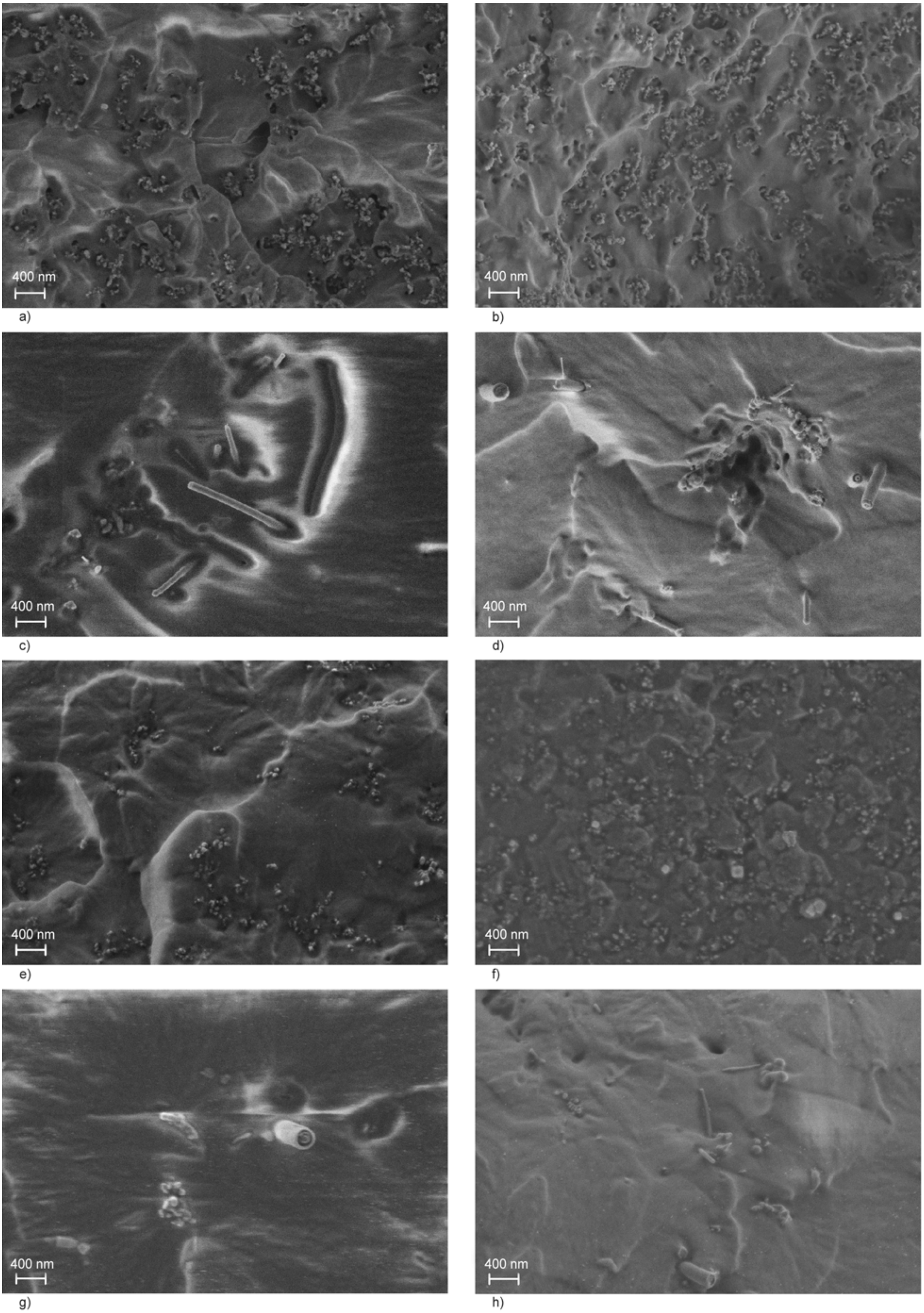

Figure 2. FESEM images of the fracture surfaces of epoxy based nanocomposites: (a) 1CB, (b) 4CB, (c) 1NF, (d) 4NF, (e) 1CB+Ag, (f) 4CB+Ag, (g) 1NF+Ag, (h) 4NF+Ag

average diameter of about 40 nm, organized in agglomerates of about 250 nm (Figure 2a). 4CB sample manifests a higher particle density and a more pronounced tendency of the particles to form agglomerates (Figure 2b). In fact, the agglomerates are larger (about 450 nm) than that detectable at a lower nanofiller content. As often reported for particulate filled nanocomposites, as the filler amount increases the mean interparticle distance diminishes and the probability of aggregation is therefore enhanced [33]. NF filled nanocomposites exhibit a more complex microstructure. Some cavities, most probably related to fiber-matrix debonding phenomena, are detectable on the fracture surface (Figure 2c–2d). 1CB+Ag and 4CB+Ag composites are characterized by a morphology in which silver primary nanoparticles are homogeneously distributed within the matrix forming aggregates of 4–5 nanoparticles having a mean diameter of about 300 nm (Figure 2e–2f). Interestingly, the microstructure of 1NF+Ag and 4NF+Ag samples is characterized by the presence of Ag aggregates localized near the NF or adhering on the nanofiber surface (Figure 2g–2h). This microstructural feature may play an important role in the electrical conductivity.

3.2. Thermal properties

Representative DSC thermograms of EP and EP+Ag samples are reported in Figure 3, while T_g values collected during the first heating scan of DSC tests are summarized in Table 1. Comparing T_g data reported in Table 1, it can be concluded that transition temperature seems to be slightly reduced upon nanofiller addition, especially for elevated CB amounts. A similar trend has been previously observed and reported by our group for various nanofilled thermosets [6, 33–37], and it can be explained considering that the crosslinking process can be partially hindered for elevated filler loadings. The observed T_g trend could be due to the occurrence of two concurrent phenomena: as the filler content increases the chain blocking effect is more effective and induces a slight T_g increase, while, at the same time, polymer-filler chemical interactions and the viscosity increase reduces the crosslinking degree of the matrix, with a consequent T_g drop. In a recent investigation on epoxy/alumina nanocomposites, Liu *et al.* [38] speculated that the hardener molecules were unevenly distributed at a microscale, thus leading to a stoichiometric imbalance between epoxy components and reduced T_g values.

Table 1. Glass transition temperature from DSC tests on neat epoxy and nanocomposites (first heating scan)

Sample	T_g [°C]	Sample	T_g [°C]
EP	49.3	EP+Ag	47.6
1CB	43.6	1CB+Ag	45.5
2CB	46.9	2CB+Ag	47.5
4CB	43.0	4CB+Ag	42.7
1NF	47.3	1NF+Ag	44.1
2NF	46.9	2NF+Ag	44.1
4NF	45.3	4NF+Ag	45.4

3.3. Mechanical behavior

Representative load-displacement curves of flexural tests on epoxy based nanocomposites filled with carbon black are reported in Figure 4, while the elastic and yield properties of epoxy/CB and epoxy/NF nanocomposites are respectively reported in Figure 5 and 6. As it often happens with epoxy

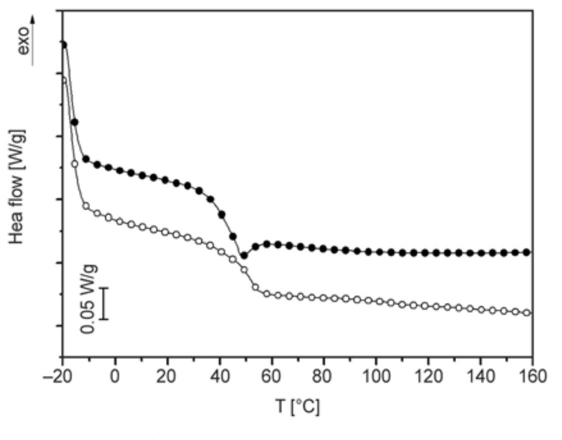

Figure 3. DSC thermograms of EP (○) and EP+Ag (●) samples (first heating stage)

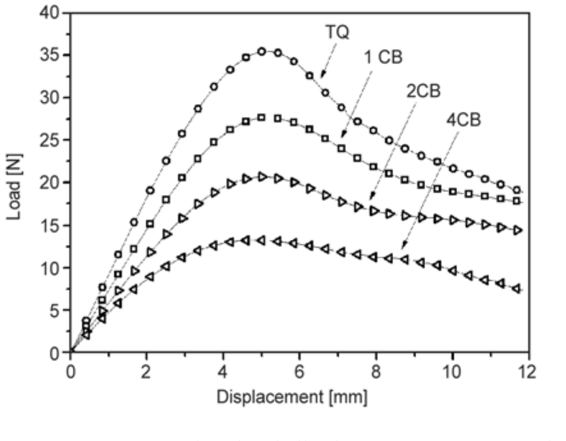

Figure 4. Representative load-displacement curves under flexural conditions for epoxy based nanocomposites filled with carbon black nanoparticles

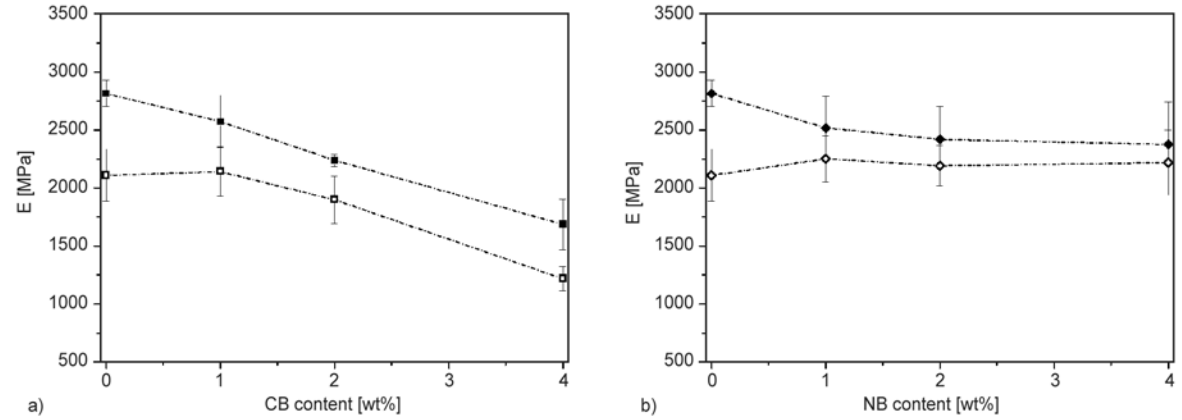

Figure 5. Elastic modulus (*E*) from flexural tests on: (a) epoxy/CB and on (b) epoxy/NF nanocomposites (nanofiller content = 1–4 wt%). Samples with (full symbols) and without (open symbols) Ag nanoparticles.

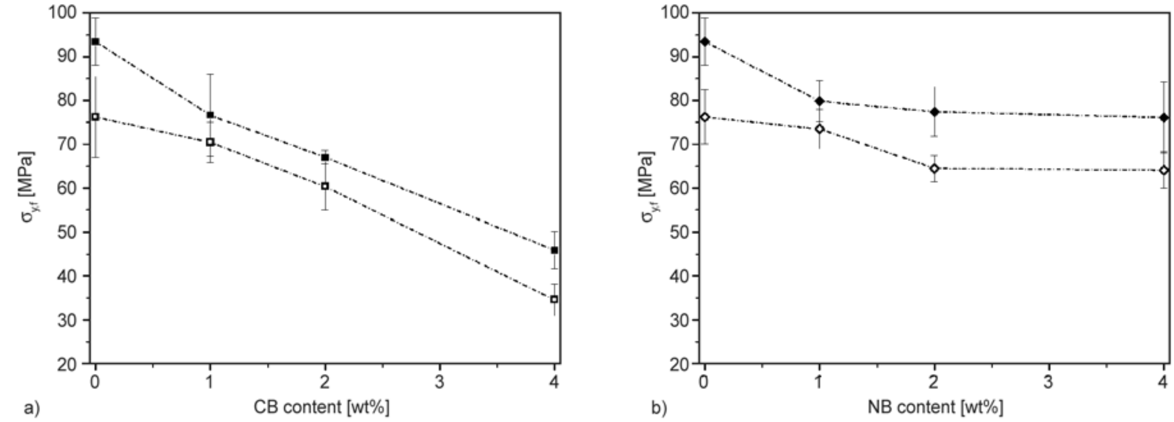

Figure 6. Stress at yield ($\sigma_{y,f}$) from flexural tests on: (a) epoxy/CB and on (b) epoxy/NF nanocomposites (nanofiller content = 1– 4 wt%). Samples with (full symbols) and without (open symbols) Ag nanoparticles.

systems with relatively low T_g (around 50°C), the specimens do not break in a brittle manner under flexure, but the load reaches a maximum (i.e. flexural stress at yield), after which a plastic and irreversible deformation process without a clear failure occurs (Figure 4). It can be noticed that the addition of CB markedly plasticizes the epoxy matrix similarly to what previously observed for epoxy/silica nanocomposites [39]. Interestingly, the elastic modulus is reduced by CB introduction (Figure 5a), especially at elevated filler amounts. On the contrary, the elastic modulus seems to be substantially unaffected by NF introduction (Figure 5b). Both this facts and the lower T_g drop detected from DSC tests for NF-based nanocomposites could be explained by considering the lower specific surface area of NF (29 m^2/g) with respect to CB (1353 m^2/g) and, consequently, the different filler/matrix interactions. On the other hand, the introduction of silver nanoparticles systematically increases the stiffness of the composites for all the tested compositions. A similar trend can be observed if the stress at yield values are considered (Figure 6). Flexural yield stress steadily decreases when CB is added, while $\sigma_{y,f}$ is practically constant for NF filled nanocomposites. Even in this case, the introduction of Ag nanoparticles within the hardener enhances the yield resistance of the samples.

3.4. Electrical conductivity and heating by Joule effect

In Figure 7a the trend of electrical resistivity of epoxy based nanocomposites without silver nanoparticles are represented, while in Figure 7b the electrical resistivity of the corresponding samples with the addition of Ag nanoparticles are summarized. The electrical resistivity of the neat matrix is of about 10^{16} Ω·cm, in the typical range generally reported for epoxy resins [6]. CB filled nanocomposites show a percolation threshold for a filler concentration lower than 1 wt% (Figure 7a), with a further resistivity drop for higher filler loading, reaching a plateau

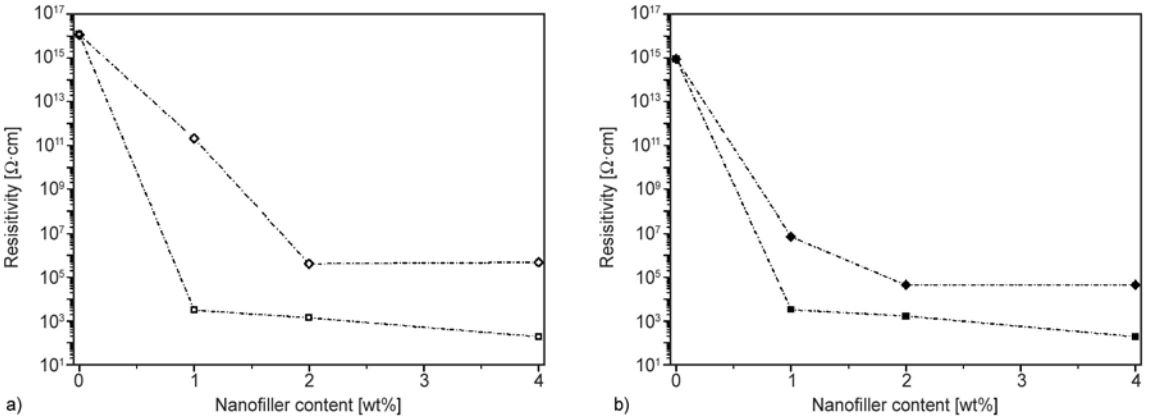

Figure 7. Electrical resistivity of epoxy based nanocomposites (filler content = 1–4 wt%). Samples without (a) and with (b) Ag nanoparticles filled with CB (□, ■) or NF (◊, ♦).

value at around 10^3 Ω·cm for nanofiller contents of 4 wt%. The electrical resistivity of CB filled nanocomposites is not substantially influenced by the introduction of Ag nanoparticles. On the other hand, NF based nanocomposites without Ag nanoparticles show a percolation threshold at 2 wt%, reaching a plateau value of 10^6 Ω·cm for a filler loading of 4 wt%. It is interesting to observe how the introduction of Ag nanoparticles in NF based nanocomposites leads to a remarkable reduction of electrical resistivity for all the tested compositions, reaching a value of 10^4 Ω·cm after the percolation threshold (Figure 7b). The positive contribution played by Ag nanoparticles on the conductivity of these composites can be probably correlated with their peculiar morphological features. As reported in FESEM micrographs (Figure 2g–2h), Ag aggregates are localized near NFs or directly adhere on NFs sur-

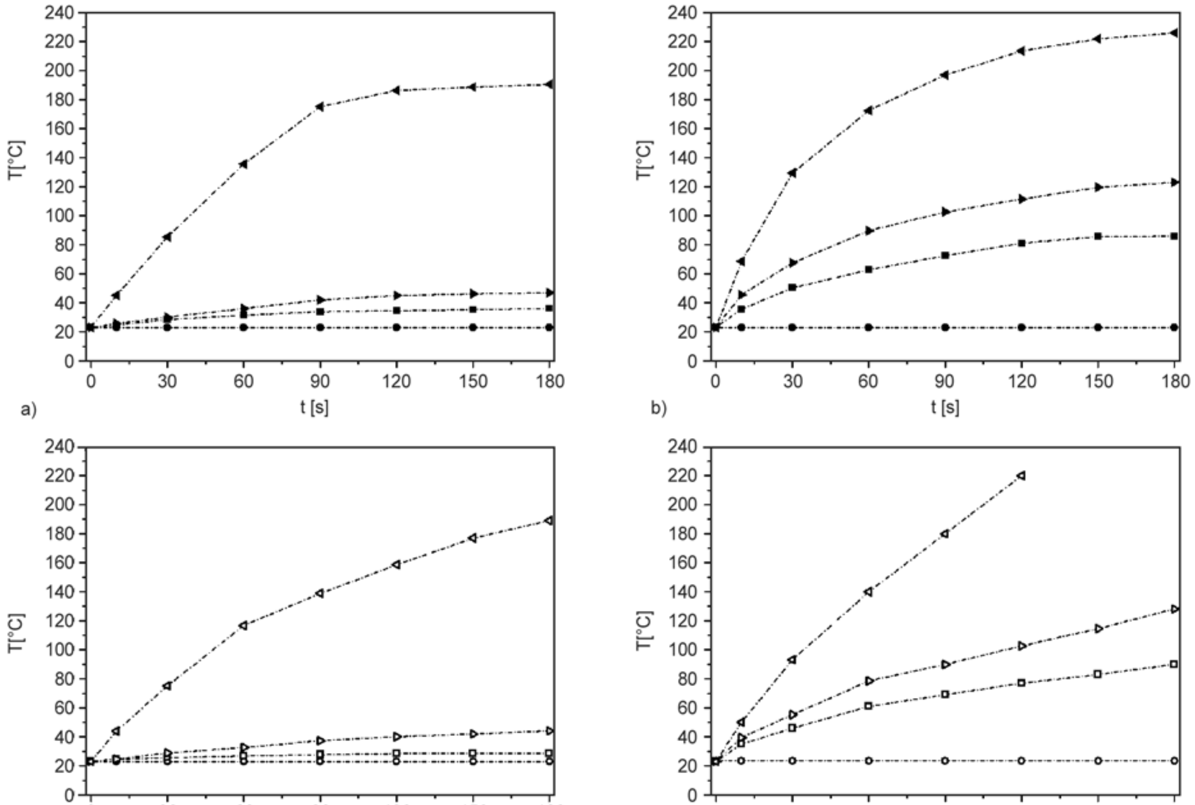

Figure 8. Time dependency of the surface temperature of epoxy/CB nanocomposites at an applied voltage of (a–c) 100 V and (b–d) 220 V. CB content of 0 wt% (●, ○), 1 wt% (■, □), 2 wt% (▶, ▷) and 4 wt% (◀, ◁). Samples with (full symbols) and without (open symbols) Ag nanoparticles.

face. In these conditions the formation of a conductive path is favored, with a consequent reduction of the electrical resistivity.

Considering that the eventual application of the tested materials as electro active SMPs is strictly connected to their capability of reaching the transition temperature (i.e. the glass transition temperature for epoxy systems) upon voltage application, surface temperature measurements at different voltages were performed. In Figure 8a–8d the time dependency of the surface temperature of epoxy/CB nanocomposites is summarized. Except for the samples without CB and NF, it can be noticed that the surface temperature increases with the voltage application time. Moreover, for all the tested specimens the surface temperature increases proportionally to the nanofiller amount in the whole interval of voltage application time. At 100 V, the transition temperature (about 45°C) can be reached only with a CB content of 4 wt% (Figure 8a–8c). Increasing the voltage up to 220 V, all samples reach a temperature higher than 45°C (T_g) in less than 30 s (Figure 8b–8d). Interestingly, the presence of Ag nanoparticles within the matrix is able to stabilize the temperature reached by the samples for long voltage application times (Figure 8a–8b). This feature is probably related to the high heat dissipation capability of Ag nanoparticles within the matrix. Considering that the electrical conductivity of CB nanocomposites is not substantially affected by the presence of silver within the matrix, this peculiar feature can be related to the higher heat dissipation capability of the composites in the presence of metallic nanoparticles. This aspect is very important to prevent the overheating and the consequent thermal degradation of the material at elevated voltages. The same tests were performed on NF filled nanocomposites and the most important results are summarized in Figure 9a–9d. Regardless the presence of Ag nanoparticles, an applied voltage of 100 V is not enough to raise the surface temperature up to the T_g of the material (Figure 9a–9c). The increase of the voltage up to 220 V promotes a slight heating of the samples increasing with the NF amount. However, the temperature of 26°C reached on the surface of 4 wt% filled nanocomposites after 180 s is by far below the glass tran-

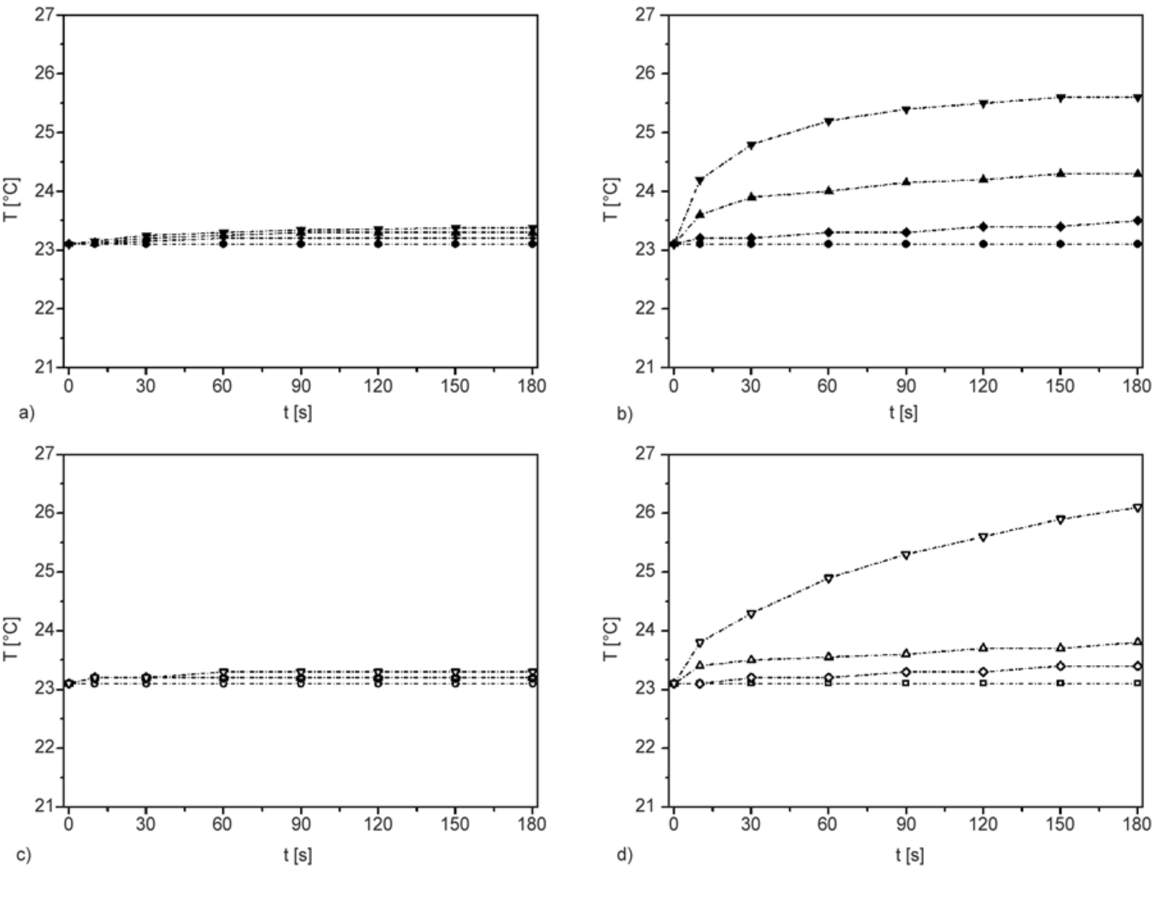

Figure 9. Time dependency of the surface temperature of epoxy/NF nanocomposites at an applied voltage of (a–c) 100 V and (b–d) 220 V. NF content of 0 wt% (●, ○), 1 wt% (♦, ◊), 2 wt% (▲, △) and 4 wt% (▼, ▽). Samples with (full symbols) and without (open symbols) Ag nanoparticles.

sition temperature of the material (Figure 9b–9d). On the other hand, electrical resistivity measurements (Figure 7a–7b) demonstrated how the conductivity of CB nanocomposites is systematically higher than that of the corresponding NF filled samples. This means that an electrical resistivity of about 10^3 Ω·cm is required to thermally activate epoxy based nanocomposites by Joule effect, and that the presence of high heat dissipating filler (i.e. Ag nanoparticles) promotes temperature stabilization for long voltage application times.

4. Conclusions

Conductive polymer nanocomposites were prepared adding different amounts of carbon black and carbon nanofibers to an epoxy resin nanomodified with *in-situ* generated silver nanoparticles. The glass transition temperature of the material was slightly decreased by the addition of both CB and NF, while the dimension of CB aggregates within the matrix increased with the filler content. The introduction of CB promoted a decrease of the stiffness and of the yield properties of the matrix, while Ag nanoparticles were responsible of an interesting improvement of the flexural yield stress. The electrical resistivity of the materials was strongly reduced upon CB introduction, with a percolation threshold of about 1 wt%. Surface temperature of CB nanocomposites was rapidly increased above the glass transition temperature when a proper voltage was applied. Ag nanoparticles resulted to be effective in stabilizing the temperature for elevated voltage application times, thus avoiding the thermal degradation of the material.

References

[1] Liu C., Qin H., Mather P. T.: Review of progress in shape-memory polymers. Journal of Materials Chemistry, **17**, 1543–1558 (2007).
DOI: 10.1039/B615954K

[2] Fan Z., Zheng C., Wei T., Zhang Y., Luo G.: Effect of carbon black on electrical property of graphite nanoplatelets/epoxy resin composites. Polymer Engineering and Science, **49**, 2041–2045 (2009).
DOI: 10.1002/pen.21445

[3] Li J., Wong P-S., Kim J-K.: Hybrid nanocomposites containing carbon nanotubes and graphite nanoplatelets. Materials Science and Engineering A, **483–484**, 660–663 (2008).
DOI: 10.1016/j.msea.2006.08.145

[4] Sumfleth J., Buschhorn S. T., Schulte K.: Comparison of rheological and electrical percolation phenomena in carbon black and carbon nanotube filled epoxy polymers. Journal of Materials Science, **46**, 659–669 (2011).
DOI: 10.1007/s10853-010-4788-6

[5] Traina M., Pegoretti A., Penati A.: Time–temperature dependence of the electrical resistivity of high-density polyethylene/carbon black composites. Journal of Applied Polymer Science, **106**, 2065–2074 (2007).
DOI: 10.1002/app.26444

[6] Pedrazzoli D., Dorigato A., Pegoretti A.: Monitoring the mechanical behaviour of electrically conductive polymer nanocomposites under ramp and creep conditions. Journal of Nanoscience and Nanotechnology, **12**, 4093–4102 (2012).
DOI: 10.1166/jnn.2012.6219

[7] Pedrazzoli D., Dorigato A., Pegoretti A.: Monitoring the mechanical behavior under ramp and creep conditions of electrically conductive polymer composites. Composites Part A: Applied Science and Manufacturing, **43**, 1285–1292 (2012).
DOI: 10.1016/j.compositesa.2012.03.019

[8] Lendlein A., Kelch S.: Shape-memory polymers. Angewandte Chemie International Edition, **41**, 2034–2057 (2002).
DOI: 10.1002/1521-3773(20020617)41:12<2034::AID-ANIE2034>3.0.CO;2-M

[9] Bogue R.: Shape-memory materials: A review of technology and applications. Assembly Automation, **29**, 214–219 (2009).
DOI: 10.1108/01445150910972895

[10] Sun L., Huang W. M., Ding Z., Zhao Y., Wang C. C., Purnawali H., Tang C.: Stimulus-responsive shape memory materials: A review. Materials and Design, **33**, 577–640 (2012).
DOI: 10.1016/j.matdes.2011.04.065

[11] Meng Q., Hu J., Zhu Y., Lu J., Liu Y.: Morphology, phase separation, thermal and mechanical property differences of shape memory fibres prepared by different spinning methods. Smart Materials and Structures, **16**, 1192–1197 (2007).
DOI: 10.1088/0964-1726/16/4/030

[12] Metcalfe A., Desfaits A-C., Salazkin I., Yahia L., Sokolowski W. M., Raymond J.: Cold hibernated elastic memory foams for endovascular interventions. Biomaterials, **24**, 491–497 (2003).
DOI: 10.1016/S0142-9612(02)00362-9

[13] Charlesby A.: Atomic radiation and polymers.Pergamon Press, New York (1960).

[14] Mondal S., Hu J. L., Yong Z.: Free volume and water vapor permeability of dense segmented polyurethane membrane. Journal of Membrane Science, **280**, 427–432 (2006).
DOI: 10.1016/j.memsci.2006.01.047

[15] Kim B. K., Lee S. Y., Xu M.: Polyurethanes having shape memory effects. Polymer, **37**, 5781–5793 (1996).
DOI: 10.1016/S0032-3861(96)00442-9

[16] Gall K., Dunn M. L., Liu Y., Finch D., Lake M., Munshi N. A.: Shape memory polymer nanocomposites. Acta Materialia, **50**, 5115–5126 (2002).
DOI: 10.1016/S1359-6454(02)00368-3

[17] Hu J. L., Ji F. L., Wong Y. W.: Dependency of the shape memory properties of a polyurethane upon thermomechanical cyclic conditions. Polymer International, **54**, 600–605 (2005).
DOI: 10.1002/pi.1745

[18] Wang C. C., Huang W. M., Ding Z., Zhao Y., Purnawali H.: Cooling-/water-responsive shape memory hybrids. Composites Science and Technology, **72**, 1178–1182 (2012).
DOI: 10.1016/j.compscitech.2012.03.027

[19] Lendlein A., Jiang H., Jünger O., Langer R.: Light-induced shape-memory polymers. Nature, **434**, 879–882 (2005).
DOI: 10.1038/nature03496

[20] Jiang H., Kelch S., Lendlein A.: Polymers move in response to light. Advanced Materials, **18**, 1471–1475 (2006).
DOI: 10.1002/adma.200502266

[21] Cho J. W., Kim J. W., Jung Y. C., Goo N. S.: Electroactive shape-memory polyurethane composites incorporating carbon nanotubes. Macromolecular Rapid Communication, **26**, 412–416 (2005).
DOI: 10.1002/marc.200400492

[22] Paik I. H., Goo N. S., Jung Y. C., Cho J. W.: Development and application of conducting shape memory polyurethane actuators. Smart Materials and Structures, **15**, 1476–1482 (2006).
DOI: 10.1088/0964-1726/15/5/037

[23] Yang B., Huang W. M., Li C., Li L., Chor J. H.: Qualitative separation of the effects of carbon nano-powder and moisture on the glass transition temperature of polyurethane shape memory polymer. Scripta Materialia, **53**, 105–107 (2005).
DOI: 10.1016/j.scriptamat.2005.03.009

[24] Leng J., Lv H., Liu Y., Du S.: Electroactivate shape-memory polymer filled with nanocarbon particles and short carbon fibers. Applied Physics Letters, **91**, 144105/1–144105/3 (2007).
DOI: 10.1063/1.2790497

[25] Schmidt A. M.: Electromagnetic activation of shape memory polymer networks containing magnetic nanoparticles. Macromolecular Rapid Communication, **27**, 1168–1172 (2006).
DOI: 10.1002/marc.200600225

[26] Koerner H., Price G., Pearce N., Alexander M., Vaia R. A.: Remotely actuated polymer nanocomposites–stress-recovery of carbon-nanotube-filled thermoplastic elastomers. Nature Materials, **3**, 115–120 (2004).
DOI: 10.1038/nmat1059

[27] Leng J. S., Lan X., Liu Y. J., Du S. Y., Huang W. M., Liu N., Phee S. J., Yuan Q.: Electrical conductivity of thermoresponsive shape-memory polymer with embedded micron sized Ni powder chains. Applied Physics Letters, **92**, 014104/1–014104/3 (2008).
DOI: 10.1063/1.2829388

[28] Leng J. S., Huang W. M., Lan X., Liu Y. J., Du S. Y.: Significantly reducing electrical resistivity by forming conductive Ni chains in a polyurethane shape-memory polymer/carbon-black composite. Applied Physics Letters, **92**, 204101/1–204101/3 (2008).
DOI: 10.1063/1.2931049

[29] Narendra Kumar U., Kratz K., Behl M., Lendlein A.: Shape-memory properties of magnetically active triple-shape nanocomposites based on a grafted polymer network with two crystallizable switching segments. Express Polymer Letters, **6**, 26–40 (2012).
DOI: 10.3144/expresspolymlett.2012.4

[30] Fan K., Huang W. M., Wang C. C., Ding Z., Zhao Y., Purnawali H., Liew K. C., Zheng L. X.: Water-responsive shape memory hybrid: Design concept and demonstration. Express Polymer Letters, **5**, 409–416 (2011).
DOI: 10.3144/expresspolymlett.2011.40

[31] Behl M., Lendlein A.: Shape-memory polymers. Materials Today, **10**, 20–28 (2007).
DOI: 10.1016/S1369-7021(07)70047-0

[32] Yong Y., Matsubara S., Xiong L., Hayakawa T., Nogami M.: Solvothermal synthesis of multiple shapes of silver nanoparticles and their SERS properties. Journal of Physical Chemistry C, **111**, 9095–9104 (2007).
DOI: 10.1021/jp068859b

[33] Dorigato A., D'Amato M., Pegoretti A.: Thermo-mechanical properties of high density polyethylene – fumed silica nanocomposites: Effect of filler surface area and treatment. Journal of Polymer Research, **19**, 9889/1–9889/11 (2012).
DOI: 10.1007/s10965-012-9889-2

[34] Dorigato A., Pegoretti A.: The role of alumina nanoparticles in epoxy adhesives. Journal of Nanoparticle Research, **13**, 2429–2441 (2011).
DOI: 10.1007/s11051-010-0130-0

[35] Dorigato A., Pegoretti A. P., Penati A.: Effect of the polymer–filler interaction on the thermo-mechanical response of polyurethane-clay nanocomposites from blocked prepolymer. Journal of Reinforced Plastics and Composites, **30**, 325–335 (2011).
DOI: 10.1177/0731684410396599

[36] Dorigato A., Pegoretti A., Bondioli F., Messori M.: Improving epoxy adhesives with zirconia nanoparticles. Composite Interfaces, **17**, 873–892 (2010).
DOI: 10.1163/092764410X539253

[37] Pegoretti A., Dorigato A., Brugnara M., Penati A.: Contact angle measurements as a tool to investigate the filler–matrix interactions in polyurethane–clay nanocomposites from blocked prepolymer. European Polymer Journal, **44**, 1662–1672 (2008).
DOI: 10.1016/j.eurpolymj.2008.04.011

[38] Liu G., Zhang H., Zhang D-J., Zhang H., Zhang Z., An X-F., Yi X-S.: On depression of glass transition temperature of epoxy nanocomposites. Journal of Materials Science, **47**, 6891–6895 (2012).
DOI: 10.1007/s10853-012-6633-6

[39] Preghenella M., Pegoretti A., Migliaresi C.: Thermo-mechanical characterization of fumed silica-epoxy nanocomposites. Polymer, **46**, 12065–12072 (2005).
DOI: 10.1016/j.polymer.2005.10.098

eXPRESS Polymer Letters Vol.7, No.8 (2013) 683–689
Available online at www.expresspolymlett.com
DOI: 10.3144/expresspolymlett.2013.65

Needleless electro-spun nanofibers used for filtration of small particles

J. Li[1,2], *F. Gao*[1], *L. Q. Liu*[1], *Z. Zhang*[1*]

[1]National Center for Nanoscience and Technology, 100190 Beijing, China
[2]University of Chinese Academy of Sciences, 100049 Beijing, China

Received 12 March 2013; accepted in revised form 28 April 2013

Abstract. A composite aerosol filter media was prepared by depositing nanofibers on the non-woven fabrics substrate using needleless electrospinning technique. The polyvinyl alcohol nanofibers with mean diameters of ca. 100 nm were used as top layers. The filtration performance was evaluated by measuring the filtration of sodium chloride nanoparticles (75±20 nm) through the filters. It was found that the filtration efficiency of the composite filter media for nanoparticles was increased along with the thickness of nanofibers mats which was controlled by the collection time during the electrospinning. The multi-layer arrangement for fabrication of the composite filter can achieve high filtration efficiency (up to 99.95%) which was comparable to commercial high efficiency particulate air filters but with higher quality factor and less mass.

Keywords: *nanomaterials, nanofibers, needleless electrospinning, filtration, nanoparticles*

1. Introduction

Air pollution becomes more and more serious especially haze pollution [1, 2]. Haze is caused by fine particles that scatter and absorb light before it reaches the observer [3]. In particular, airborne fine particulate matters especially PM 2.5 (defined as particulate matters with an aerodynamic diameter $\leq$2.5 μm) are one of the most serious sources of fine particles. PM 2.5 and its extracts can induce many human diseases [4–7]. So, there is a great need for the development of filtration technologies to prevent harmful nanoparticles affecting human healthy. One of the most valid methods of removing particles from a gas stream is via fibrous filters. According to filtration theories [8], the smaller diameter of fibers leads to better filtration efficiency.

A small diameter and large surface area of nanofibers can be achieved by the electrospinning method. The nanofiber mats have a light weight, a high permeability and a large surface area which make them appropriate for filtration and separation applications. Much work has been done in the improvement of the filtration capability of media containing electrospun nanofibers [9–14]. In spite of high filtration efficiency obtained in their works, electrospun nanofibers were obtained in low yield using needle electrospinning setup. The needle electrospinning has a very low production rate and the spinneret was frequently clogged during electrospinning [15, 16]. Recently, needleless electrospinning appeared with the aim of producing nanofibers on a large scale [17–19]. Numerous jets are formed simultaneously from the spinneret without the influence of capillary effect, which greatly enhanced the productivity of nanofibers.

Poly(vinyl alcohol) (PVA) is a hydrophilic polymer with high biocompatibility, non-toxicity, good chemical and thermal stability [20, 21]. It can be easily modified to incorporate functional groups and reacted with different crosslinking agents to form a

---

[*]Corresponding author, e-mail: zhong.zhang@nanoctr.cn

gel [22]. In this study, the needleless electrospinning equipment was set up with a stainless steel roller as spinneret. The PVA nanofibers with mean diameters of ca. 100 nm were deposited on nonwoven fabrics to form a composite filter material by needleless electrospinning. It showed a high efficiency and low pressure drop for the filtration of nano-sized sodium chloride (NaCl) aerosols while depositing a thin layer of nanofibers (thickness of 2.3 μm obtained by electrospinning only for 10 s). The multi-layer arrangement of nanofibers mats can achieve high filtration efficiency (up to 99.95%). That was comparable to high efficiency particulate air (HEPA) filters but with much higher quality factor and less mass.

2. Materials and methods

2.1. Materials

PVA, (typical M_w of 118 000–124 000, 86–90% hydrolyzed) was commercial from Zhong Ke Guo Chang Technology Co., Ltd. Beijing, China. The non-woven polypropylene (PP) fabrics with thickness of about 95 μm were supplied by Handan Hengyong Protective & Clean Products Co., Ltd. Handan, China. The commercial high efficiency particulate air (HEPA) filter media (CZU500W) were purchased from Chongqing Paper Industry Research and Design Institute Co., Ltd. China. The deionized water used in all preparations was produced by a Millipore milli-Q water purification system.

2.2. Needleless electrospinning and the preparation of composite filter materials

Figure 1 illustrates the overall procedure for the fabrication of the composite filter media based on needleless electrospinning. Needleless electrospinning began to attract attentions since Chaloupek *et al.*'s invention [17] on using a metal roller as spinneret. The setup in our laboratory is shown in Figure 1c. A stainless steel roller was put on a polyte-

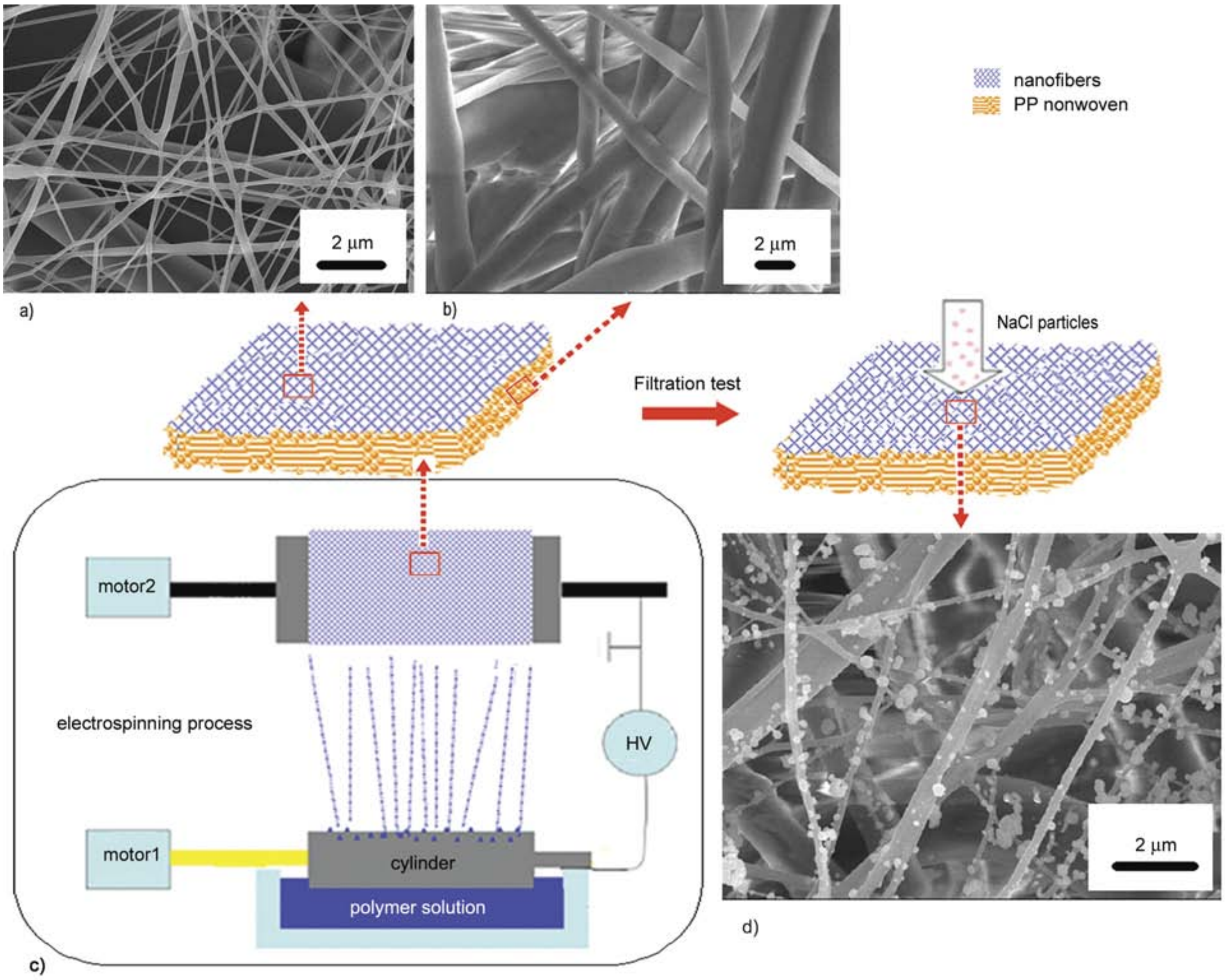

Figure 1. Schematic diagrams illustrating the fabrication of the composite filter materials. The SEM image of the composite membrane (a), PP substrate (b), the electrospinning process (c) and the SEM image of the composite membrane after filtration test (d).

trafluoroethylene solution tank which was used as the generator of jets. The polymer solution was loaded onto the upper surface when the rotated roller was partially immersed into polymer solution. A large number of jets can be generated from the roller surface after applying a high voltage. Another grounded roller was used for collecting electrospinning nanofibers.

Different concentrations (from 6 to 10 wt%) of PVA solutions were prepared by dissolving the PVA polymer in deionized water at 60°C, and completely dissolved by stirring. PVA nanofibers prepared by needleless electrospinning have been studied by many researchers [23]. After the polymer solutions were added to the solution tank, a voltage of 70 kV (Spellman SL130 P300) was supplied on the positive roller for electrospinning. The distance between positive roller and collect roller was fixed at 12 cm. The nanofibers were deposited on the non-woven PP substrate which covered the collect roller to form the composite filter. It was dried under vacuum condition to remove the remaining solvent for the filtration test. PVA solutions can form physical gels [22] which have fine adhesive properties. After the evaporation of solvents, PVA nanofibers can well fasten on the non-woven PP fabrics without slipping away.

2.3. Characterization

The conductivity and viscosity of PVA solutions were measured by the conductivity meter (DDS-11A, Shanghai REX Instrument Factory, China) and the HAAKE Rotational Rheometer (MARS2), respectively. The surface tension was tested by water contact angle measurement (DSA100, Germany). The morphologies of the nanofibers were observed by the scanning electron microscope (SEM, S4800, HITACHI, Japan). Prior to SEM measurement, the specimens were sputtered with gold to avoid charge accumulations. The fibers mats were weighed using the electronic balance (WA 10005, Shanghai Fangrui Istrument Co., Ltd. China). The thickness of the membrane was measured by the thickness gauge (CH-12.7-STSX, Shanghai Chuanlu Mesuring Tools Co., Ltd. China). A TSI Automated Filter Tester (Model 8130) was used to measure the filtration efficiency and pressure drop. TSI 8130 could generate neutralized monodisperse solid NaCl aerosols with a number median diameter of 75±20 nm. The geometric standard deviation was smaller than 1.83. The NaCl aerosols were flown through the filter with a continuous airflow fixed at 32 L·min^{-1}. The testing time of each sample was 10 s.

3. Results and discussion

3.1. Needleless electrospinning of PVA nanofibers

Different concentrations (from 6 to 10 wt%) of PVA solutions were prepared for sources of needleless electrospinning. The parameters such as viscosity, conductivity and surface tension were increased along with the polymeric concentration which can be seen in Figure 2 and the inserted table. The productivity of nanofibers can be achieved 10 g/h tested from the electronic balance. Figure 3 shows the SEM images of nanofibers spun under different concentrations on PP substrate. It can be seen that the morphologies and diameters of the electrospun nanofibers obviously depended on the polymer concentrations. Discontinuous fibers and a large number of droplets were obtained when the concentration was 6 wt%, some beads can be observed while at 7 wt% as shown in Figure 3a, 3b. That was caused by the little entangled polymer in lower concentration solutions which was discussed in detail in previous studies [24, 25]. However, uniform fibers were obtained when it was higher than 7 wt%. The diameters of fibers were increased along with the increasing of polymeric concentration which in range of ca. 91±21 nm for 8 wt%, 104±24 nm for 9 wt% and 117±27 nm for 10 wt% as shown in Figure 3f. The

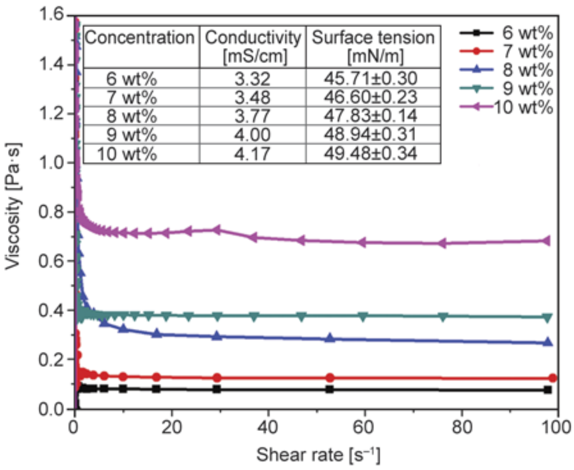

Concentration	Conductivity [mS/cm]	Surface tension [mN/m]
6 wt%	3.32	45.71±0.30
7 wt%	3.48	46.60±0.23
8 wt%	3.77	47.83±0.14
9 wt%	4.00	48.94±0.31
10 wt%	4.17	49.48±0.34

Figure 2. The viscosity versus shear rate curves of PVA solutions (the concentrations was given in figure). The inserted table shows the conductivity and surface tension of PVA solutions.

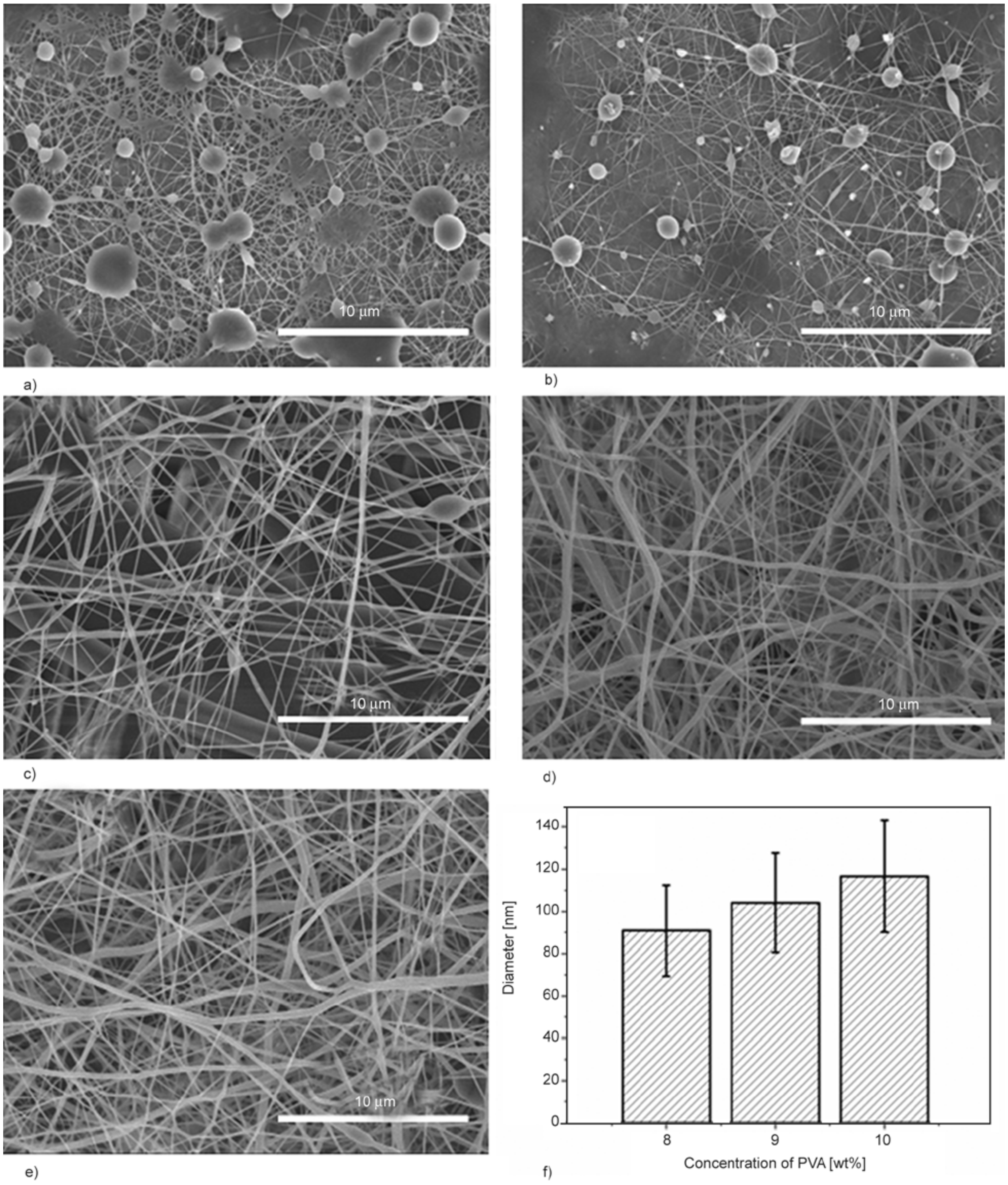

Figure 3. The SEM micrographs of PVA nanofibers spun under different concentrations on PP substrate: (a) 6 wt%; (b) 7 wt%; (c) 8 wt%; (d) 9 wt%; (e) 10 wt%. (f) The effect of PVA concentration on the diameter distribution. (The average diameter of nanofibers were measured from 100 random nanofibers on SEM micrographs using ImageJ software. Error bars indicated the standard deviation.)

thicker fibers were obtained at higher concentration. The explanation was that there were more chain entanglements and less chain mobility in higher concentration solutions. In view of the fine and uniformity of nanofibers, PVA (8 wt%) solution was used for the following study.

3.2. The composite filter materials for air filtration

The nonwoven substrate with diameter of larger than 2 µm was used to collect nanofibers. It is intuitive to assume that the thickness of nanofibers depended on the electrospinning time. The layers of

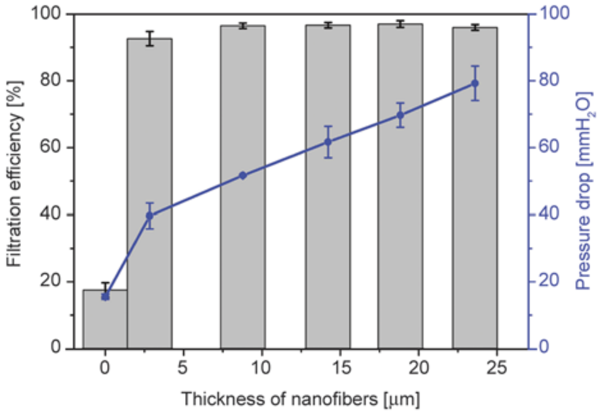

Figure 4. The filtration efficiency and drop pressure of nanofibers versus the thickness of nanofibers. (Each data point represents an average obtained from testing of five separate mats. Error bars indicate the standard deviation).

nanofibers with thickness of about 2.3, 6.3, 13.2, 18.8, 24.6 µm were obtained by the electrospinning time of 10, 30, 60, 90, 120 s, respectively. The composite filter membranes with different thicknesses of nanofibers (2.3, 6.3, 13.2, 18.8, 24.6 µm) were designated as Nn (N1, N2, N3, N4 and N5), respectively. The SEM images of composite membranes and PP substrate were shown in Figure 1a and 1b, respectively. The filtration performances are generally characterized by two basic parameters: collection efficiency and pressure drop [26]. Figure 4 shows the filtration efficiency and drop pressure of composite membranes versus the thickness of nanofibers. The PP non-woven fabrics showed lower filtration efficiency at 17.5%, while it rose dramatically and reached above 92% after compositing with nanofibers. The filtration efficiencies of the composite membranes versus increased thickness of nanofibers (2.3, 6.3, 13.2, 18.8, 24.6 µm) were 92.61, 96.44, 96.63, 96.98 and 95.95%, respectively (Figure 4). Obviously, the filtration efficiency increased along with the increasing of thickness. The filtration efficiencies can be significantly improved by compositing with a thin layer of nanofibers (only 2.3 µm obtained by electrospinning for 10 s).

3.3. The filtration performances of multilayer nanofibers filter

In order to reach higher efficiency, the above filter membranes were stacked up in different ways. The multi-layer nanofibers filter has been proposed which could realize the higher efficiency and save pressure drop in previous study [27]. The multilayer membranes (3*N1, 2*N2, N2+N3, 2*N3) and (PP + Nn) were designed as shown in the left inserted image of Figure 5a. The composite filter membranes showed filtration efficiency higher than 95% after stacked with the same layer of PP, while it showed at about 35% for two layers of PP fabrics as can be seen in Figure 5a. The efficiencies of the multilayer membranes (3*N1, 2*N2, N2+N3, 2*N3) were reached at 99.95, 99.60, 99.63, 99.78% obviously observed in Figure 5a. The filtration of nanoparticles using commercial HEPA was also tested under the same conditions. It shows the filtration efficiency of 99.95% but much higher pressure drop than the multi-layer nanofibers filters in the right inserted image of Figure 5a.

A good filtration performance requires higher efficiency but lower pressure drop. The quality factor (*QF*) [28] as a comprehensive parameter for measuring the filtration performance can be deduced from Equation (1):

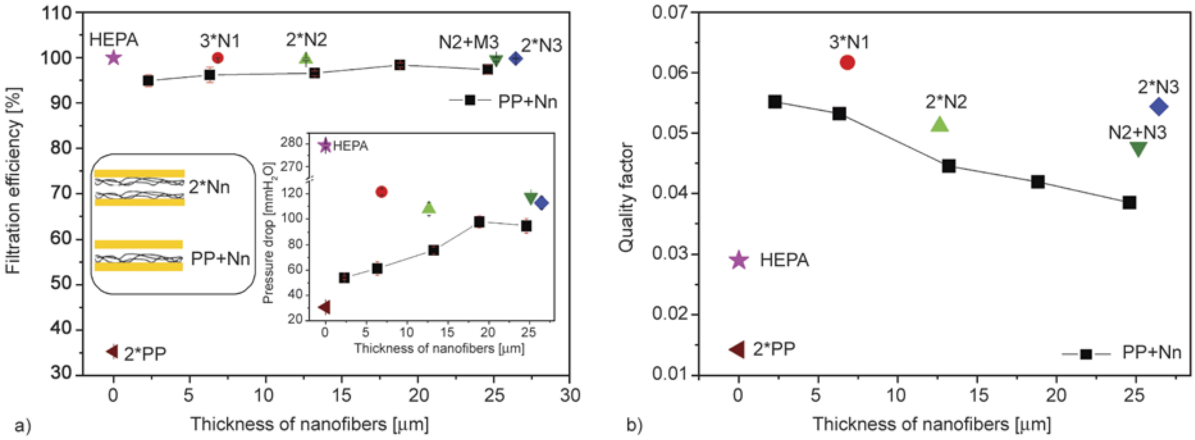

Figure 5. The filtration efficiency and drop pressure (inserted) (a) and quality factor of multi-layer composite filter media versus the thickness of nanofibers (b)

$$QF = -\frac{\ln(1-\eta)}{\Delta P} \tag{1}$$

where η and ΔP are the filtration efficiency and pressure drop, respectively. The *QF* of the above filter media was calculated from using Equation (1) as shown in Figure 5b. The *QF* of multi-layer was much higher than HEPA. It was suggested that the filter media in our system showed better performance than HEPA for the filtration of nanoparticles. It might be used for filtration of small particles such as viruses and bacteria.

4. Conclusions

Uniform and continuous fibers can be obtained while the concentration was not lower than 8 wt% by needleless electrospinning. The PVA nanofiber mats were collected on non-woven PP fabrics to form the composite filter membranes. The filtration efficiencies can be significantly improved by compositing with a thin layer of nanofibers (only 2.3 μm obtained by electrospinning for 10 s). It increased with the thickness of nanofibers which were controlled by the electrospinning time. The multi-layer nanofibers showed high filtration efficiency (99.95%) for the nanoparticles but much lower pressure drop and higher quality factor than commercial HEPA.

Acknowledgements

This project was jointly supported by a key international collaboration project (Grant No. 2011DFR50200) of the Ministry of Science and Technology of China, and the National Nature Science Foundation of China (Grant Nos. 11225210 and 51073044).

References

[1] Ji D., Wang Y., Wang L., Chen L., Hu B., Tang G., Xin J., Song T., Wen T., Sun Y., Pan Y., Liu R.: Analysis of heavy pollution episodes in selected cities of northern China. Atmospheric Environment, **50**, 338–348 (2012). DOI: 10.1016/j.atmosenv.2011.11.053

[2] Ma J., Xu X., Zhao C., Yan P.: A review of atmospheric chemistry research in China: Photochemical smog, haze pollution, and gas-aerosol interactions. Advances in Atmospheric Sciences, **29**, 1006–1026 (2012). DOI: 10.1007/s00376-012-1188-7

[3] Watson J. G.: Visibility: Science and regulation. Journal of the Air and Waste Management Association, **52**, 628–713 (2002). DOI: 10.1080/10473289.2002.10470813

[4] Wei A., Meng Z.: Evaluation of micronucleus induction of sand dust storm fine particles ($PM_{2.5}$) in human blood lymphocytes. Environmental Toxicology and Pharmacology, **22**, 292–297 (2006). DOI: 10.1016/j.etap.2006.04.003

[5] Nikasinovic L., Just J., Sahraoui F., Seta N., Grimfeld A., Momas I.: Nasal inflammation and personal exposure to fine particles $PM_{2.5}$ in asthmatic children. Journal of Allergy and Clinical Immunology, **117**, 1382–1388 (2006). DOI: 10.1016/j.jaci.2006.03.023

[6] Morgenstern V., Zutavern A., Cyrys J., Brockow I., Gehring U., Koletzko S., Bauer C. P., Reinhardt D., Wichmann H-E., Heinrich J.: Respiratory health and individual estimated exposure to traffic-related air pollutants in a cohort of young children. Journal of Occupational and Environmental Medicine, **64**, 8–16 (2007). DOI: 10.1136/oem.2006.028241

[7] de Hartog J. J., Lanki T., Timonen K. L., Hoek G., Janssen N. A., Ibald-Mulli A., Peters A., Heinrich J., Tarkiainen T. H., van Grieken R., van Wijnen J. H., Brunekreef B., Pekkanen J.: Associations between $PM_{2.5}$ and heart rate variability are modified by particle composition and beta-blocker use in patients with coronary heart disease. Environmental Health Perspectives, **117**, 105–111 (2009). DOI: 10.1289/ehp.11062

[8] Pich J.: Theory of aerosol filtration by fibrous and membrane filters. Academic Press, London (1966).

[9] Zhang S., Shim W. S., Kim J.: Design of ultra-fine nonwovens via electrospinning of Nylon 6: Spinning parameters and filtration efficiency. Materials and Design, **30**, 3659–3666 (2009). DOI: 10.1016/j.matdes.2009.02.017

[10] Yun K. M., Hogan C. J., Matsubayashi Y., Kawabe M., Iskandar F., Okuyama K.: Nanoparticle filtration by electrospun polymer fibers. Chemical Engineering Science, **62**, 4751–4759 (2007). DOI: 10.1016/j.ces.2007.06.007

[11] Wang N., Wang X., Ding B., Yu J., Sun G.: Tunable fabrication of three-dimensional polyamide-66 nanofiber/nets for high efficiency fine particulate filtration. Journal of Materials Chemistry, **22**, 1445–1452 (2012). DOI: 10.1039/c1jm14299b

[12] Tsai P. P., Schreuder-Gibson H., Gibson P.: Different electrostatic methods for making electret filters. Journal of Electrostatics, **54**, 333–341 (2002). DOI: 10.1016/S0304-3886(01)00160-7

[13] Patanaik A., Jacobs V., Anandjiwala R. D.: Performance evaluation of electrospun nanofibrous membrane. Journal of Membrane Science, **352**, 136–142 (2010). DOI: 10.1016/j.memsci.2010.02.009

[14] Hoover L. A., Schiffman J. D., Elimelech M.: Nanofibers in thin-film composite membrane support layers: Enabling expanded application of forward and pressure retarded osmosis. Desalination, **308**, 73–81 (2013). DOI: 10.1016/j.desal.2012.07.019

[15] Yu D. G., Zhou J., Chatterton N. P., Li Y., Huang J., Wang X.: Polyacrylonitrile nanofibers coated with silver nanoparticles using a modified coaxial electrospinning process. International Journal of Nanomedicine, **7**, 5725–5732 (2012).
DOI: 10.2147/IJN.S37455

[16] Yu D. G., Li X. Y., Wang X., Chian W., Liao Y. Z., Li Y.: Zero-order drug release cellulose acetate nanofibers prepared using coaxial electrospinning. Cellulose, **20**, 379–389 (2013).
DOI: 10.1007/s10570-012-9824-z

[17] Chaloupek J., Jirsak O., Kotek V., Lukas D., Martinova L., Sanetrnik F.: A method of nanofibres production from a polymer solution using electrostatic spinning and a device for carrying out the method. EP Patent 1673493, EU (2009).

[18] Niu H., Lin T., Wang X.: Needleless electrospinning. I. A comparison of cylinder and disk nozzles. Journal of Applied Polymer Science, **114**, 3524–3530 (2009).
DOI: 10.1002/app.30891

[19] Wu D., Huang X., Lai X., Sun D., Lin L.: High throughput tip-less electrospinning via a circular cylindrical electrode. Journal of Nanoscience and Nanotechnology, **10**, 4221–4226 (2010).
DOI: 10.1166/jnn.2010.2194

[20] Zheng H., Du Y., Yu J., Huang R., Zhang L.: Preparation and characterization of chitosan/poly(vinyl alcohol) blend fibers. Journal of Applied Polymer Science, **80**, 2558–2565 (2001).
DOI: 10.1002/app.1365

[21] Kim C. K., Kim B. S., Sheikh F. A., Lee U. S., Khil M. S., Kim H. Y.: Amphiphilic poly(vinyl alcohol) hybrids and electrospun nanofibers incorporating polyhedral oligosilsesquioxane. Macromolecules, **40**, 4823–4828 (2007).
DOI: 10.1021/Ma070056e

[22] Hodge R., Edward G. H., Simon G. P.: Water absorption and states of water in semicrystalline poly(vinyl alcohol) films. Polymer, **37**, 1371–1376 (1996).
DOI: 10.1016/0032-3861(96)81134-7

[23] Cengiz F., Dao T. A., Jirsak O.: Influence of solution properties on the roller electrospinning of poly(vinyl alcohol). Polymer Engineering and Science, **50**, 936–943 (2010).
DOI: 10.1002/pen.21599

[24] McKee M. G., Wilkes G. L., Colby R. H., Long T. E.: Correlations of solution rheology with electrospun fiber formation of linear and branched polyesters. Macromolecules, **37**, 1760–1767 (2004).
DOI: 10.1021/ma035689h

[25] Shenoy S. L., Bates W. D., Frisch H. L., Wnek G. E.: Role of chain entanglements on fiber formation during electrospinning of polymer solutions: Good solvent, non-specific polymer–polymer interaction limit. Polymer, **46**, 3372–3384 (2005).
DOI: 10.1016/j.polymer.2005.03.011

[26] Matteson M. J., Orr C.: Filtration: Principles and practices. Marcel Dekker, New York (1987).

[27] Leung W. W. F., Hung C. H., Yuen P. T.: Effect of face velocity, nanofiber packing density and thickness on filtration performance of filters with nanofibers coated on a substrate. Separation and Purification Technology, **71**, 30–37 (2010).
DOI: 10.1016/j.seppur.2009.10.017

[28] Viswanathan G., Kane D. B., Lipowicz P. J.: High efficiency fine particulate filtration using carbon nanotube coatings. Advanced Materials, **16**, 2045–2049 (2004).
DOI: 10.1002/adma.200400463

eXPRESS Polymer Letters Vol.7, No.8 (2013) 690–702
Available online at www.expresspolymlett.com
DOI: 10.3144/expresspolymlett.2013.66

A novel strategy towards cyclic aliphatic (co)polyesters

Ch. Gao[1], *Y. Li*[1], *J. Chi*[1], *Ph. Lecomte*[2], *R. Jerome*[2], *Ch. Jerome*[2], *L. Lei*[1], *H. Li*[1*]

[1]Department of Polymer Materials and Engineering, Liaoning SHIHUA University, 113001 Fushun, P. R. China
[2]Center for Education and Research on Macromolecules (CERM), University of Liege, 4000 Liege, Belgium

Received 25 February 2013; accepted in revised form 3 May 2013

Abstract. This feature article focuses on a novel strategy towards macrocyclic (co)polyesters that combines controlled ring-opening polymerization of lactones initiated by a cyclic tin(IV) dialkoxide and intramolecular cyclization by photo-cross-linking of pendant unsaturations next to the propagating sites. No linear species is ever involved in the polymerization and permanent cyclization steps, which allows higher molecular weight macrocycles to be prepared with high efficiency and no need for further purification. Moreover, this synthetic route is very flexible to the point where macrocyclic polyesters with more complex although well-defined architectures, such as tadpole-shaped and sun-shaped copolyesters, can be tailored. Synthesis of well-defined eight-shaped polyesters and twin tadpole-shaped copolymers has also been explored by using a spirocyclic tin(IV) alkoxides as an initiator. When functional lactones were introduced, the 'click' copper-mediated cycloaddition [3+2] reaction was utilized to make the eight-shaped and twin tadpole-shaped copolyesters amphiphilic.

Keywords: *polymer synthesis, ring-opening polymerization, cyclic polyesters, cross-linking by UV irradiation, 'click' chemistry*

1. Introduction

Much attention was paid to cyclic polymers and much effort was devoted to their design and synthesis for the last decades because of distinct properties compared to the linear counterparts, such as glass transition temperature, order-disorder transition, hydrodynamic volume, intrinsic viscosity, and enhancement of fluorescence [1–4]. This interest is motivated by the appealing topology of the macrocycles, the stringent restrictions on the backbone conformation, and the absence of chain ends. The discovery of natural DNA ring [5], where the two strands of the double helix form a high order link, has stimulated the chemists to embark on the macromolecular engineering of cyclic polymers. It must be noted that living organisms produce numerous cyclic compounds, such as oligopeptides, polypeptides, and DNAs, whose molecular weight and ring size can change extensively. In protozoa, relatively small rings containing approximately 400 base pairs (equivalent to 2400 atoms in the ring) are known that have a molar mass of $1.2\cdot10^5$ g/mol. Importantly, it was found recently that cyclic DNA can be prepared *in-vitro* by using the enzyme ligase [6]. Therefore, synthesis of well-defined macrocycles, extending over a large range of macromolecular characteristic features is of the utmost importance for improving basic knowledge and ultimately mimicking compounds with a specific biological activity.

The main approaches to macrocycles are based on the end-to-end ring-closure (coupling) of homo- or hetero-difunctional linear precursors under very high dilution by any reaction known in the state of the art, such as nucleophilic substitution [7, 8], addition on unsaturations [9–13], metathesis reaction [14–16], amidification [17], 'click' reaction [18–22], and electrostatic interaction followed by covalent

---

[*] Corresponding author, e-mail: haiying.li@hotmail.com

fixation [23, 24]. Although the linear precursors prepared by living/controlled polymerization are well-defined, the unavoidable competition between intramolecular cyclization and intermolecular extension is the major problem to be solved. In order to increase the cyclization yield at the expense of the detrimental intermolecular polycondensation, the intramolecular cyclization must be performed at very high dilution. Nevertheless, even under optimized conditions, the efficiency of cyclization is inversely proportional to the molecular weight of the precursor. Anyway, the cyclization is not very effective, contamination by undesired polycondensates is a concern and requires an additional and tedious step of purification by fractionation. Therefore, the quest for more efficient cyclization methods remains a challenging priority, even though several clever strategies have been explored as reported in the literatures [25–28]. Remarkably, Bielawski *et al*. have initiated the ring-opening metathesis polymerization of cyclooctene by a cyclic ruthenium carbene, so leading to macrocyclic poly(cyclooctene) ($M_n = 6\cdot10^5$–$1.1\cdot10^6$ g/mol) by intramolecular chain transfer. Polymerization can be conducted at high concentration, even in the bulk and macrocycles with higher molecular weight can be achieved. Another route reported by He *et al*. [26] for the synthesis of macrocycles, relies on the controlled radical polymerization of methyl acrylate (MA) in THF (10 wt%) by using a cyclic initiator with a weak (C-S) bond upon ^{60}Co γ-ray irradiation. Cyclic poly(methyl acrylate) was accordingly formed with a predetermined molecular weight ($M_n = 8.2\cdot10^3$ g/mol) without high dilution by intramolecular chain termination. Kricheldorf *et al*. [27] initiated ring-opening polymerization of lactones and lactides by a series of cyclic tin dialkoxide and the growing chains are macrocycles linked by an endocyclic living tin dialkoxide. In a typical example, cyclization was stabilized by the insertion of 1,3-dithian-2-one into the Sn-O bond with formation of macrocyclic precursor. Finally, the cyclic 2-stanna-1,3-dithiane was selectively eliminated from the precursor. No need for high dilution is a substantial advantage [28]. Culkin *et al*. [29] reported a zwitterionic strategy for the kinetically controlled synthesis of high-molecular-weight cyclic PLA with narrow polydispersity by using N-hetreocyclic carbene as an initiator.

This feature article aims at summarizing recent developments in synthesizing macrocyclic poly(ε-caprolactone) with well-defined architectures designed through a novel strategy that combines controlled ring-opening polymerization of lactones initiated by a cyclic tin(IV) dialkoxide and intramolecular cyclization by photo-cross-linking of pendant unsaturations next to the propagating sites. No linear oligomer or polymer is ever involved in the polymerization and permanent cyclization steps, which allows higher molecular weight macrocycles to be prepared with high efficiency. Moreover, this synthetic route is very flexible to the point where macrocyclic polyesters with more complex although well-defined architectures, such as tadpole-shaped and sun-shaped copolyesters, can be tailored. When a spirocyclic tin(IV) alkoxides were employed as an initiator, well-defined eight-shaped polyesters and twin tadpole-shaped amphiphilic copolymers has been readily made available.

2. Synthesis of macrocyclic poly(ε-caprolactone)

The strategy for synthesis of cyclic PCL is based on the ring-opening polymerization of ε-caprolactone initiated by cyclic tin dialkoxides (DSDOP), followed by the sequential polymerization of a few functional units of α-(1-acryloxyethyl)-ε-caprolactone (αAεCL) [30]. As result of a coordination-insertion polymerization mechanism, no linear species is formed at any stage of the process. Moreover, polymerization being controlled, the molecular weight can be predicted by the monomer/initiator molar ratio and the monomer conversion. The growing chains are closed by two endocyclic tin alkoxides at least as long as they are protected from hydrolysis, which means the precursors to be stabilized are a living cyclic PCL (**CP**). Before cyclization, a sample was withdrawn and hydrolyzed into the parent linear copolyester ($M_{n,NMR} = 2.6\cdot10^4$ g/mol, $M_{n,SEC} = 2.4\cdot10^4$ g/mol, $M_w/M_n = 1.45$) for characterization. The intramolecular cross-linking of the pendant acrylic unsaturations of αAεCL units next to the propagating sites is performed by UV (350–420 nm, 1000 W) irradiation to result in macrocyclic polyesters ($M_{n,NMR} = 2.64\cdot10^4$ g/mol, $M_{n,SEC} = 2.08\cdot10^4$ g/mol, $M_w/M_n = 1.45$) free of any tin alkoxide after hydrolysis (Figure 1). ^{1}HNMR spectroscopy proved at least part of the double bonds in

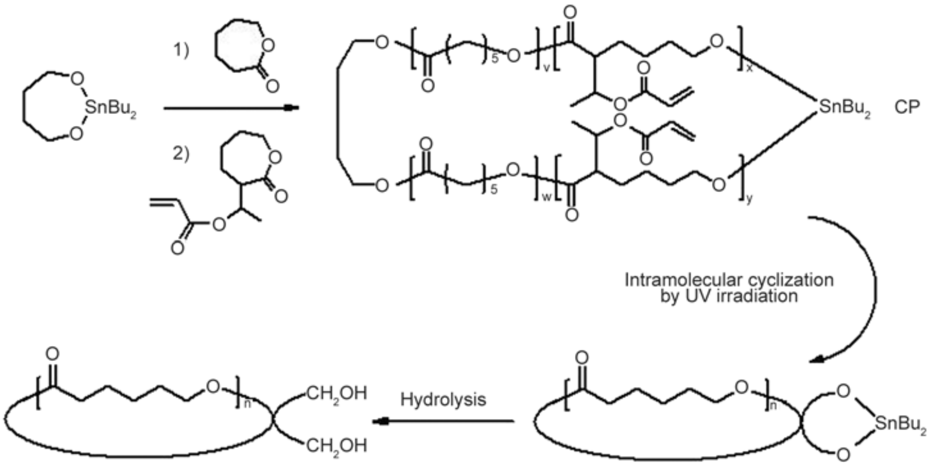

Figure 1. New strategy for the synthesis of macrocyclic polyester free from tin alkoxides

one block of the PCL chains react with double bonds in the second block. Remarkably, the concentration of the chains ($2.8\cdot10^{-4}$ M or ~0.78 wt%) at which the UV cyclization has been carried out, is at least one order of magnitude higher compared to cyclization of linear precursors ($<10^{-5}$ M). The average numbers of acrylic unsaturations per chain are key parameters for the success of cyclization. Indeed, gelation occurs as result of intermolecular cross-linking when either the chain concentration ($\geq5.0\cdot10^{-3}$ M) or the number of acrylic units (more than 30) is too high. In contrast, whenever the average number of unsaturation is too low (less than 7), the apparent molecular weight measured by SEC remains unchanged, which indicated that intramolecular cross-linking does not take place and that no chain degradation is triggered by UV irradiation. Only chains of a medium molecular weight ($M_{n,theor.} = 2.6\cdot10^4$ g/mol) have been considered in relation to feasible characterization by NMR spectroscopy.

The parameter $<G>$, i.e., the ratio of the molecular weights at the maximum of the elution peaks [$M_{p,SEC}$(cyclic)/$M_{p,SEC}$(linear)], is 0.76 and the ratio of the intrinsic viscosity of the polyester, g, ($g = [\eta]_{cyclic}/[\eta]_{linear}$) is 0.69 in toluene at 25°C, in agreement with data published for other cyclic polymers [1]. Cyclization of PCL ($M_{n,NMR} = 2.64\cdot10^4$ g/mol) has only a minor effect on T_g, in contrast to the important impact on crystallization. Indeed, the melting temperature (T_m) of cyclic PCL decreased by 7°C compared to that of the linear counterpart and the degree of crystallinity (X_c) by at least a factor of two.

One advantage of the novel strategy for the synthesis of macrocycles is that there is no linear intermediate at any stage of the process, such that macrocyclic polyesters free of any knot are prepared. Indeed, whenever macrocycles are synthesized from a linear precursor, chains of high enough molecular weight can be entangled leading to physical cross-links or knots that impact the macroscopic properties of the macrocycles [31]. Moreover, the statistics of the cyclization is favourably changed because the probability for intra reaction (P_{intra}) is higher when the precursor is cyclic rather than linear, as result of the permanently close vicinity of the unsaturations to be crosslinked. Clearly, the new strategy is very well-suited to high molecular weight chains, whose macrocyclization from linear precursors is very challenging. The independence of P_{intra} on the chain molecular weight is the key feature, which makes the cyclization to depend mainly on the reactivity of the unsaturated units. In parallel, the probability for inter-reactions decreases upon increasing molecular weight which accounts for high cyclization yield can be observed at higher concentration.

3. Synthesis of functional ciclic copolyesters and amphiphilic sun-shaped copolymers

3.1. Functional cyclic copolyesters

In order to make a cyclic functional copolyesters available, a comonomer containing a protected hydroxyl group [32], i.e., γ-triethylsilyloxy-ε-caprolactone (γ-Et$_3$SiOεCL), has been random copolymerized with ε-caprolactone initiated by cyclic DSDOP in toluene, followed by the addition and sequential polymerization of a few units of αAεCL with formation of a cyclic precursor (**CP**) as shown in Figure 2, poly(γ-Et$_3$SiOεCL-co-εCL-b-αAεCL)

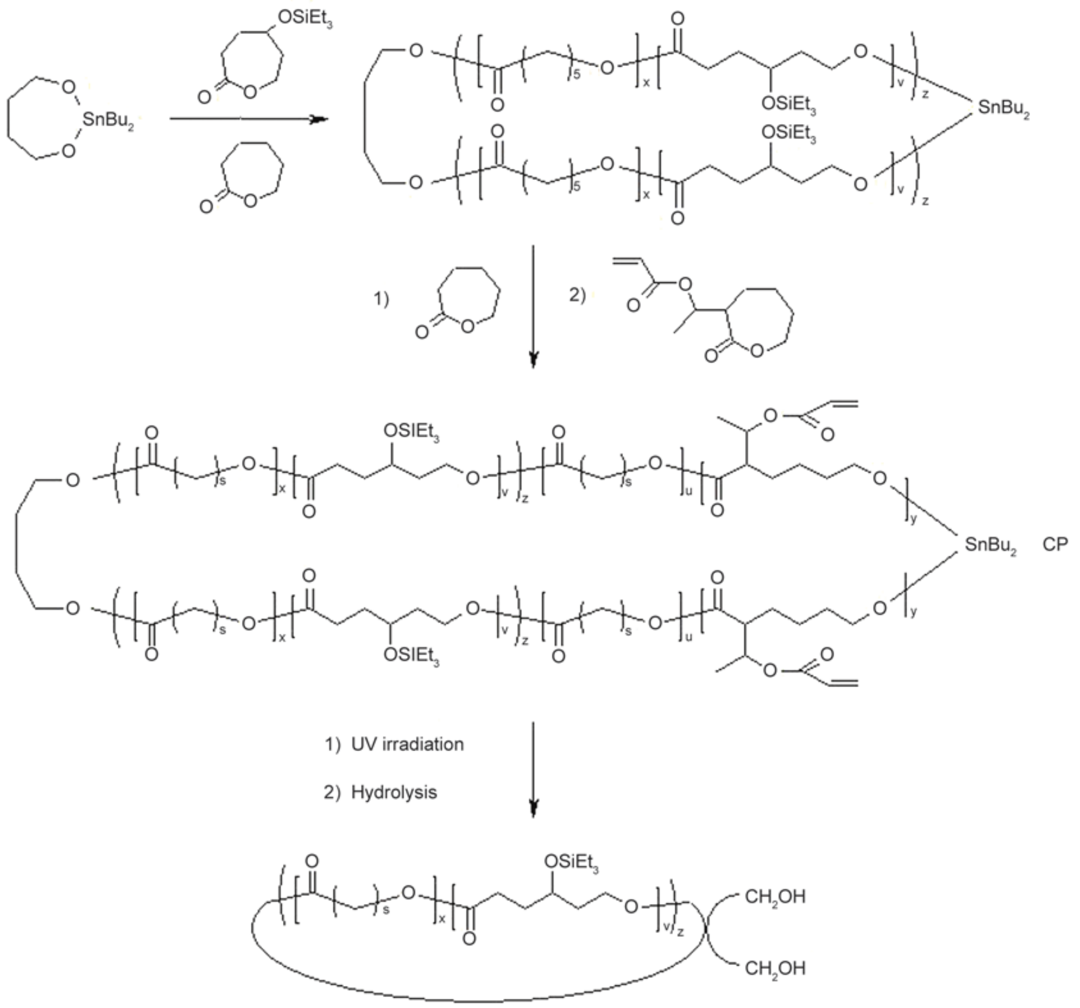

Figure 2. Synthesis of functional cyclic copolyesters

($M_{n,NMR} = 2.75\cdot10^4$ g/mol, $M_{n,SEC} = 2.55\cdot10^4$ g/mol, $M_w/M_n = 1.45$, $F_{\gamma\text{-}Et_3SiO\varepsilon CL} = 8.8\%$). Then intramolecular photo cross-linking of the unsaturations next to the propagating sites is carried out, with formation of a functionalized macrocyclic random copolyester poly(γ-Et_3SiOεCL-co-εCL) after hydrolysis of tin alkoxides.

The apparent $M_{n,SEC}$ decreased indeed from 25 500 to 21 500 upon cross-linking, consistent with the lower hydrodynamic volume that the physically more compact cyclic macromolecules exhibit with respect to the linear counterparts [1]. This observation confirms that the macrocyclic copolyester is maintained after hydrolysis of the endocyclic tin alkoxide. The polydispersity index (1.45) before and after intramolecular crosslinking, remains unchanged and the ratio of the molecular weights at the maximum of the elution peaks [$M_{p,SEC}$(cyclic)/$M_{p,SEC}$(linear)] is 0.79. An additional evidence for the successful cyclization is the ratio, g, of the intrinsic viscosity $[\eta]$ of the copolyester after and before the UV treatment. This ratio ($g = [\eta]_{cyclic}/[\eta]_{linear}$) is 0.70 in toluene at 25°C, which is again quite consistent with observations reported in the scientific literature for other macrocyclic (co)polymers [1, 30]. All these observations support that the cyclization strategy is very effective.

The thermal properties of the cyclic random copolyester and the linear counterpart were also analyzed by differential scanning calorimetry. Both the samples are semi-crystalline, which indicates that the γ-Et_3SiOεCL co-units (8.8 mol%) do not prevent PCL from crystallizing. However, the crystallinity degree, X_c, and the melting temperature, T_m, are lower for the cyclic copolyester than for the linear chains. The reverse observation is found for the glass transition temperature, T_g, which is higher for the cyclic (–56.8°C) than for the linear chains (–64.5°C). Cyclization is thus responsible for a loss of chain mobility.

3.2. Amphiphilic sun-shaped copolymers

The deprotection of the triethylsilanolate groups released hydroxyl groups that were esterified by carboxylic acid end-capped PEO, with formation of an amphiphilic sun-shaped copolymer, i.e., macrocyclic copolyesters grafted with PEO as shown in Figure 3 [32]. The SEC traces could be superposed before and after deprotection, whereas the molar composition ($DP_{\gamma\text{-HO}\varepsilon\text{CL}}$ = 17, $DP_{\varepsilon\text{CL}}$ = 178) determined by ^{1}H NMR analysis remained unchanged after deprotection. The number of the grafted PEO chains (9.5 per cyclic chain, $M_{n,NMR} = 3.55\cdot10^4$ g/mol) was estimated from the relative integration of the ^{1}H NMR signals, such that the grafting efficiency was 50–60%.

Additional although qualitative evidence for the successful grafting of PEO onto the macrocycles may be found in the formation of water-soluble micelles by self-assembly of the amphiphilic grafted macrocycles in water. Spherical micelles are observed by TEM (Figure 4), that consist of a hydrophobic core formed by the cyclic copolyester and a hydrophilic corona of PEO.

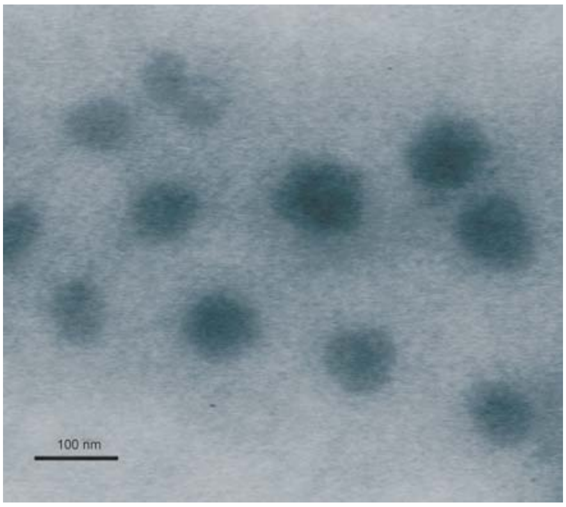

Figure 4. TEM picture of micelles of the cyclic poly(γ-HOεCL-co-εCL)-g-PEO in water

4. Synthesis of tadpole-shaped copolyesters

The novel strategy has been successfully tested for the synthesis of cyclic PCL [30] and cyclic functional copolyesters [32]. It relies on the intramolecular photo cross-linking of few acrylic unsaturations in the close vicinity of a cyclic precursor (**CP**)

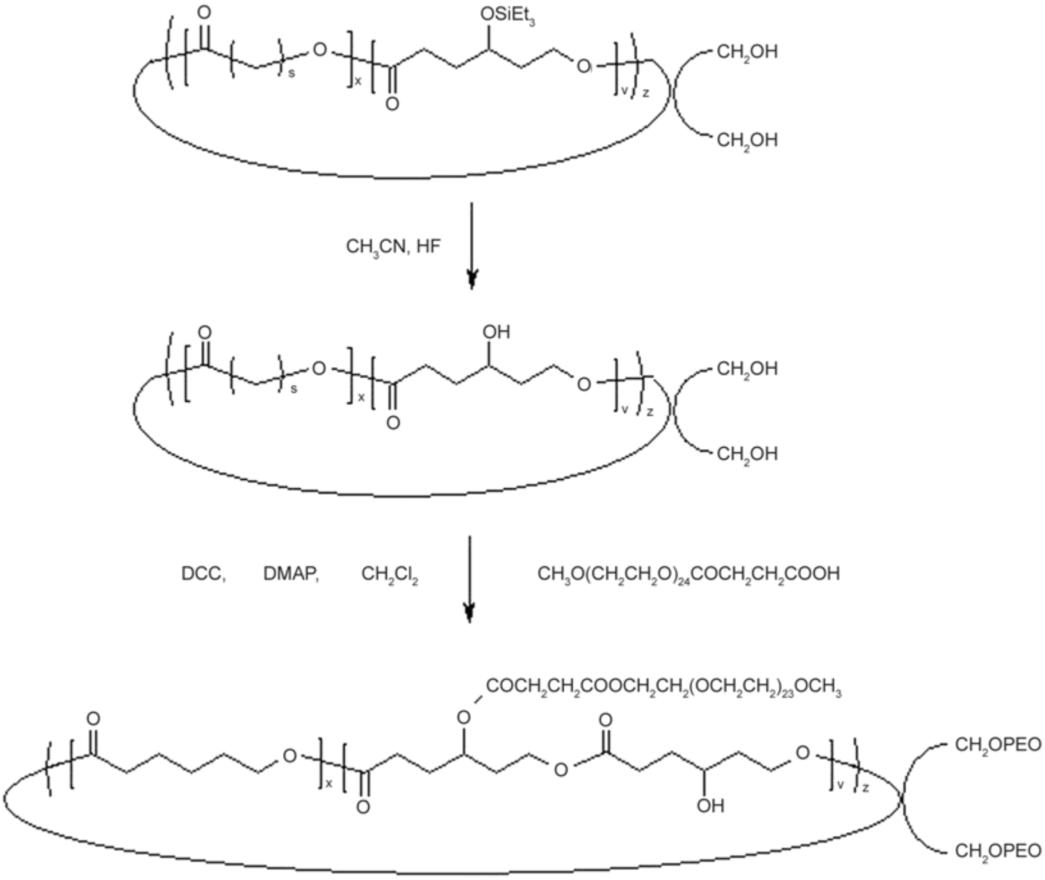

Figure 3. Synthesis of amphiphilic copolymer with a sun-shaped architecture

synthesized by ring-opening polymerization initiated by a cyclic tin alkoxide. This process is very well-suited to the synthesis of high molecular weight macrocycles. Remarkably, the propagating tin dialkoxides **1** (Figure 5) remain active after cyclization and available to further derivatization and macromolecular engineering.

As a very straightforward example [30], the εCL polymerization ($[CL]_0/[Sn]_0$ = 108, $M_{n,th}$ = 3.8 $\cdot 10^4$ g/mol) has been resumed after cyclization, so leading to tadpole-shaped chains ($M_{n,NMR}$ = $3.84\cdot 10^4$ g/mol, $M_{n,SEC}$ = $3.05\cdot 10^4$ g/mol, M_w/M_n = 1.45), thus two adjacent tails grafted onto the macrocycles ($M_{n,NMR}$ = $2.64\cdot 10^4$ g/mol, $M_{n,SEC}$ = $2.08\cdot 10^4$ g/mol, M_w/M_n = 1.45) (Figure 5, path A).

In an alternative example [33], polymerization of L-lactide can be directly initiated by the macrocyclic initiator **1** after the UV treatment (intramolecular cyclization), with formation of two PLLA chains attached to the ring in the close vicinity one to each other (Figure 5, path B). The average polymerization degree of LLA was calculated from ^{1}H NMR analysis for each tail ($DP_{L\text{-lactide}}$ = 59, $M_{n,NMR}$ = $8.5\cdot 10^3$ g/mol). The apparent molecular weight measured by SEC was actually increased ($M_{n,SEC}$ = $2.45\cdot 10^4$ g/mol, M_w/M_n = 1.40) after resumption polymerization, compared to the macrocyclic precursor ($M_{n,SEC}$ = $2.05\cdot 10^4$ g/mol, M_w/M_n = 1.40). The molecular weight calculated from the integration of the ^{1}H NMR signals was $4.45\cdot 10^4$ g/mol for the tadpole-shaped copolyesters and $2.75\cdot 10^4$ g/mol for the macrocyclic PCL. Moreover, the absence of transesterification reaction was confirmed by ^{13}C NMR spectrum. Indeed, the expanded carbonyl region shows two peaks at 173.5 ppm for cyclic PCL and at 169.5 ppm for the two PLLA tails, respectively. This observation of the PCL and PLLA homodiads without any additional signal is consistent with the coexistence of 'pure' macrocyclic PCL and linear PLLA tails. It can, thus, be concluded that the polymerization resumption is effective and that tadpole-shaped poly(ε-caprolactone) with two PLLA tails of a tunable length can be readily prepared.

The thermal behaviour of tadpole-shaped copolyester **3** (Figure 5, path B) was compared to cyclic PCL (precursor, i.e., after hydrolysis of macrocyclic initiator **1**) by differential scanning calorimetry. During cooling, crystallization peak is observed for the macrocyclic PCL at 15.0°C. When the tadpole-shaped copolyester is concerned, no crystallization is detected anymore, consistent with a much slower crystallization for the macrocyclic PCL as result of the grafting of two PLLA arms. Upon heating, a melting endotherm is clearly observed for the cyclic PCL (44°C, precursor) and a similar behavior is observed for the cyclic PCL in the tadpole-shaped copolyester. Indeed, the crystallization that did not occur during cooling, is observed during heating at –11.5°C, followed by melting at 39°C. The melting temperature of cyclic PCL is thus decreased by 5°C as result of the PLLA grafting. Although crystallization of PLLA could not be observed during the cooling and the heating steps (possibly because of a too low content of PLLA in the tadpole-shaped copolyester), a small melting endotherm was observed at a much lower temperature (132.5°C) compared to homo linear PLLA (148°C). In parallel to T_m, the crystallinity degree for cyclic PCL and PLLA is also decreased as result of incorporation into the

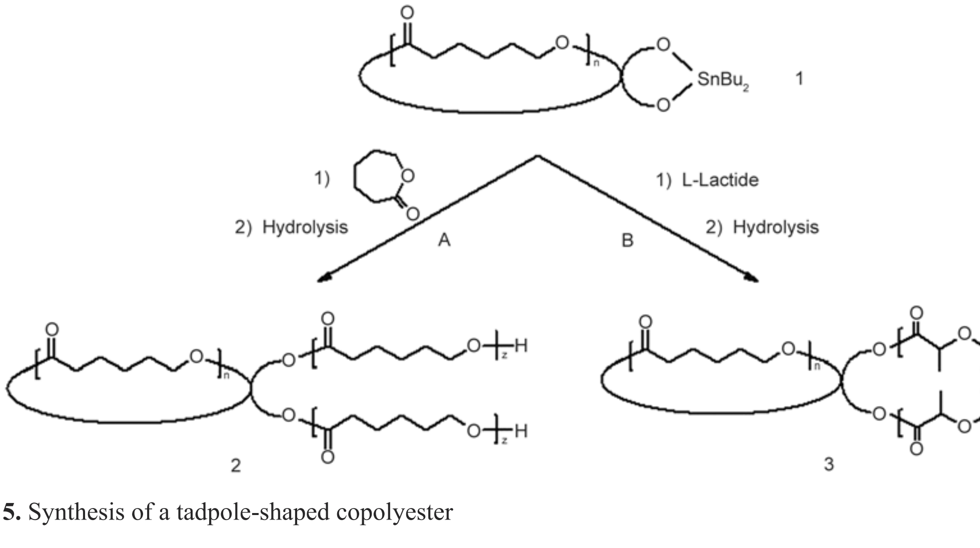

Figure 5. Synthesis of a tadpole-shaped copolyester

tadpole-shaped architecture. It thus appears that the coexistence of two crystallizable constitutive components in the copolyester has a mutually detrimental impact on their crystallization. Finally, only T_g of the cyclic PCL could be observed by DSC, which remained unaffected by grafting of PLLA.

5. Synthesis of amphiphilic tadpole-shaped copolymers

In another version, the tadpole-shaped copolyester with a high molecular weight cyclic PCL head ($M_{n,NMR} = 2.45\cdot10^4$ g/mol, $M_{n,SEC} = 2.06\cdot10^4$ g/mol, $M_w/M_n = 1.40$) and two functionalized grafted tails, has been synthesized for the very first time [34]. The active macrocyclic initiator **1** (Figure 6) after intramolecular cyclization resumes a random copolymerization of εCL and αClεCL, so yielding a tadpole-shaped copolyester ($M_{n,NMR} = 6.76\cdot10^4$ g/mol, $M_{n,SEC} = 3.0\cdot10^4$ g/mol, $M_w/M_n = 1.40$) with two activated chloride containing tails poly(αClεCL-co-εCL) ($F_{\alpha Cl\varepsilon CL} = 0.53$). The chloride groups were then converted into azides i.e., poly(αN_3εCL-co-

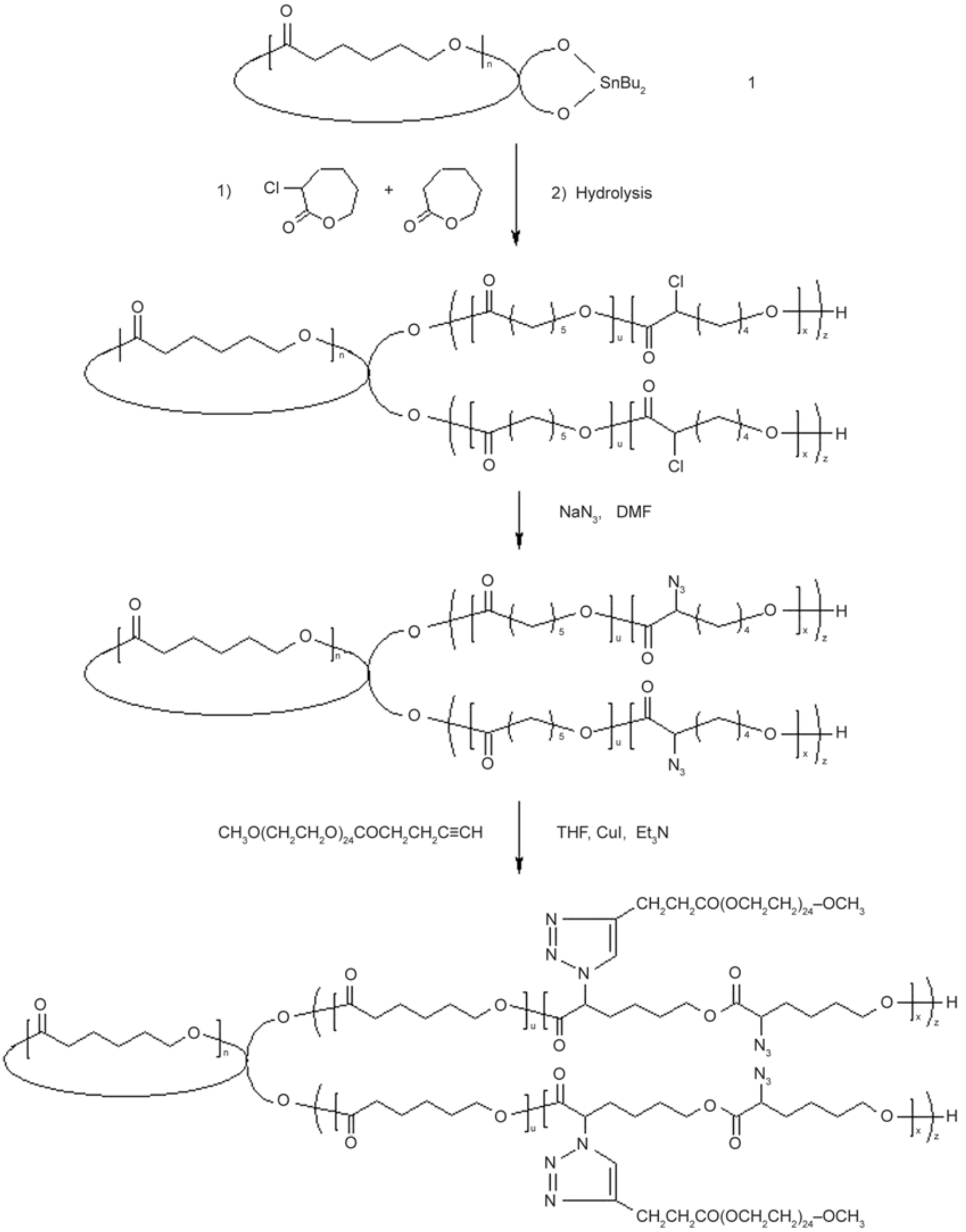

Figure 6. Synthesis of an amphiphilic copolymer by grafting of PEO onto functional tadpole-shaped copolyester

εCL) ($F_{\alpha N3\varepsilon CL}$ = 0.53), that were reacted with alkyne end-capped PEO by a 'click' copper mediated cycloaddition reaction in order to make tadpole-shaped copolyesters amphiphilic ($M_{n,NMR}$ = 1.81·10^5 g/mol, $M_{n,SEC}$ = 2.62·10^4 g/mol, M_w/M_n = 1.65). Each tail of the tadpole-shaped copolyester was grafted by 53 PEO chains and the grafting efficiency was 65% as determined by the ^{1}H NMR analysis.

The copolymerization step is controlled and the substitution (conversion of chlorides into azides) and the 'click' cycloaddition [3+2] reactions are easily implemented and quasi quantitative. The 'click' chemistry used for the grafting of the tails of the tadpole-shaped PCL is very tolerant to many functional groups and no cumbersome protection/deprotection reaction is required. It may be noted that all these copolymers consist of two biocompatible components and that PEO is known for protein repellent properties.

The thermal behavior of cyclic PCL, α-chloro-functionalized tadpole-shaped copolyester, α-azide-substituted derivative, PEO-grafted copolymer, and homo-PEO (reference) was characterized by DSC. Upon cooling, a crystallization peak was observed at 12.0°C for the macrocyclic PCL (macroinitiator **1** after hydrolysis of the tin dialkoxide), in contrast to a faint peak at a lower temperature (–12°C and –11°C) for the tadpole-shaped copolyesters with two amorphous tails poly(αClεCL-co-εCL) ($F_{\alpha Cl\varepsilon CL}$ = 0.53) and poly(αN$_3$εCL-co-εCL) ($F_{\alpha N_3\varepsilon CL}$ = 0.53), respectively. The crystallization enthalpy (ΔH_c) decreased by at least a factor of two upon the grafting of two functional tails onto the macrocyclic PCL. The same observation was also observed in case of grafting of two semi-crystalline poly(L-lactide) arms [33]. As a rule, the two tails of the tadpole-shaped copolyesters have a depressive effect on the crystallization of PCL, whatever they are amorphous or not. Crystallization of the PEO grafts of the PEO-grafted tadpole-shaped copolymer was observed although at a much lower temperature and to a lesser extent than homo PEO. During heating, a melting endotherm was noted for the cyclic PCL at 42°C with a melting enthalpy of 34.5 J/g. Once again, the negative impact of the tails was reported to an extent that depends on the substituents, thus chlorides versus azides. The melting temperature of PCL was indeed decreased by 6.5°C in case of α-chlorides and by 10.5°C for the α-azide pendant groups. In parallel to T_m, the melting enthalpy for PCL was also decreased by 7.5 J/g for the α-chloride substituted copolyester and by 10.5 J/g for the α-azide version. When PEO is part of the copolymer, only this constitutive component crystallizes, although with restrictions imposed by the complex architecture, as testified by a substantial decrease in T_m (by 17°C) and ΔH_m (by 112 J/g) compared to linear PEO.

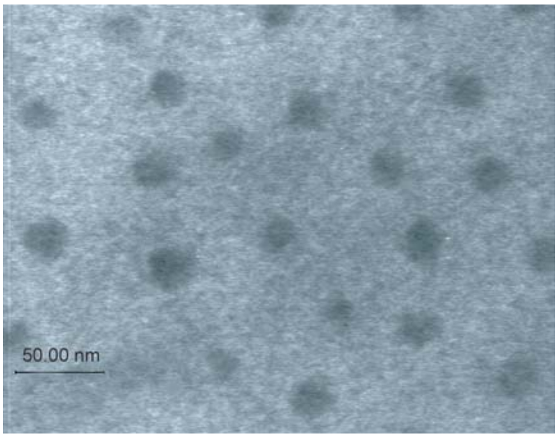

Figure 7. Micelles of PEO-grafted tadpole-shaped copolyester in water observed by TEM

The micellization in water as result of the amphiphilicity and self-assembly of this new well-defined copolymer was testified by transmission electron microscopy (Figure 7). Spherical micelles were indeed observed, that are supposed to consist of a hydrophobic polyester core surrounded by a hydrophilic corona of PEO.

6. Synthesis of eight-shaped and twin tadpole-shaped amphiphilic copolymers by using a spirocyclic tin initiator

6.1. Eight-shaped polyester

The novel strategy which allows going a step further in the complexity of the eight-shaped and twin tadpole-shaped architecture is less demanding in terms of dilution and size of the rings. Briefly, the sequential ring-opening polymerization of εCL and αAεCL units was initiated by a spirocyclic initiator (**a**, Figure 8), followed by the intramolecular photo-cross-linking of the acrylate unsaturations, thus the covalent stabilization of rather high molecular weight eight-shaped PCL **d** ($M_{n,NMR}$ = 4.12·10^4 g/mol, $M_{n,SEC}$ = 2.40·10^4 g/mol, M_w/M_n = 1.45) [35]. Before cyclization, the living chain **b** was hydrolyzed into the parent star-shaped copolyester ($M_{n,NMR}$ = 4.26·10^4 g/mol, $M_{n,SEC}$ = 2.90·10^4 g/mol, M_w/M_n =

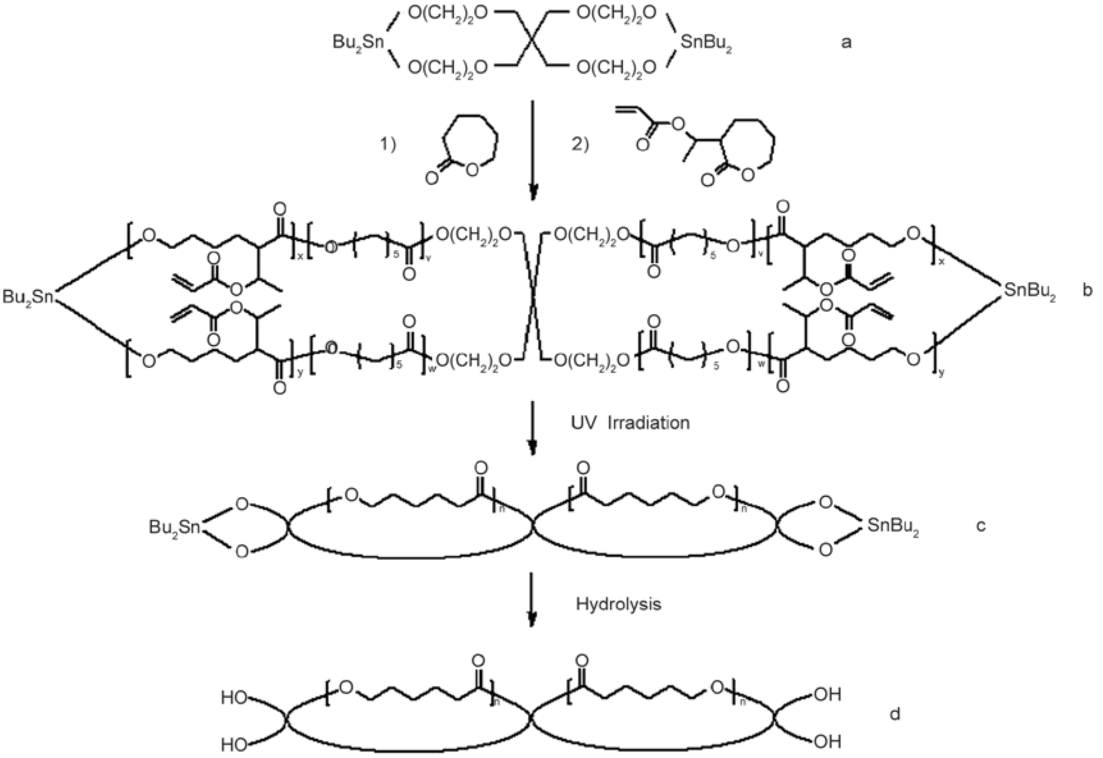

Figure 8. Synthesis of eight-shaped PCL by a spicocyclic initiator

1.45) for comparison characterization. The apparent $M_{n,SEC}$ decreased from $2.90\cdot10^4$ to $2.40\cdot10^4$ g/mol upon cross-linking, merely because of the successful conversion of star into bicyclic macromolecules. Meanwhile, the cyclization reaction did not change the molar mass distribution ($M_w/M_n = 1.45$), which is evidence for the well-controlled formation of eight-shaped macrocycles. The ratio of the molecular weights at the maximum of the elution peaks [$M_{p,SEC}$(bicyclic)/$M_{p,SEC}$(star)] was 0.65, thus smaller than the value (0.76) for monocyclic PCL ($M_{n,NMR} = 2.60\cdot10^4$ g/mol) [30].

The thermal behavior of the star-shaped (parent) and eight-shaped PCL ($M_{n,NMR} = 4.12\cdot10^4$ g/mol) was compared by DSC. The crystallinity of the eight-shaped PCL decreased from 50.0 to 22.0% upon cyclization, and the melting temperature (T_m) decreased by 17°C compared to the star-shaped PCL. In contrast, cyclization of PCL of high molecular weight had only a minor effect on T_g. The same evolution was previously observed for the impact of the cyclization of linear PCL on the thermal properties [30].

6.2. Twin tadpole-shaped amphiphilic copolymers

After UV irradiation, the bicyclic polyester without hydrolysis was nothing but a new macroinitiator **c** (Figure 9) able to resume the ring-opening polymerization of a mixture of εCL and αClεCL, so imparting a functional twin tadpole structure **e**. This was the first example of an eight-shaped architecture substituted at the same place by two dangling chains to the individual macrocycles. Indeed, the average polymerization degrees of εCL and αClεCL in the four tails of the bicyclic chains were 246 and 190, respectively, which indicates the molecular weight of the twin tadpole-shaped copolyesters was very high ($M_{n,NMR} = 1.0\cdot10^5$ g/mol). The apparent molecular weight of e measured by SEC was actually increased ($M_{n,SEC} = 3.48\cdot10^4$ g/mol) while keeping the polydispersity index unchanged ($M_w/M_n = 1.45$), compared to the spirocyclic PCL ($M_{n,SEC} = 2.40\cdot10^4$ g/mol, $M_w/M_n = 1.45$).

The pendant chloride groups of the functional twin tadpole-shaped copolyesters **e** were converted into azides under a very mild condition. The completeness of the derivatization reaction was confirmed by ^{1}H NMR and IR analysis. Moreover, the azide content of the tails in **f** ($F_{\alpha N_3\varepsilon CL} = 0.43$) was found in good agreement with the composition of the precursors **e** ($F_{\alpha Cl\varepsilon CL} = 0.43$). Meanwhile, the molecular weight and the polydispersity index before and after the derivatization remain unchanged.

Finally, the copper mediated 'click' chemistry was used to attach alkyne end-capped PEO ($M_n =$

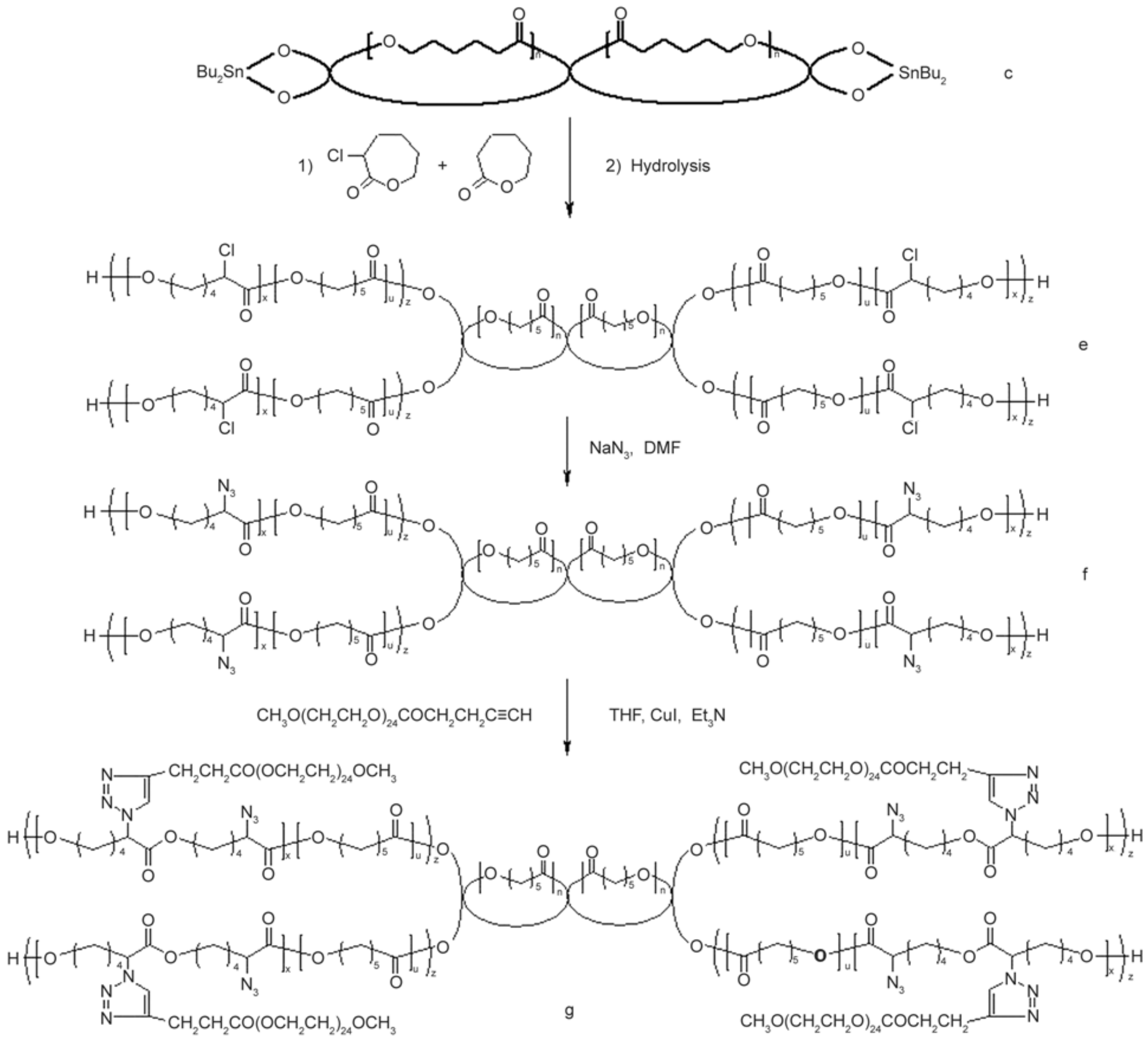

Figure 9. Synthesis of amphiphilic twin tadpole-shaped copolymers

1050 g/mol) onto those azide functionalized tails, so leading to an amphiphilic eight-shaped copolyester, whose constitutive macrocycles were grafted by four PCL-g-PEO tails. The grafting efficiency was 61% as calculated from the relative intensity of the ^{1}H NMR signals. Each tail of the copolymer **g** was grafted by 29 PEO chains and M_n was $1.95 \cdot 10^5$ g/mol as determined by ^{1}H NMR. The polydispersity of the amphiphilic twin tadpole-shaped copolymer was slightly increased (from 1.45 to 1.75) as result of the PEO-grafting in line with the chromatograms that remained monomodal and symmetrical and with the data for the PEO grafted tadpole-shaped copolymer [34].

Dependence of the crystallization on conversion of the chlorinated tails of the eight-shaped PCL (**e**) to the azide containing tails (**f**) and finally to the PEO grafted tails (**g**) was also investigated by DSC. Comparison of data shows that the crystallization temperature and enthalpy decreased by 12.5°C and 8 J/g, respectively, upon the grafting of four poly (αClεCL-co-εCL) tails onto the spirocyclic PCL. The same observation was reported when cyclic PCL was grafted by two semi-crystalline poly(L-lactide) tails [33] and by two amorphous poly (αClεCL-co-εCL) tails [34], respectively. As a rule, the grafting of mono/spiro-cyclic PCL by two/four polymeric tails, amorphous or not, has a depressive effect on the crystallization of PCL.

Conversion of the chlorinated chains into the azide containing version decreased ΔH_c by 14.5 J/g for spirocyclic PCL (**f** vs **e**). Crystallization of the PEO grafts was observed for the copolymer **g**, although at a much lower temperature (T_c decreased by 42.5°C) and to a lesser extent (ΔH_c decreased by 121.5 J/g) than homo PEO.

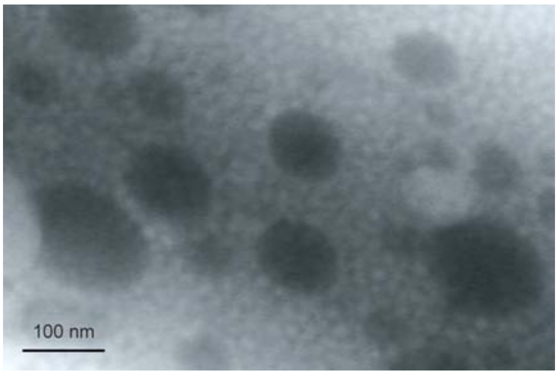

Figure 10. TEM of micelles of amphiphilic twin tadpole-shaped copolymers (Figure 9, **g**)

Comparison of T_m and ΔH_m for the spirocyclic PCL and the samples **e** and **f** confirms the negative impact of the tails on the PCL crystallization to an extent that depends on the tail substituents, thus chlorides versus azides. The melting temperature of PCL was indeed decreased by 3.5°C in case of α-chlorides and by 10.0°C for the α-azide pendant groups. In parallel to T_m, the melting enthalpy for PCL was also decreased by 5.0 J/g upon grafting of the chlorinated tails **e** and by 16.0 J/g when the tails contained azides **f** rather than chlorides. Once again, there is a clear relationship between property and macromolecular architecture. When PEO was part of the copolymer, only this constitutive component crystallized, although with some restriction imposed by the complex architecture, as testified by a substantial decrease in T_m (by 16°C) and ΔH_m (by 109.5 J/g) compared to linear PEO and in agreement with the PEO-grafting of tadpole-shaped PCL [34].

Micellization in water as result of the amphiphilicity and self-assembly of the grafted copolymer **g** was an additional although qualitative evidence for the successful grafting of PEO onto the twin tadpole-shaped macrocycles. Ellipsoidal micelles were observed by TEM (Figure 10), that are supposed to consist of a hydrophobic polyester core surrounded by a hydrophilic corona of PEO. The size of the micelles formed by the eight-shaped amphiphilic PCL/PEO copolymer **g** (Figure 9) was larger than by the monocyclic amphiphilic PCL/PEO copolymer (Figure 6) [34].

7. Conclusions

This review has highlighted the novel and efficient strategies for the synthesis of well-defined macrocyclic aliphatic polyesters, to which steadily more complex topologies can be imparted. In this respect, combination of controlled ring-opening polymerization initiated by cyclic/spirocyclic tin(IV) dialkoxides and intramolecular photo cross-linking of unsaturations close to the propagating site proved to be successful. Compared to the traditional techniques of cyclization of linear precursors by the end-to-end coupling at very high dilution, this process has the substantial advantage that linear species are never involved while cyclic precursors (**CP**) are concerned. Accordingly, the new strategy is very well-suited to the synthesis of high molecular weight macrocycles ($2.4\cdot10^4$–$4.2\cdot10^4$) under moderate dilution, which is a sizeable improvement. Very importantly, the macrocyclic/macrobicyclic polyesters prepared in these routes, can be accommodated into more complex architectures as part of a macromolecular engineering effort of the basic macrocycles/macrobicycles. Indeed, the propagating tin alkoxides remain active after cyclization and available to further derivatization, so leading to the functional tadpole-shaped and twin tadpole-shaped architectures, both the size and composition of which can be extensively tuned. In another version, when a copper mediated ‘click’ reaction was employed, new amphiphilic PEO/macrocyclic-PCL copolymers with tadpole architecture and amphiphilic PEO/macrospirocyclic-PCL copolymers with twin tadpole architecture were accordingly made available. Another engineering route was pioneered to novel functional macrocyclic copolyesters, so resulting in amphiphilic sun-shaped copolymers.

The research effort is now devoted to the synthesis of polyesters with novel architectures based on macrocyclic/macrospirocyclic building blocks. In order to shed light on the impact of the architectures on the macroscopic properties and the self-assembly both in solution and in bulk, synthesis of a wider range of macrocyclic polyesters with different compositions and different molecular weights will be explored in the future.

Acknowledgements

The authors are much grateful for the financial support to National Natural Science Foundation of China (NSFC, Grant No. 20974042), the State Ministry of Education, Scientific Research Foundation for the Returned Overseas Chinese Scholars (No. [2008]890) and to the ‘Belgian Science Policy’ (Poles Programme: PAI VI/27).

References

[1] Roovers J.: Organic cyclic polymers. in 'Cyclic polymers' (Ed.: Semlyen J. A.) 347–384 Kluwer, Dordrecht (2000).

[2] Gan Y., Dong D., Carlotti S., Hogen-Esch T. E.: Enhanced fluorescence of macrocyclic polystyrene. Journal of the American Chemical Society, **122**, 2130–2131 (2000).
DOI: 10.1021/ja9929638

[3] Laurent A., Grayson M.: Synthetic approaches for the preparation of cyclic polymers. Chemical Society Reviews, **38**, 2202–2213 (2009).
DOI: 10.1039/B809916M

[4] Yamamoto T., Tezuka Y.: Topological polymer chemistry: A cyclic approach toward novel polymer properties and functions. Polymer Chemistry, **2**, 1930–1941 (2011).
DOI: 10.1039/C1PY00088H

[5] Fiers W., Sinsheimer R. L.: The structure of the DNA of bacteriophage φX174 *: III. Ultracentrifugal evidence for a ring structure. Journal of Molecular Biology, **5**, 424–434 (1962).
DOI: 10.1016/S0022-2836(62)80031-X

[6] Bednar J., Furrer P., Stasiak A., Dubochet J., Egelmann E. H., Bates A. D.: The twist, writhe and overall shape of supercoiled DNA change during counterion-induced transition from a loosely to a tightly interwound superhelix: Possible implications for DNA structure *in vivo*. Journal of Molecular Biology, **235**, 825–847 (1994).
DOI: 10.1006/jmbi.1994.1042

[7] Hild G., Kohler A., Rempp P.: Synthesis of ring-shaped macromolecules. European Polymer Journal, **16**, 525–527 (1980).
DOI: 10.1016/0014-3057(80)90136-6

[8] Roovers J., Toprowski P. M.: Synthesis of high molecular weight ring polystyrenes. Macromolecules, **16**, 843–849 (1983).
DOI: 10.1021/ma00240a002

[9] Geiser D., Höcker H.: Preparation of macrocyclic polystyrene. Polymer Bulletin, **2**, 591–597 (1980).
DOI: 10.1007/BF00263029

[10] El Madani A., Favier J-C., Hémery P., Sigwalt P.: Synthesis of ring-shaped polyisoprene. Polymer International, **27**, 353–357 (1992).
DOI: 10.1002/pi.4990270411

[11] Rique-Lurbet L., Schappacher M., Deffieux A.: A new strategy for the synthesis of cyclic polystyrenes: Principle and application. Macromolecules, **27**, 6318–6324 (1994).
DOI: 10.1021/ma00100a014

[12] Schappacher M., Deffieux A.: Synthesis of macrocyclic copolymer brushes and their self-assembly into supramolecular tubes. Science, **319**, 1512–1515 (2008).
DOI: 10.1126/science.1153848

[13] Schappacher M., Deffieux A.: Imaging of catenated, figure-of-eight, and trefoil knot polymer rings. Angewandte Chemie International Edition, **48**, 5930–5933 (2009).
DOI: 10.1002/anie.200900704

[14] Tezuka Y., Komiya R.: Metathesis polymer cyclization with telechelic poly(THF) having allyl groups. Macromolecules, **35**, 8667–8669 (2002).
DOI: 10.1021/ma021023w

[15] Xie M., Shi J., Ding L., Li J., Han H., Zhang Y.: Cyclic poly(ε-caprolactone) synthesized by combination of ring-opening polymerization with ring-closing metathesis, ring closing enyne metathesis, or 'click' reaction. Journal of Polymer Science Part A: Polymer Chemistry, 47, 3022-3033 (2009).
DOI: 10.1002/pola.23390

[16] Chen L., Xu B., Li M., Li H.: Synthesis of cyclic poly (ε-caprolactone) by high efficient ring-closing metathesis reaction (in Chinese). Acta Polymerica Sinica, **7**, 743–748 (2012).
DOI: 10.3724/SP.J.1105.2012.11355

[17] Kubo M., Hayashi T., Kobayashi H., Tsuboi K., Itoh T.: Synthesis of α-carboxyl, ω-amino heterodifunctional polystyrene and its intramolecular cyclization. Macromolecules, **30**, 2805–2807 (1997).
DOI: 10.1021/ma961850v

[18] Laurent B. A., Grayson S. M.: An efficient route to well-defined macrocyclic polymers via 'click' cyclization. Journal of the American Chemical Society, **128**, 4238–4239 (2006).
DOI: 10.1021/ja0585836

[19] Shi G. Y., Pan C. Y.: Synthesis of well-defined figure-of-eight-shaped polymers by a combination of atrp and click chemistry. Macromolecular Rapid Communications, **29**, 1672–1678 (2008).
DOI: 10.1002/marc.200800337

[20] Shi G. Y., Pan C. Y.: An efficient synthetic route to well-defined theta-shaped copolymers. Journal of Polymer Science Part A: Polymer Chemistry, **47**, 2620–2630 (2009).
DOI: 10.1002/pola.23347

[21] Dong Y. Q., Tong Y. Y., Dong B. T., Du F. S., Li Z. C.: Preparation of tadpole-shaped amphiphilic cyclic PS-*b*-linear PEO via atrp and click chemistry. Macromolecules, **42**, 2940–2948 (2009).
DOI: 10.1021/ma802361h

[22] Sugai N., Heguri H., Ohta K., Meng Q., Yamamoto T., Tezuka Y.: Effective click construction of *bridged*- and *spiro*-multicyclic polymer topologies with tailored cyclic prepolymers (*kyklo*-telechelics). Journal of the American Chemical Society, **132**, 14790–14802 (2010).
DOI: 10.1021/ja103402c

[23] Oike H., Imaizumi H., Mouri T., Yoshioka Y., Uchibori A., Tezuka Y.: Designing unusual polymer topologies by electrostatic self-assembly and covalent fixation. Journal of the American Chemical Society, **122**, 9592–9599 (2000).
DOI: 10.1021/ja001736z

[24] Tezuka Y.: Topological polymer chemistry by electrostatic self-assembly. Journal of Polymer Science Part A: Polymer Chemistry, **41**, 2905–2917 (2003).
DOI: 10.1002/pola.10893

[25] Bielawski Ch. W., Benitez D., Grubbs R. H.: An 'endless' route to cyclic polymers. Science, **297**, 2041–2044 (2002).
DOI: 10.1126/science.1075401

[26] He T., Zheng G-H., Pan C-Y.: Synthesis of cyclic polymers and block copolymers by monomer insertion into cyclic initiator by a radical mechanism. Macromolecules, **36**, 5960–2966 (2003).
DOI: 10.1021/ma021371y

[27] Kricheldorf H. R.: Biodegradable polymers with variable architectures via ring-expansion polymerization. Journal of Polymer Science Part A: Polymer Chemistry, **42**, 4723–4742 (2004).
DOI: 10.1002/pola.20261

[28] Kricheldorf H. R., Lee S-R., Schittenhelm N.: Macrocycles, 1. Macrocyclic polymerizations of (thio)lactones – stepwise ring expansion and ring contraction. Macromolecular Chemistry and Physics, **199**, 273–282 (1998).
DOI: 10.1002/(SICI)1521-3935(19980201)199:2<273::AID-MACP273>3.0.CO;2-D

[29] Culkin D. A., Jeong W., Csihony S., Gomez E. D., Balsara N. P., Hedrick J. L., Waymouth R. M.: Zwitterionic polymerization of lactide to cyclic poly(lactide) by using n-heterocyclic carbene organocatalysts. Angewandte Chemie International Edition, **46**, 2627–2630 (2007).
DOI: 10.1002/anie.200604740

[30] Li H., Debuigne A., Jérome R., Lecomte P.: Synthesis of macrocyclic poly(ε-caprolactone) by intramolecular cross-linking of unsaturated end groups of chains precyclic by the initiation. Angewandte Chemie International Edition, **45**, 2264–2267 (2006).
DOI: 10.1002/anie.200503961

[31] Hadziioannou G., Cotts P. M., ten Brinke G., Han C. C., Lutz P., Strazielle C., Rempp P., Kovacs A.: Thermodynamic and hydrodynamic properties of dilute solutions of cyclic and linear polystyrenes. Macromolecules, **20**, 493–497 (1987).
DOI: 10.1021/ma00169a006

[32] Li H., Jérôme R., Lecomte P.: Amphiphilic sun-shaped polymers by grafting macrocyclic copolyesters with PEO. Macromolecules, **41**, 650–654 (2008).
DOI: 10.1021/ma070282o

[33] Li H., Jérôme R., Lecomte P.: Synthesis of tadpole-shaped copolyesters based on living macrocyclic poly (ε-caprolactone). Polymer, **47**, 8406–4813 (2006).
DOI: 10.1016/j.polymer.2006.10.008

[34] Li H., Riva R. Jérôme R., Lecomte P.: Combination of ring-opening polymerization and 'click' chemistry for the synthesis of an amphiphilic tadpole-shaped poly(ε-caprolactone) grafted by PEO. Macromolecules, **40**, 824–831 (2007).
DOI: 10.1021/ma062488f

[35] Li H., Riva R., Kricheldorf H. R., Jérôme R., Lecomte P.: Synthesis of eight- and star-shaped poly(ε-caprolactone)s and their amphiphilic derivatives. Chemistry A: European Journal, **14**, 358–368 (2008).
DOI: 10.1002/chem.200700603

eXPRESS Polymer Letters Vol.7, No.8 (2013) 703–715
Available online at www.expresspolymlett.com
DOI: 10.3144/expresspolymlett.2013.67

Accelerated weathering of PP based nanocomposites: Effect of the presence of maleic anhydryde grafted polypropylene

M. Morreale[1], *N. Tz. Dintcheva*[2*], *F. P. La Mantia*[2]

[1]Università degli Studi di Enna „Kore", Facoltà di Ingegneria, Architettura e delle Scienze Motorie, Cittadella Universitaria, 94100 Enna, Italy
[2]Dipartimento di Ingegneria Civile, Ambientale, Aerospaziale, dei Materiali, Università di Palermo, Viale delle Scienze, Ed. 6, 90128 Palermo, Italy

Received 8 March 2013; accepted in revised form 9 May 2013

Abstract. Polymer nanocomposites are currently a topic of great interest. The increasing importance they are gaining also in the standpoint of industrial applications, is giving concerns regarding their environmental stability and, in general, their behaviour in outdoor applications, under direct solar irradiation. Papers available in the literature have highlighted the different influences of different nanosized fillers, in particular clay-based nanofillers; however, few data are available regarding other nanosized fillers. Furthermore, the research on polymer nanocomposites has clearly pointed out that the use of compatibilizers is required to improve the mechanical performance and the dispersion of polar fillers inside apolar polymer matrices, especially when complex mechanisms such as intercalation and exfoliation, typical of clay-filled nanocomposites, are involved. In this work, the photo-oxidation behaviour of polypropylene/clay and polypropylene/calcium carbonate nanocomposites containing different amounts of maleic anhydride grafted polypropylene (PPgMA) and subjected to accelerated weathering, was investigated. The results showed significant differences between the two nanofillers and different degradation behaviours in presence of the compatibilizer. In particular, PPgMA modified the dispersion of the nanofillers but, on the other hand, higher amounts proved to lead to the formation of some heterogeneities. Furthermore, PPgMA proved to positively affect the photo-oxidation behaviour by decreasing the rate of formation of the degradation products.

Keywords: *nanocomposites, weathering stability, morphology, mechanical properties, FT-IR spectroscopy*

1. Introduction

The use of nanometric-scale sized fillers for the preparation of thermoplastic polymer composites is of topical interest in the academia, because of the significant improvements achievable in terms of technological properties, such as the elastic modulus, the tensile strength, the barrier properties, the flexural modulus [1–8]. These enhancements are promising and attracting also the interest from industrial world, in sight of several applications which could benefit from them. On the other hand, it is known [3] that polymer based nanocomposites have been struggling to conquer mainstream volume market shares, and this can be attributed to some weaknesses. One of these is represented by their environmental stability, especially when outdoor applications (i.e. furnishing, building, packaging, automotive) are concerned.

It is known from the literature that polymer/silicate nanocomposites can show significant effects due to photo-oxidation (in particular, higher photo-oxidation rates and thus reduction of the mechanical prop-

---

[*]Corresponding author, e-mail: nadka.dintcheva@unipa.it

erties, in comparison to the pristine polymer matrix). These phenomena have been reported for several kinds of polymer used and were mainly attributed to a reduction of the photo-oxidation induction time [9–17]. This, in turn, was attributed to several factors, such as the presence of iron ions catalyzing the photo-oxidation process [9, 10], the formation of catalytic acidic sites or radicals following the decomposition of the organo-modifier (involving both the alkyl chain and the ammonium ions) [10–12, 17].

As regards the nanocomposites containing nanosized calcium carbonate, it was found [18] that the photo-oxidation rate increases in comparison to the pristine polymer matrix, and it was proposed that this might be attributed to several causes (nucleation phenomena, catalytic effects, presence of impurities or light sensitizers). Morreale *et al.* [19] performed a direct comparison between the photo-oxidation behaviours of silicate-filled and calcium carbonate-filled nanocomposites, finding that both organo-modified clay and nanometric calcium carbonate can increase the photo-oxidation rates; in particular, they showed how the nucleation phenomena, and thus the morphological and structural changes, can account for the photo-oxidation behaviour of calcium carbonate nanocomposites, and also that the distribution of photo-oxidation products in these nanocomposites is significantly different from that typically findable in those filled with organomodified clay.

Literature reports also about the photo-oxidation behaviour of clay-filled nanocomposites in presence of compatibilizers such as maleated polyolefins. Qin *et al.* [12] reported that maleic anhydride grafted polypropylene does not significantly modify the rate of photo-oxidation; Mailhot *et al.* [13] found that this compatibilizer can actually introduce some photo-responsive groups, leading to an acceleration of the photo-oxidation of polypropylene when used in combination with organophilic montmorillonite. However, to our present knowledge, there are few or no data regarding the photooxidation behaviour of polyolefin/calcium carbonate nanocomposites when a maleated polyolefin is added.

In this work, therefore, we investigated the behaviour of polypropylene (PP)/calcium carbonate nanocomposites in presence of different amounts of polypropylene grafted with maleic anhydride, and compared it with that of PP/organomodified montmorillonite nanocomposites.

2. Experimental

2.1. Materials

The PP used in this work was a Moplen X30G grade produced by Basell (Italy); the main properties according to the Producer are: density = 0.9 g·cm^{-3}, melt index ≈ 8 g·(10 min)$^{-1}$ (at 230°C and 21.6 N) and melting temperature $T_m \approx 170$°C. It is also known from the literature [20] that this general purpose PP usually contains small amounts of phenolic primary antioxidants and phosphite secondary antioxidants. However, it is known from the Literature that they are able to protect against thermal-oxidation during the processing [9, 11, 14, 17], but they have only an indirect influence on the photo-oxidation behaviour (for instance, by interfering with the formation of double bonds), which could be seen only as far as the final conditions are concerned, while the mechanisms and paths are not altered; furthermore, all of the systems prepared and investigated here contain practically the same amount of antioxidants, therefore their presence does not influence the comparisons. The nanosized fillers were a precipitated calcium carbonate, supplied by Solvay (Belgium) under the commercial name of Socal® 31 (in the following indicated as S31), with a calcite rhombohedral crystal structure, cube-like crystal shape and a mean particle diameter 50–100 nm [21], and a montmorillonite clay produced by Southern Clay Products (USA) and commercialized as Cloisite® 15A (further indicated as CL15A; modified with dimethyl-dihydrogenated tallow–quaternary ammonium chloride quaternary surfactant; quaternary concentration = 12 meq·(100 g)$^{-1}$ clay; d_{001} = 3.15 nm; density = 1.66 g·cm^{-3}).

The coupling agent was a polypropylene grafted with maleic anhydride (PPgMA), supplied by Sigma Aldrich (USA), with maleic anhydride content 8–10 wt% and melting temperature = 156°C.

The nanocomposite systems were prepared by always using a 5 wt% amount of the filler (clay or calcium carbonate), while the PP/PPgMA ratio changed from 100/0, 95/5, 85/15 to 75/25.

2.2. Processing

The neat PP, the binary PP/PPgMA blend and the nanocomposites were prepared in a co-rotating intermeshing twin-screw extruder (OMC, Italy), having L/D = 35, D = 19 mm. The adopted temperature profile was 120–130–140–150–160–170–190°C (die), with screw speed set at 200 rpm and the speed of the gravimetric feeder set at 10 rpm. The extrudates were water cooled and granulated by means of an Accrapak (UK) rotating blade system. Specimens for mechanical, calorimetric, morphological and Fourier transform infrared (FTIR) spectral characterization were prepared by compression moulding, using a Carver (USA) laboratory press set at 190°C (15 cm × 15 cm electrically heated and water cooled plates, pressure about 20 MPa, compression time 3–4 min).

2.3. Accelerated weathering

The compression moulded sheets were subjected to accelerated weathering conditions in a Q-UV (Q-Lab Corp., USA) apparatus, containing eight UVB-313 lamps. The exposure cycle conditions were 8 h of light at a temperature of 55°C followed by 4 h condensation at 35°C.

2.4. Mechanical characterization

Tensile properties (elastic modulus, tensile strength and elongation at break) were determined according to ASTM D882, with the help of an Instron mod. 3365 (USA) apparatus. The specimens were cut from the compression-moulded sheets and tested at 5 mm/min crosshead speed. At least seven samples were tested for each tensile property and the average values (with the corresponding error bars) are reported. In the case of photo-oxidized samples, at least five samples were tested and the reproducibility was about ±6%.

2.5. Differential scanning calorimetry

Calorimetric data were obtained using a Perkin-Elmer DSC7 apparatus, at scanning rate of 10°C·min^{-1} in the temperature range from 30 to 210°C. At least three samples for each formulation were tested and the reproducibility of the collected data was satisfactory (±4%).

2.6. FTIR analysis

A Fourier Transform Infrared (FTIR) spectrometer (Spectrum One, Perkin-Elmer, UK) was used to record FTIR spectra of the samples, performing 16 scans at a resolution of 1 cm^{-1} (in the range 450–4000 cm^{-1}). The relative concentration of functional groups was determined from their peak absorption area index (absorbance peak area of the chemical group compared to that of the reference absorption peak area located at 2722 cm^{-1} and being known as the sum of the $\delta(CH_2)$ and $\gamma_t(CH_2)$ vibrations [22]). Measurements were obtained from the average of three samples, with a calculated reproducibility of ±3%.

2.7. Morphological characterization by SEM

The scanning electron microscopic (SEM) analysis was performed by scanning of the nitrogen fractured surfaces of the specimens, using a FEI (USA) Quanta F200 equipment.

2.8. X-ray analysis

Wide angle X-ray diffraction (WAXD) patterns were obtained at room temperature by using a Siemens (Germany) D-500 X-ray diffractometer in the reflection mode with Cu K_α incident radiation of wavelength 0.1542 nm.

The interlayer distance was calculated using Bragg's formula (Equation (1)):

$$d_{001} = \frac{n\lambda}{2\sin\theta} \tag{1}$$

From the results, it was possible to calculate the number of clay platelets per average stack with the interlayer distance d_{001} using Equation (2):

$$N = 1 + \frac{t}{d_{001}} \tag{2}$$

where t is given by the Scherrer's formula, $t = 0.9\lambda/(B_{1/2}\cdot\cos\theta_b)$, λ is the wavelength, $B_{1/2} = \theta_1 - \theta_2$ (in radiants) at half peak height ($I_{max/2}$), $\theta_b = (\theta_1 + \theta_2)/2$ [23].

2.9. TEM analysis

Tansmission electron microscopic (TEM) observations were made with a ZEISS (Germany) EM 900 microscope, at accelerating voltages of 50 and 80 KeV, in the Genoa division of the Institute for Macromolecular Studies (ISMac) of CNR (Italian National Research Council). The dimension of the microtomed sample was about 10 μm.

3. Results and discussion

Figure 1a–1c report respectively the tensile modulus, tensile strength and elongation at break for the investigated systems (unfilled polymer, composite with modified clay and composite with nanosized calcium carbonate) as a function of the PP-PPgMA ratio (from 100/0 to 75/25, as described in the experimental part).

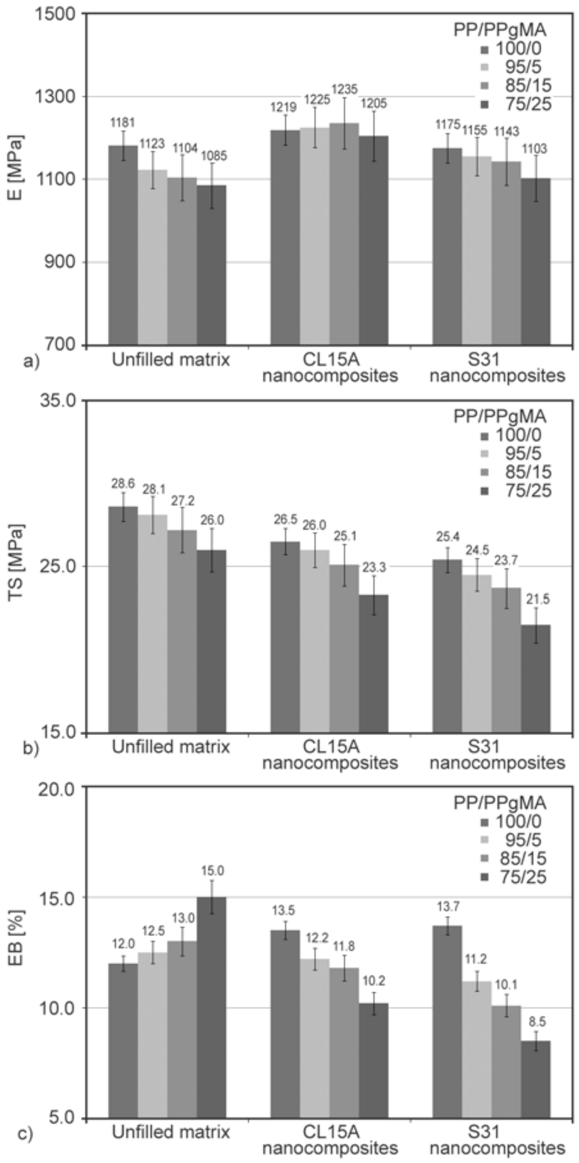

Figure 1. Main mechanical properties: (a) elastic modulus, *E*, (b) tensile strength, *TS*, (c) elongation at break, *EB*, of the unfilled matrix, CL15A nanocomposites and S31 nanocomposites with different PP/PPgMA ratios

As regards the elastic modulus, the addition of PPgMA leads to a significant reduction of the rigidity of the material (higher upon increasing the MA content), in agreement with previous results on similar systems [17]. The behavior is completely different as far as the nanocomposites are concerned: the elastic modulus keeps practically unchanged, and some reductions (however, not higher than 5%) are experienced only in the S31-filled nanocomposite at higher PPgMA content. On the average, the nanocomposites keep higher moduli than the corresponding unfilled systems, and the CL15A filled ones show the highest overall values. Indeed, the overall results can be explained by taking into account two different factors: the presence of PPgMA and the effect of the filler. When PPgMA is added to the PP at sufficiently high amounts, the polymer matrix actually becomes a polymer blend. In polymer blends, the properties typically vary according to the values of the properties of the pure components, as well as their relative amounts [24]. Significant deviations from this behavior can be present mainly when synergistic or strong incompatibility issues occur [24, 25]. In the case of this study, PPgMA has lower elastic modulus (not reported here for sake of conciseness) than that of pure PP, therefore the blends have decreasing modulus (Figure 1a) upon increasing the PPgMA content. The same explanation holds for the tensile strength (Figure 1b) and the elongation at break (Figure 1c): in this last case, the value increases due to the higher ductility of PPgMA. However, as far as the nanocomposites are concerned, there is one more factor to be taken into account, i.e. the presence of the filler and the role of its interface with the matrix. In fact, the presence of PPgMA can improve the adhesion between the matrix and the filler, and this effect counterbalances the lower rigidity given by PPgMA. In summary, the mechanical properties trends of the nanocomposites can be explained by taking into account both the two factors, which can be in contrast and lead to opposite directions according to which of the two prevails.

With particular concern to the tensile strength, the presence of CL15A and S31 leads to small reductions of the resistance, in agreement with our previous results [19]. In general, it can be stated that both the breaking properties (tensile strength and elongation at break) are ruled by the heterogeneity of the system [24], which obviously increases upon increasing the amount of PPgMA and reaches a maximum at the 75/25 PP-to-PPgMA ratio. This helps to explain the nanocomposites behavior observable in Figure 1b and 1c, i.e. the reduction of tensile strength and elongation at break upon increasing the PPgMA content, and will be further discussed with reference to morphological analysis, below reported.

Figure 2a, 2b, show respectively the enthalpies of melting and crystallization for the investigated systems, obtained by DSC analysis. Both the melting and the crystallization enthalpy tend to decrease upon increasing the PPgMA content; it can be, on the whole, stated that the calorimetric data are in per-

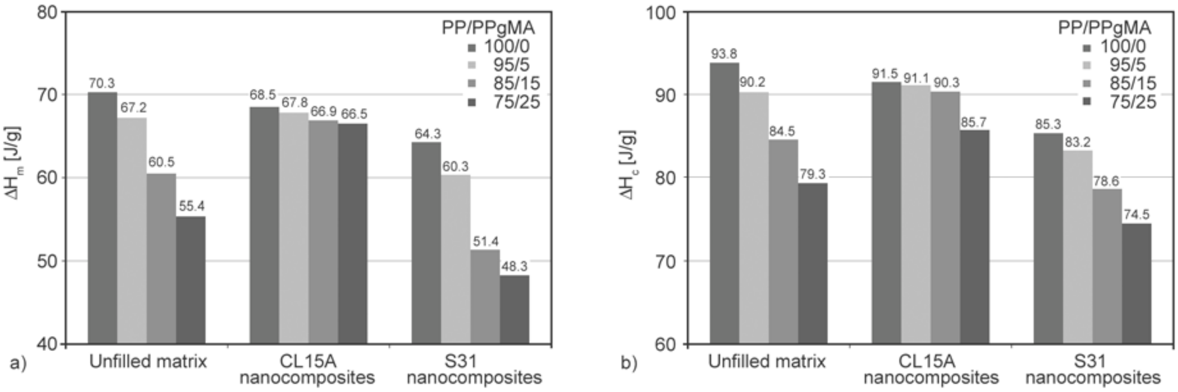

Figure 2. Enthalpies of (a) melting and (b) crystallization of the unfilled matrix, CL15A nanocomposites and S31 nanocomposites with different PP/PPgMA ratios

fect agreement with the values of the elastic modulus: the reduced crystallinity upon increasing the PPgMA content thus accounts for the reduction in the elastic modulus, which is counterbalanced, in the nanocomposites, by the presence of the filler and the compatibilizer.

Figure 3 reports the morphology of some representative samples, obtained by SEM and TEM analysis, as well as our graphic interpretation of the morphology. It can be observed that the SEM morphology of the fracture surface of the polymer (i.e. without filler) appears, in general, slightly more homogeneous upon adding PPgMA (see Figure 3a), while no significant differences are detectable between the SEM morphologies of CL15A nanocomposites without and with 75/25 PP/PPgMA ratio (Figure 3b). Important information is, on the other hand, obtainable from the TEM images reported in the same figure: the filler dispersion upon adding PPgMA is significantly improved. However, as previously mentioned with regard to the mechanical properties, although PP and PPgMA are physically miscible (thus forming a polymer blend without observable phase separation, as shown by the SEM images), they are not chemically compatible [26, 27]; therefore, higher PPgMA contents (as in the case of 75/25 systems) are likely to form heterogeneous micro-zones as schematically shown in the drawings in Figure 3b, where a graphical interpretation of the system structure at nanometric scale is provided for CL15A nanocomposite (left) and CL15A nanocomposite with 75/25 PP/PPgMA ratio (right). The presence of PPgMA increases clay dispersion (with partial exfoliation, as further proved by XRD analysis which will be described in the following) and should therefore improve the mechanical properties, but its high amount and its chemical incompatibility leads to the formation of heterogeneities (grey in the drawings) consisting in PPgMA with some clay particles at the inside. The considerations about selective disposition of the clay platelets and stakes, especially into the more polar phase, within the incompatible polymer blends, have been also made on the base of our previous studies [28, 29]. This can also help in explaining the reduction of the tensile strength and the elongation at break upon increasing the PPgMA content, as already pointed out in the discussion about the mechanical properties (Figures 1b and 1c), in spite of the improved filler dispersion. As regards the S31 nanocomposites with and without PPgMA, SEM images as well as our graphical interpretations of the inner morphology at nanometric scale are provided in Figure 3c. The presence of PPgMA helps in improving the dispersion but, on the other hand, similar phenomena as in the case of CL15A nanocomposites can occur (grey zones). It was mentioned above that further information in the direction of clay behaviour in terms of dispersion and morphology was provided by XRD analysis; the results are reported in Table 1. The interlayer distance of the clay increases in the nanocomposite without PPgMA, showing that some intercalation occurs and confirming the result suggested by the TEM image (predominantly intercalated morphology). When PPgMA is added, the interlayer distance increases upon increasing the PPgMA content, to such a level that, when a 75/25 PP-to-PPgMA ratio is adopted, the results coming from XRD and TEM analyses prove that a mixed intercalated/exfoliated (predominantly exfoliated) morphology is achieved.

Figure 4a and 4b report, respectively, the dimensionless elastic modulus (*E* at time ‘*t*’ vs *E* at time

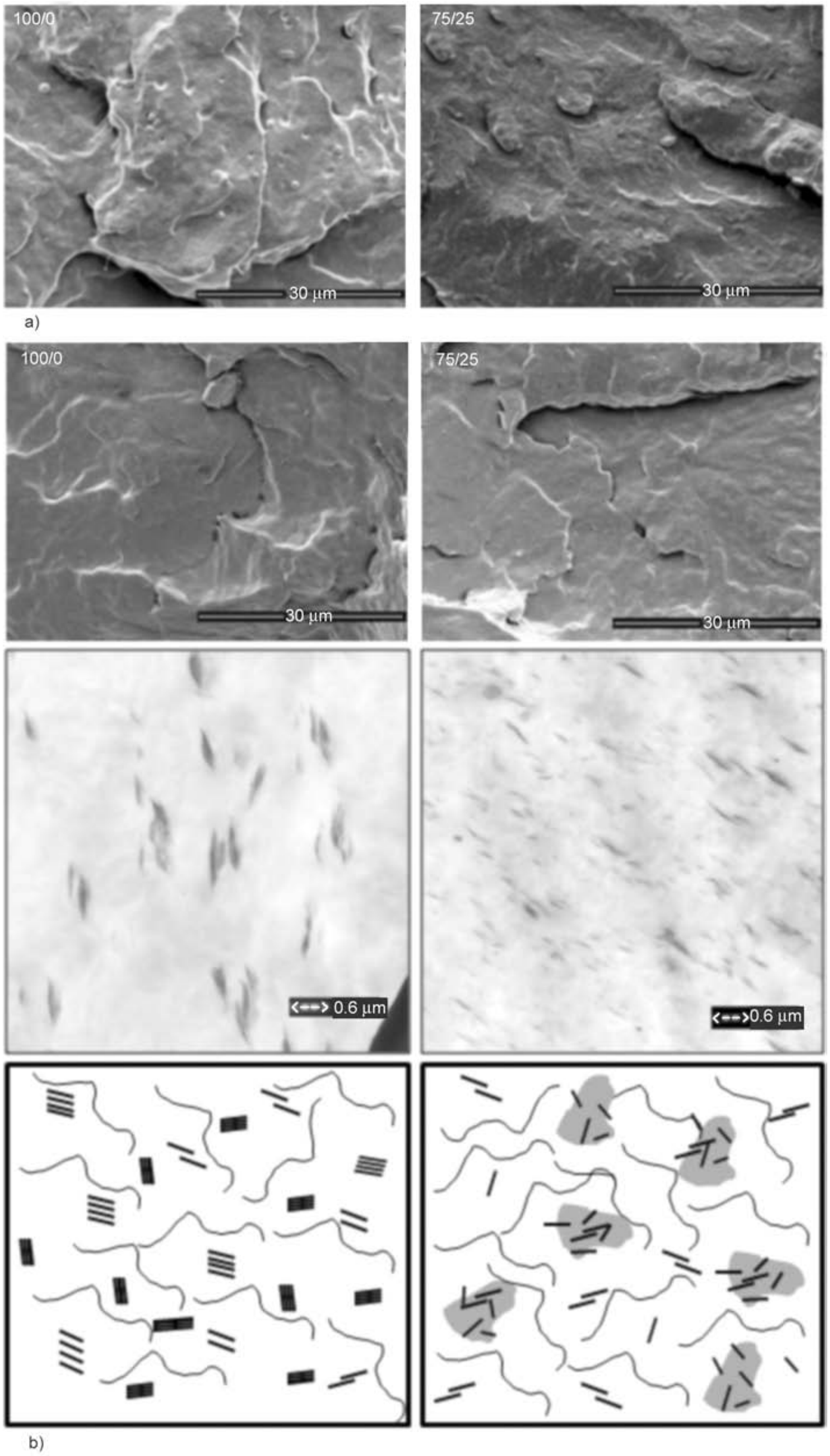

Figure 3a, b. SEM, TEM images and graphic interpretation of some investigated samples: (a) PP/PPgMA = 100/0 and 75/25, (b) CL15A nanocomposite where PP/PPgMA = 100/0 and 75/25

zero) of the samples containing clay (a) or calcium carbonate (b), upon increasing the photo-oxidation time; the figures contain also the data of the PP-PPgMA blends. The reported data clearly outline that an increase of the elastic modulus occurs upon increasing the accelerated weathering time, in agreement with our previous results and other studies on similar systems [9, 19]. The presence of the nano-

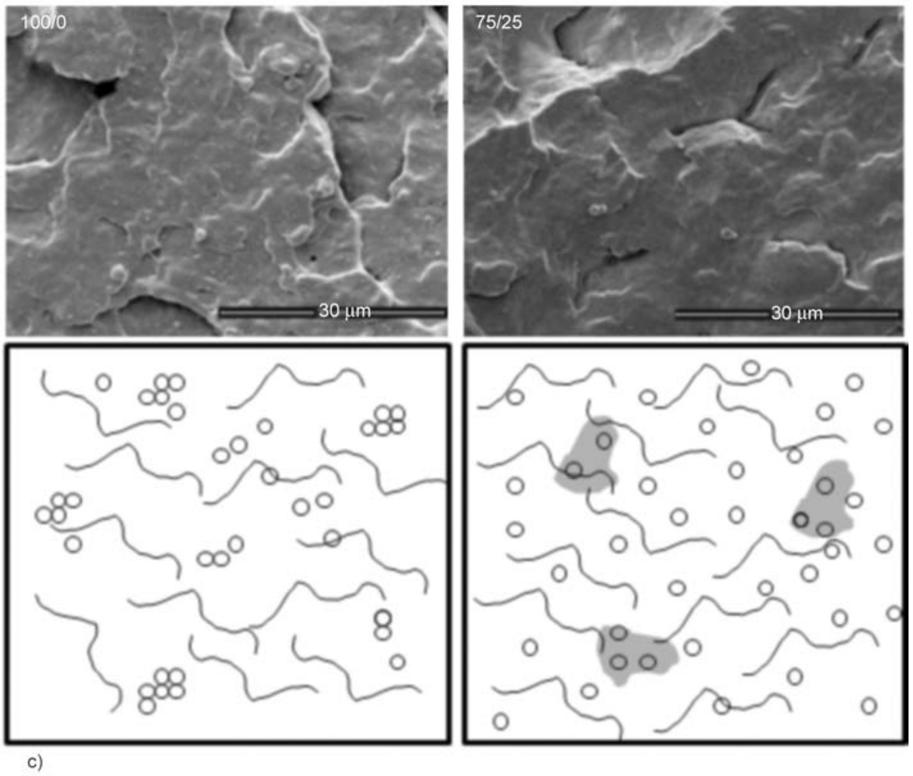

Figure 3c. SEM, TEM images and graphic interpretation of some investigated samples: (c) S31 nanocomposite where PP/PPgMA = 100/0 and 75/25

Table 1. Main XRD peaks and interlayer distances for pristine clay and nanocomposite systems

Sample	Main peak 2θ [°]	Interlayer distance d_{001} [nm]	Platelets/stack [N]
CL15A	2.80	3.15	3.11
PP/PPgMA/CL15A = 100/0/5	2.67	3.30	2.61
PP/PPgMA/CL15A = 95/5/5	2.58	3.42	2.33
PP/PPgMA/CL15A = 85/15/5	2.32	3.81	2.08
PP/PPgMA/CL15A = 75/25/5	2.16	4.10	2.02

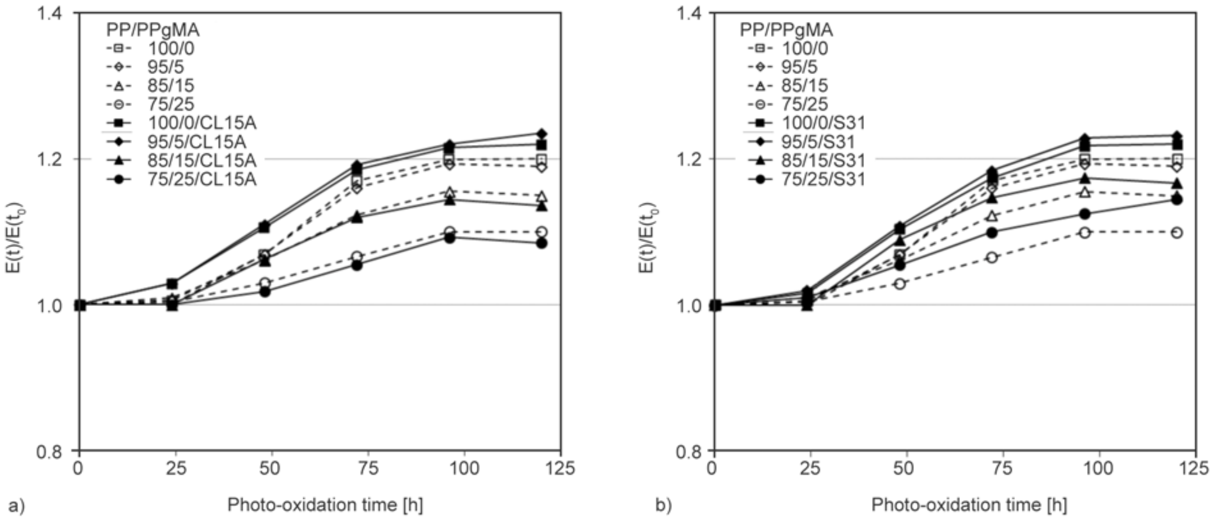

Figure 4. Dimensionless elastic modulus of samples at different PP/PPgMA ratios with (a) CL15A and (b) S31, as a function of the photo-oxidation times

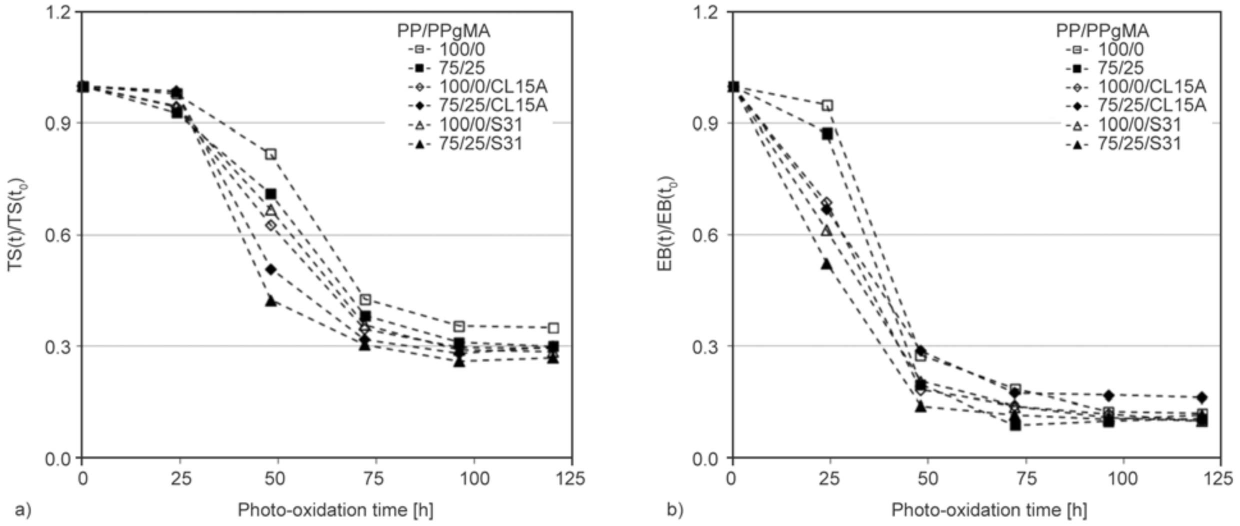

Figure 5. Dimensionless (a) tensile strength and (b) elongation at break of some investigated samples (at different PP/PPgMA ratios) as a function of the photo-oxidation times

sized fillers does not lead to significant differences in the increase of the elastic modulus, if compared to the unfilled binary blends. On the other hand, from all of the systems (binary blend, clay-filled nanocomposite and calcium carbonate filled nanocomposite) a clear tendency emerges, i.e. the decrease of the stiffening effect with time, when higher amounts of PPgMA are used; in other words, the presence of increasing amounts of PPgMA seems to lead to reduced photo-oxidation effects, although the differences are not striking.

The dimensionless tensile strength and elongation at break upon increasing the photo-oxidation time are reported in Figure 5a and 5b, respectively. The breaking properties experience a dramatic drop upon increasing the photo-oxidation time (especially after 48 h), while the presence of PPgMA and the variation of its percentage do not significantly change the overall behavior: the difficulties in extrapolating variations in the systems with different PPgMA amount and/or filler type are due, once more, to the previously mentioned heterogeneity of the investigated systems.

Carbonyl index (CI) is reported in Figure 6a and 6b, for CL15A and S31 filled nanocomposites, respectively, and compared with the unfilled binary blends. The diagrams show an expected increase of the CIs of all the investigated samples upon increasing the photo-oxidation time. However, a very clear trend emerges, which was already, at least partially, pres-

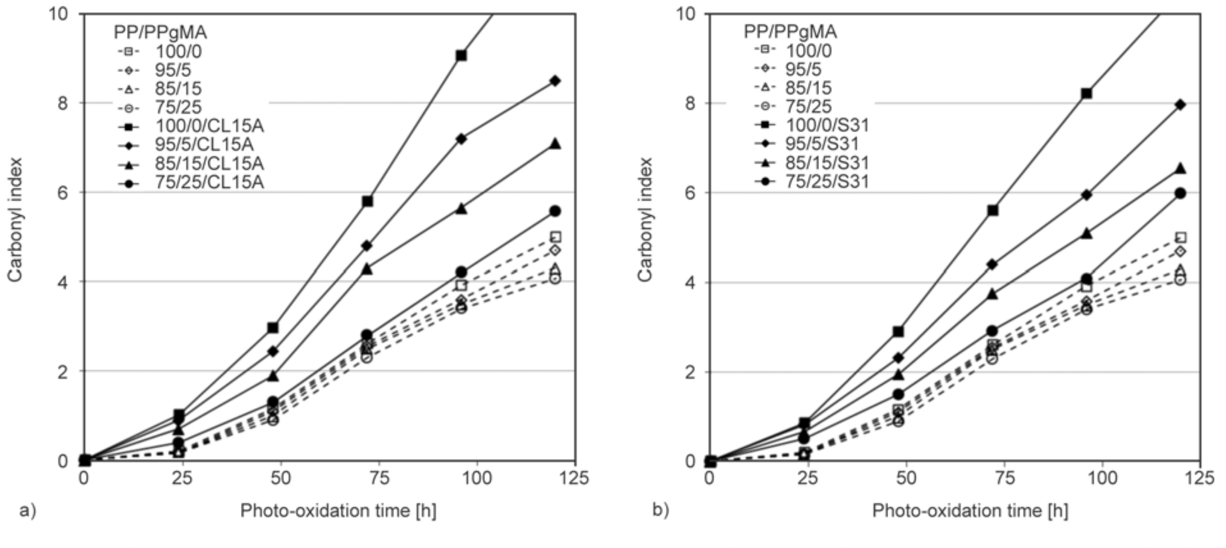

Figure 6. Carbonyl index of (a) CL15A and (b) S31 nanocomposites at different PP/PPgMA ratios, as a function the photo-oxidation times

ent in the previous discussed experimental observations on the mechanical behavior: the increase of CI is lower upon increasing the PPgMA, both in the unfilled binary blends and in the nanocomposites. This suggests that the presence of PPgMA actually reduces the photo-oxidation products formation. This is particularly true in the nanocomposites where, after 120 hours, the CIs of the systems at 75/25 PP-to-PPgMA ratios are approximately one half of those of the nanocomposites without PPgMA. This is a striking result, since it suggests that the addition of PPgMA to a PP based nanocomposite, filled with either organomodified clay or precipitated calcium carbonate, can reduce the photo-oxidation rates. As regards the role of the fillers alone (i.e. without taking into account the PPgMA), it can be stated that their presence leads to higher sensitivity to photo-oxidation, in agreement with our previous studies [19].

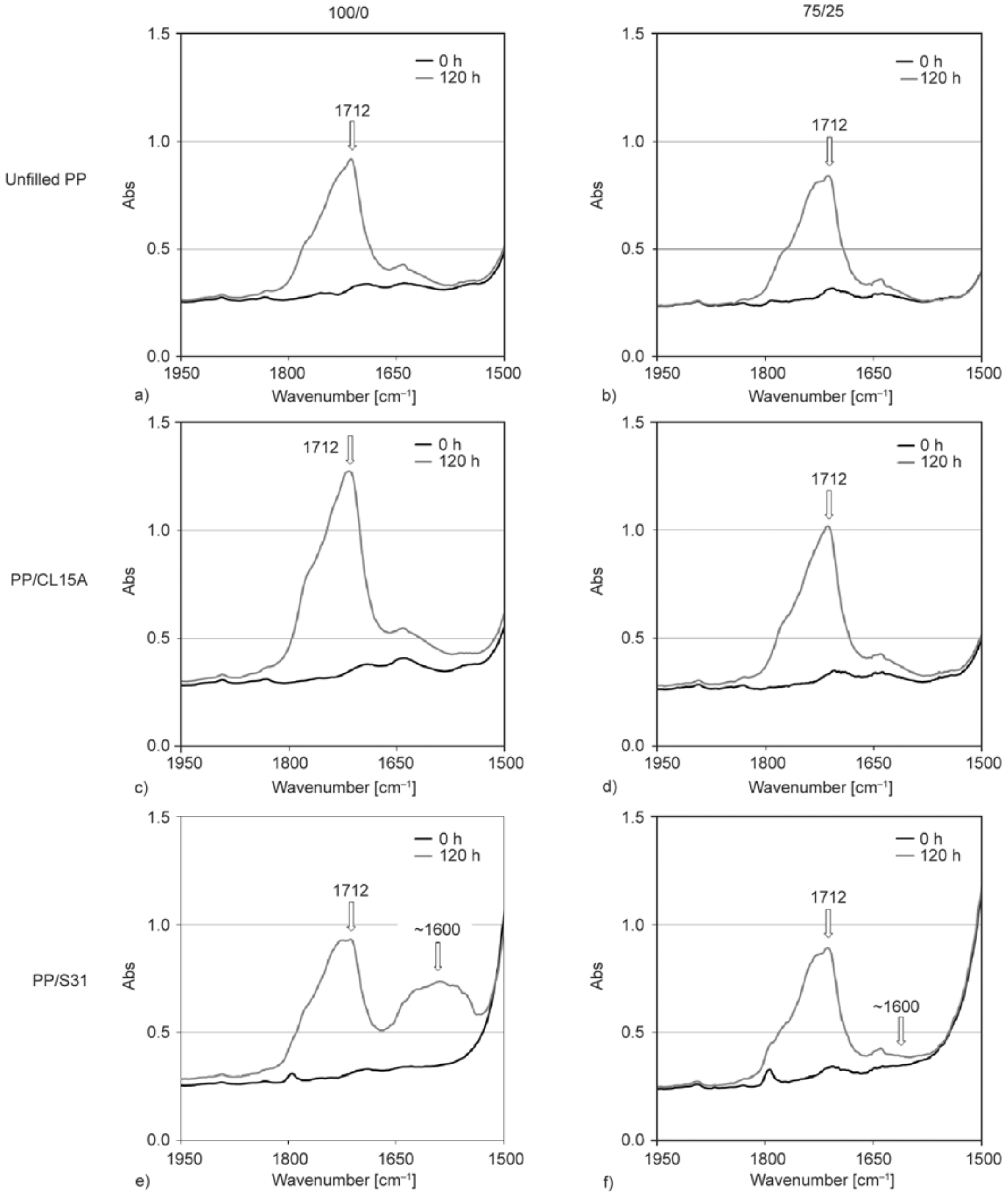

Figure 7. Carbonyl region of FT-IR spectra at 0 h and 120 h: (a) PP/PPgMA = 100/0, (b) PP/PPgMA = 75/25, (c) CL15A nanocomposites where PP/PPgMA = 100/0, (d) CL15A nanocomposites where PP/PPgMA = 75/25, (e) S31 nanocomposites where PP/PPgMA = 100/0, (f) S31 nanocomposites where PP/PPgMA = 75/25

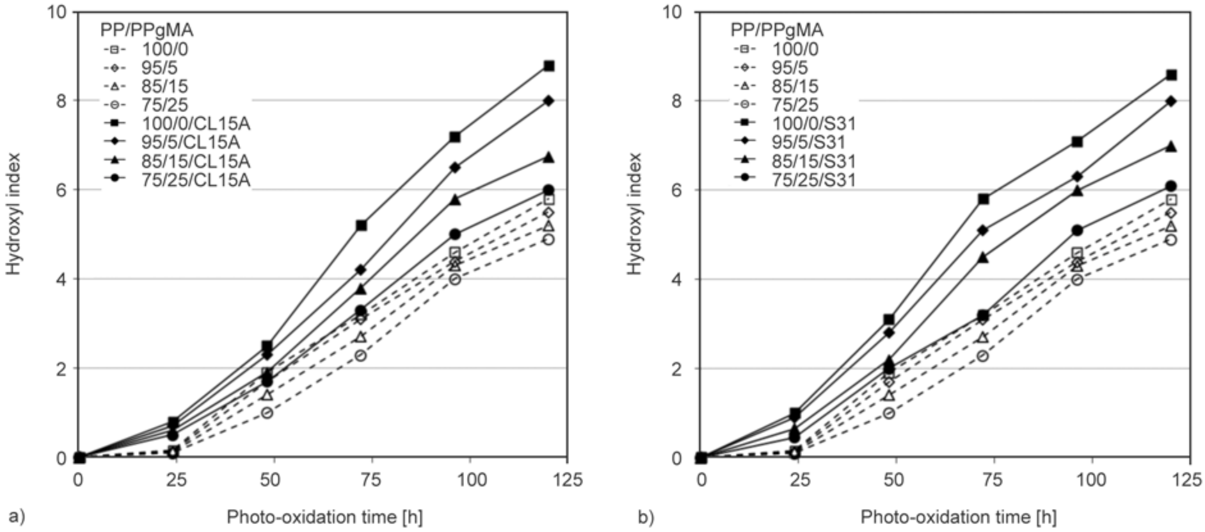

Figure 8. Hydroxyl index of (a) CL15A and (b) S31 nanocomposites at different PP/PPgMA ratios, as a function of the photo-oxidation times

The FT-IR spectra in the carbonyl region are reported in Figure 7a–7f. The spectra show the formation of a peak centered at 1712 cm^{-1} in PP, PP/CL15A and PP/S31 samples upon increasing the photo-oxidation time up to 120 h; furthermore, a wide band at approx. 1600 cm^{-1} appears in the PP/S31 sample after 120 h, while it is much less evident in the previous samples. This band is attributable to the formation of carboxylic acid salts during weathering, as a result of the reaction between carboxylic acids coming from the PP degradation, and the basic fillers (S31) used in the nanocomposites [19]. However, the situation is different as far as the systems with 75/25 PP-to-PPgMA ratio are concerned. In the case of the binary blend and the CL15A nanocomposite, the shapes of the peaks are similar to those found in the samples without the compatibilizer. With particular concern to the CL15A nanocomposite, the subtended area is significantly smaller, as already shown by the CI data, suggesting that the presence of PPgMA actually reduces the photo-oxidation products formation in the carbonyl region. This can be explained by considering that the acid sites formed onto the clay platelets during photo-oxidation (due to the Hoffmann elimination of the organomodifier [17]) are partially hindered by the presence of the maleic anhydride which creates a physical barrier. However, the results are even more interesting when the S31 nanocomposite is taken into account. The spectra clearly show that the band at 1600 cm^{-1} does not appear, even after 120 h of accelerated weathering. This suggests that the presence of a high amount of PPgMA hinders the reaction between the filler and the degradation products coming from the photo-oxidized PP, and thus the formation of carboxylic acid salts. This is probably due to the PPgMA encapsulating (at least partially, as already described in the discussion on the morphology) the S31 particles and thus slowing down the reactions with the carboxylic acids.

The above considerations regarding the role of PPgMA are proved also by the morphology improvements already investigated by SEM and TEM and discussed before. The complex morphology of both CL15A and S31 filled nanocomposites with 75/25 PP-to-PPgMA ratio is due to two contrasting effects, i.e. the blend formation and the effect of the filler. Finally, Figure 8 and Figure 9a–9f, report respectively the Hydroxyl index (HI) and the FT-IR spectra in the hydroxyl region of the same samples. The results confirm the observations done with regard to the carbonyl region: the presence of PPgMA reduces the formation of photo-oxidation products, increasingly upon increasing the PPgMA content.

4. Conclusions

In this work, the effect of the addition of different amounts of PPgMA to PP-based nanocomposites has been investigated. An accurate study on the mechanical behavior, as well as the morphology of the prepared systems before accelerated weathering has been carried out. It was found that the addition of PPgMA leads to a reduction of the elastic modulus of pristine PP, however it can also improve the adhesion between the filler and the polymer matrix, thus leading to improvements of the elastic modu-

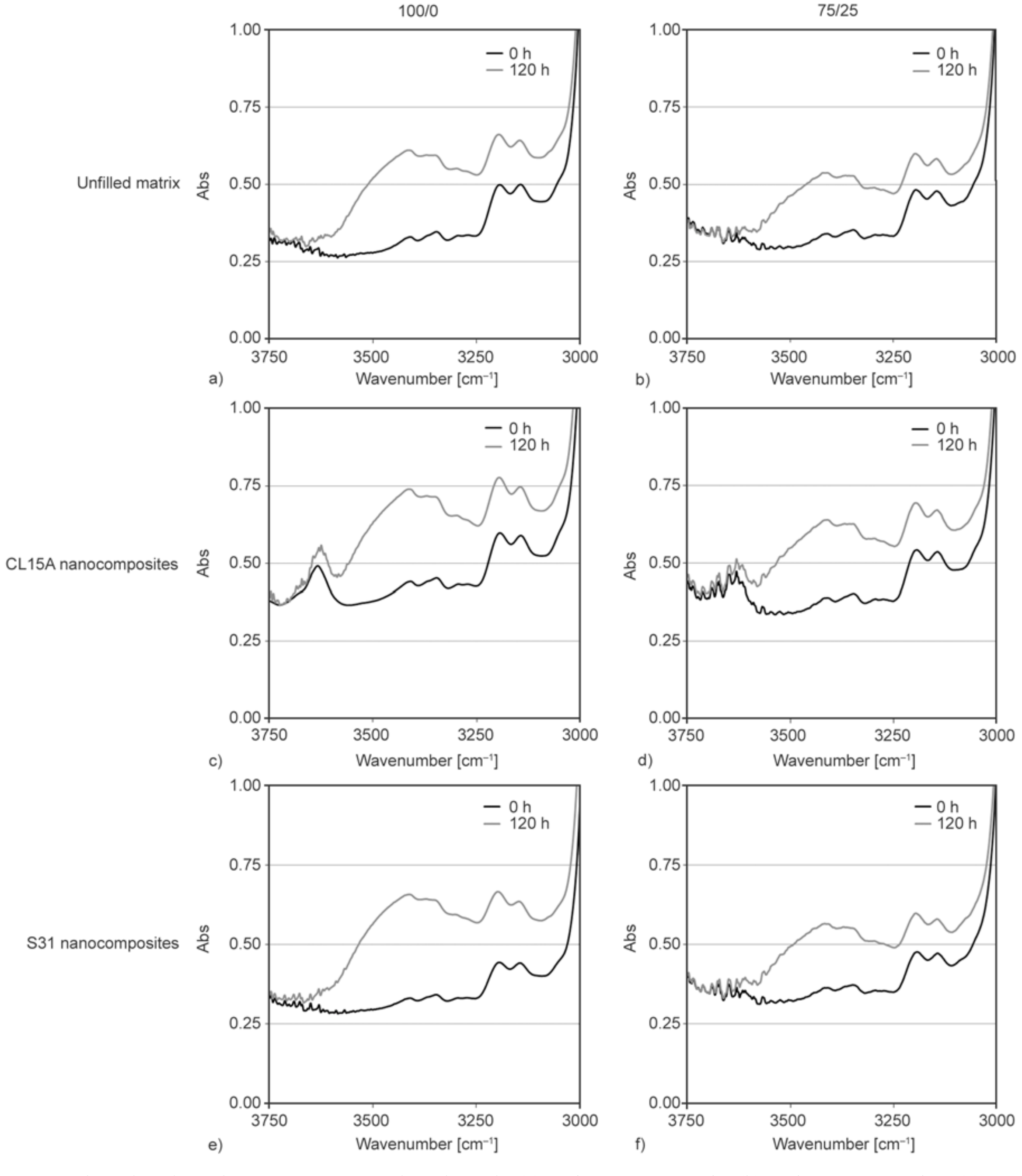

Figure 9. Hydroxyl region of FT-IR spectra at 0 h and 120 h: (a) PP/PPgMA = 100/0, (b) PP/PPgMA = 75/25, (c) CL15A nanocomposites where PP/PPgMA = 100/0, (d) CL15A nanocomposites where PP/PPgMA = 75/25, (e) S31 nanocomposites where PP/PPgMA = 100/0, (f) S31 nanocomposites where PP/PPgMA = 75/25

lus. On the other hand, higher amounts of PPgMA can also lead to the formation of heterogeneities which, in turn, affect the tensile strength and the elongation at break. However, the morphology was positively affected by the presence of PPgMA, especially in the case of clay-filled nanocomposites, where the clay morphology turned from predominantly intercalated to predominantly exfoliated.

The photo-oxidation behavior seems to be positively affected by the presence of PPgMA. From the mechanical properties standpoint, most of the systems appeared to have similar behavior starting from about 48 hours accelerated weathering, due to the heterogeneity of the systems; on the other hand, FT-IR analysis revealed that the addition of PPgMA significantly reduced the formation of photo-oxidation products in the nanocomposites; in particular, clay nanocomposites showed a reduced formation of photo-oxidation products in the carbonyl region, while calcium carbonate nanocomposites experienced a dramatic reduction in the formation of photo-oxidation products related to carboxylic acid salts, coming from the interaction between the basic filler and the photo-oxidation products from the PP.

Acknowledgements

This work has been financially supported by University of Palermo RS ex-60% (ORPA07XR52: 'Comportamento foto-ossidativo di sistemi multi-componenti a base polimerica').

References

[1] Usuki A., Kojima Y., Kawasumi M., Okada A., Fukushima Y., Kurauchi T.: Synthesis of nylon 6-clay hybrid. Journal of Materials Research, **8**, 1179–1184 (1993).
DOI: 10.1557/JMR.1993.1179

[2] Jordan J., Jacob K. I., Tannenbaum R., Sharaf M. A., Jasiuk I.: Experimental trends in polymer nanocomposites – A review. Materials Science and Engineering: A, **393**, 1–11 (2005).
DOI: 10.1016/j.msea.2004.09.044

[3] Pfaendner R.: Nanocomposites: Industrial opportunity or challenge? Polymer Degradation and Stability, **95**, 369–373 (2010).
DOI: 10.1016/j.polymdegradstab.2009.11.019

[4] Chan C-M., Wu J., Li J-X., Cheung Y-K.: Polypropylene/calcium carbonate nanocomposites. Polymer, **43**, 2981–2992 (2002).
DOI: 10.1016/S0032-3861(02)00120-9

[5] Lam T. D., Hoang T. V., Quang D. T., Kim J. S.: Effect of nanosized and surface-modified precipitated calcium carbonate on properties of $CaCO_3$/polypropylene nanocomposites. Materials Science and Engineering A, **501**, 87–93 (2009).
DOI: 10.1016/j.msea.2008.09.060

[6] Salvetat-Delmotte J. P., Rubio A.: Mechanical properties of carbon nanotubes: A fiber digest for beginners. Carbon, **40**, 1729–1734 (2002).
DOI: 10.1016/S0008-6223(02)00012-X

[7] Coleman J. N., Khan U., Blau W. J., Gun'ko Y. K.: Small but strong: A review of the mechanical properties of carbon nanotube–polymer composites. Carbon, **44**, 1624–1652 (2006).
DOI: 10.1016/j.carbon.2006.02.038

[8] Filippi S., Dintcheva N. Tz., Scaffaro R., La Mantia F. P., Polacco G., Magagnini P.: Effects of organoclay on morphology and properties of nanocomposites based on LDPE/PA-6 blends without and with SEBS-*g*-MA compatibilizer. Polymer Engineering and Science, **49**, 1187–1197 (2009).
DOI: 10.1002/pen.21361

[9] La Mantia F. P., Dintcheva N. Tz., Malatesta V., Pagani F.: Improvement of photo-stability of LLDPE-based nanocomposites. Polymer Degradation and Stability, **91**, 3208–3213 (2006).
DOI: 10.1016/j.polymdegradstab.2006.07.014

[10] Shah R. K., Paul D. R.: Organoclay degradation in melt processed polyethylene nanocomposites. Polymer, **47**, 4075–4084 (2006).
DOI: 10.1016/j.polymer.2006.02.031

[11] Morlat-Therias S., Fanton E., Gardette J. L., Dintcheva N. T., La Mantia F. P., Malatesta V.: Photochemical stabilization of linear low-density polyethylene/clay nanocomposites: Towards durable nanocomposites. Polymer Degradation and Stability, **93**, 1776–1780 (2008).
DOI: 10.1016/j.polymdegradstab.2008.07.031

[12] Qin H., Zhao C., Zhang Z., Chen G., Yang M.: Photo-oxidative degradation of polyethylene/montmorillonite nanocomposite. Polymer Degradation and Stability, **81**, 497–500 (2003).
DOI: 10.1016/S0141-3910(03)00136-8

[13] Mailhot B., Morlat S., Gardette J-L., Boucard S., Duchet J., Gérard J-F.: Photodegradation of polypropylene nanocomposites. Polymer Degradation and Stability, **82**, 163–167 (2003).
DOI: 10.1016/S0141-3910(03)00179-4

[14] Botta L., Dintcheva N. Tz., La Mantia F. P.: The role of organoclay and matrix type in photo-oxidation of polyolefin/clay nanocomposite films. Polymer Degradation and Stability, **94**, 712–718 (2009).
DOI: 10.1016/j.polymdegradstab.2008.12.017

[15] Leroux F., Meddar L., Mailhot B., Morlat-Therias S., Gardette J-L.: Characterization and photooxidative behaviour of nanocomposites formed with polystyrene and LDHs organo-modified by monomer surfactant. Polymer, **46**, 3571–3578 (2005).
DOI: 10.1016/j.polymer.2005.03.044

[16] Morlat-Therias S., Mailhot B., Gonzalez D., Gardette J-L.: Photooxidation of polypropylene/montmorillonite nanocomposites. 2. Interactions with antioxidants. Chemistry of Materials, **17**, 1072–1078 (2005).
DOI: 10.1021/cm040172l

[17] Dintcheva N. Tz., Al-Malaika S., La Mantia F. P.: Effect of extrusion and photo-oxidation on polyethylene/clay nanocomposites. Polymer Degradation and Stability, **94**, 1571–1588 (2009).
DOI: 10.1016/j.polymdegradstab.2009.04.012

[18] Li J., Yang R., Yu J., Liu Y.: Natural photo-aging degradation of polypropylene nanocomposites. Polymer Degradation and Stability, **93**, 84–89 (2008).
DOI: 10.1016/j.polymdegradstab.2007.10.022

[19] Morreale M., Dintcheva N. T., La Mantia F. P.: The role of filler type in the photo-oxidation behaviour of micro- and nano-filled polypropylene. Polymer International, **60**, 1107–1116 (2011)
DOI: 10.1002/pi.3049

[20] La Mantia F. P., Morreale M.: Accelerated weathering of polypropylene/wood flour composites. Polymer Degradation and Stability, **93**, 1252–1258 (2008)
DOI: 10.1016/j.polymdegradstab.2008.04.006

[21] La Mantia F. P., Morreale M., Scaffaro R., Tulone S.: Rheological and mechanical behavior of LDPE/calcium carbonate nanocomposites and microcomposites. Journal of Applied Polymer Science, **127**, 2544–2552 (2013).
DOI: 10.1002/app.37875

[22] Krimm S.: Infrared spectra of high polymers. Advances in Polymer Science, **2**, 51–172 (1960).
DOI: 10.1007/BFb0050351

[23] Tokihisa M., Yakemoto K., Sakai T., Utracki L. A., Sepehr M., Li J., Simard Y.: Extensional flow mixer for polymer nanocomposites. Polymer Engineering and Science, **46**, 1040–1050 (2006).
DOI: 10.1002/pen.20542

[24] Harrats C., Thomas S., Groeninckx G.: Micro- and nanostructured multiphjase polymer blend systems. CRC Press, Boca Raton (2006).

[25] Scaffaro R., Morreale M., Mirabella F., La Mantia F. P.: Preparation and recycling of plasticized PLA. Macromolecular Materials and Engineering, **296**, 141–150 (2011).
DOI: 10.1002/mame.201000221

[26] García-López D., Gobernado-Mitre I., Merino J. C., Pastor J. M.: Effect of the amount and funtionalization grade of PPgMA compatibilization agent in polypropylene/clay nanocomposites. Polymer Bulletin, **59**, 667–676 (2007).
DOI: 10.1007/s00289-007-0810-9

[27] Sahoo S., Ambre A., Jagtap R.: Effect of functionality and melt flow index of maleic anhydride grafted polypropylene on polypropylene clay nanocomposites. Journal of Polymer Materials, **25**, 601–612 (2008).

[28] Filippone G., Dintcheva N. Tz., La Mantia F. P., Acierno D.: Using organoclay to promote morphology refinement and co-continuity in high-density polyethylene/polyamide 6 blends – Effect of filler content and polymer matrix composition. Polymer, **51**, 3956–3965 (2010).
DOI: 10.1016/j.polymer.2010.06.044

[29] Filippone G., Dintcheva N. Tz., La Mantia F. P., Acierno D.: Selective localization of organoclay and effects on the morphology and mechanical properties of LDPE/PA11 blends with distributed and co-continuous morphology. Journal of Polymer Science Part B: Polymer Physics, **48**, 600–609 (2010).
DOI: 10.1002/polb.21928

eXPRESS Polymer Letters Vol.7, No.8 (2013) 716–721
Available online at www.expresspolymlett.com
DOI: 10.3144/expresspolymlett.2013.68

Influence of TiO_2 nanoparticles on the optical and structural properties of PPV thin films converted at low temperatures

B. Rostirolla[1], E. Laureto[1], M. A. T. da Silva[1], H. de Santana[2], I. F. L. Dias[1], J. L. Duarte[1]*

[1]Group of Optics and Optoeletronics, Physics Department, State University of Londrina, Londrina – Paraná, Brazil
[2]Electroactive Materials and Interfaces, Chemistry Department, State University of Londrina, Londrina – Paraná, Brazil

Received 4 March 2013; accepted in revised form 11 May 2013

Abstract. In this work we studied the optical properties of poly(p-phenylene vinylene) (PPV) produced by the thermal conversion of a precursor polymer blended with a synthetic dye (Reactive Black 5). The production of PPV by this method decreases the overall time and cost of the process. We observed that the introduction of the dye resulted in an additional absorbance band near 550–700 nm, which can be beneficial to the photon harvesting capacity of the polymer if it is used as the donor material in a photovoltaic device. We studied how the optical and structures properties of this blend change when different quantities of TiO_2 nanoparticles are introduced. For that, thin films were produced by the cast deposition of pre-PPV:dye:TiO_2. The scanning electronic microscopic images showed that the inorganic semiconductor form large agglomerates of approximately 200 nm, indicating a very rough surface where the dye can be adsorbed. The analysis of photoluminescence and Raman peaks indicated a reduction of the mean conjugation length of the polymer chains in the presence of TiO_2 nanoparticles.

Keywords: *polymer composites, nanomaterials, PPV and dye*

1. Introduction

Organic electronics is one of top rising research fields nowadays, the understanding of how we can manipulate organic materials and their physical properties have opened field to several applications, e.g. organic solar cells [1, 2], OLEDs [3, 4], etc. Some of these devices, like the dye-sensitized solar cell [5], put together organic compounds and inorganic semiconductor nanoparticles in order to absorb sunlight and transport charge carriers. The inclusion of metallic or semiconductor nanoparticles changes the optical properties of the polymers [6–11], resulting in new characteristics of the materials that can be explored to technologic applications. In this sense, knowing how inorganic nanoparticles influence organic materials is extremely important.

Even with its relatively low conductivity, poly(p-phenylene vinylene) (PPV) is one of the conjugated polymers used in solar cell fabrication [12, 13]. Its precursor, poly(p-xylene tetrahydrothiophenium chloride) (PTHT), is soluble in water, a characteristic that is getting increasing importance due to the increasing concern on environmental and safety problems related to the organic solvents [12, 14–16]. The thermal treatment of PPV's precursor is the conventional route to produce PPV, but the resulting film has some chain defects, due to the high temperatures (above 200°C) used, undermining its conductivity [17]. In addition, high temperature severely affects the properties of indium-tin oxide (ITO)/polymeric layer interface, as reported by Poças *et al*. [18]. To reduce the harmful effect of the thermal treatment, PPV can be produced by an alternative route in which a compound having a SO_3^- group is incorporated [19] (Figure 1). These compounds replaces the chloride anions present on

---

*Corresponding author, e-mail: bruno.rostirolla@hotmail.com

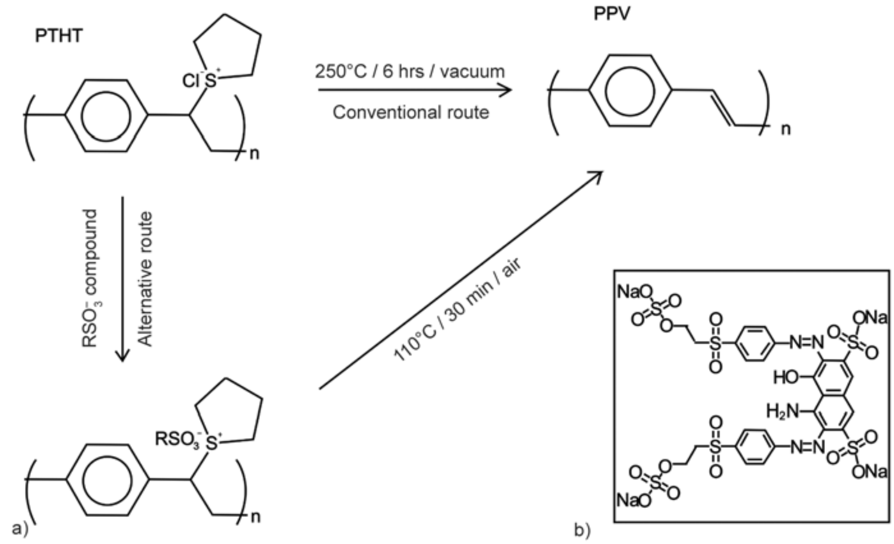

Figure 1. Conventional and alternative route of PPV's production (a). Chemical structure of Reactive Black 5 (b).

the precursor with the radical SO_3^-, facilitating the thermal elimination and reducing the thermal energy activation [19]. Many synthetic dyes exhibit this group and have been used to help the conversion of PPV [20].

In this work we used the dye Reactive Black 5 to produce PPV thin films from the alternative route proposed by Marletta *et al.* [19, 20]. It was observed that, in addition to allowing the conversion of the PPV precursor at lower temperatures, the PPV:dye film presented an absorption band extended to longer wavelengths, which is broader than absorbance of PPV produced without the dye. This can be beneficial to light harvesting capacity of this compound, if it is used as donor material in an active layer of a photovoltaic device. Different amounts of TiO_2 (acceptor material) were then added to the polymer solution, to see how this mixture reacts in the presence of inorganic nanoparticles. All components, dissolved in aqueous solution, were cast-deposited to form a bulk layer film, and the optical and structural properties of these blends were investigated by absorbance, photoluminescence (PL), Raman scattering and Scanning Electron Microscopy (SEM) techniques.

2. Experimental procedures

All solutions and films were prepared under ambient conditions, using ultrapure water (resistivity 18.2 MΩ/cm). Reactive Black 5 (code 306452) and PTHT (code 540765) were purchased from Sigma-Aldrich (USA) and TiO_2 nanoparticles (P25 Aeroxide; 70/30 anatase/rutile; $d \approx 20$ nm) from Evonik-Degussa (Germany). The mixing ratio between PTHT and dye was 1:1 (mol/mol), and their molarities were $1{,}25\cdot10^{-3}$ M. The concentration of TiO_2 solution was 2 mg/mL. All solutions were first magnetically stirred for 15 min and put at ultrasonic bath for another 15 min. After mixing PPV's precursor, Reactive Black 5 and TiO_2, the resulting solution was again magnetically stirred and put at ultrasonic bath. The following samples were made using glass as substrate: (a) 100 µL PTHT/dye; (b) 100 µL PTHT/dye + 10 µL TiO_2; (c) 100 µL PTHT/dye + 50 µL TiO_2; (d) 100 µL PTHT/dye + 200 µL TiO_2. All samples were cast-deposited and stored, protected from any light, for the period of 24 hours for water evaporation. After that, the samples were heated at 110°C for 30 minutes in air and in a homemade oven, according to [20]. The UV-Vis absorbance was measured by using a DT-Mini-2-GS model UV-Vis lamp and an USB-4000 minispectrometer (Ocean Optics). The same spectrometer was used to detect the PL of the films, whereas a solid-state laser (λ = 405 nm) was used as excitation source. During the PL measurements, the samples were under rough vacuum (10^{-2} mbar). The Raman spectra were obtained with a portable spectrometer Raman Advantage532® from Delta Nu, excited in 532 nm. NuSpec software from Delta Nu was used, making use of baseline resources, in order to remove the background fluorescence. To make SEM images, first an Au layer of approximately 40 nm was deposited using Bal-Tec SCD OSO sputter coater.

SEM images were made using FEI Quanta 200 SEM. All measures were performed at room temperature.

3. Results and discussion

The normalized absorbance of pure PPV, samples (a) and (b), all made by the alternative route are shown in Figure 2. This route reduces the preparation time and overall cost of the sample, since it uses a faster thermal treatment at lower temperature when compared to the conventional route. The maximum of the absorption, near 450 nm, is a signature of converted PPV. The absorption band in 550–700 nm is only present when the dye is introduced, since standard PPV ends its absorption near 530 nm [21]. This extra absorption band can increase the quantity of photons collected in the farther region of the solar spectrum, offering the possibility to enhance the overall efficiency of photovoltaic devices. The introduction of TiO_2 nanoparticles increases the thin films opacity, as seen in Figure 2 (black curve, baseline corrected). However, the PPV absorption band (~450 nm) and the dye absorption band (~650 nm) are still present. After the thermal treatment of 110°C, PPV+dye films exhibit characteristics of PPV made by the conventional route [21].

The Raman spectra of all samples made in this work are shown in Figure 3. Also the spectra of pure PPV film and of the dye aqueous solution were included in this figure. The pure PPV sample was made with the 1:1 mol/mol proportion between PTHT and DBS (sodium dodecylbenzenesulfonate) [19].

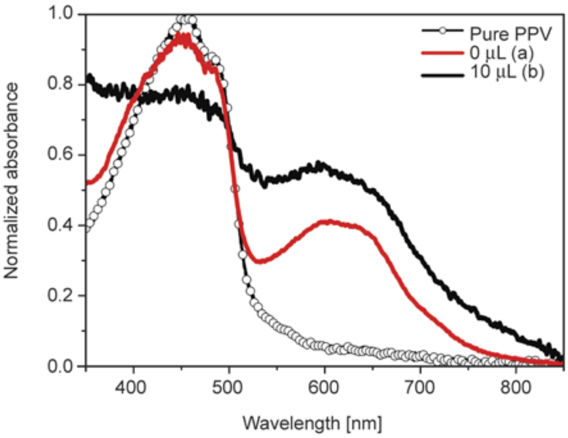

Figure 2. Normalized absorbance of pure PPV (line with circles), samples with 0 (a) and 10 µL (b) of TiO_2 (red and black lines, respectively). All samples were produced following the alternative route. The pure PPV sample was made using DBS (sodium dodecylbenzenesulfonate) as SO_3^- compound. The baselines of all spectra were corrected.

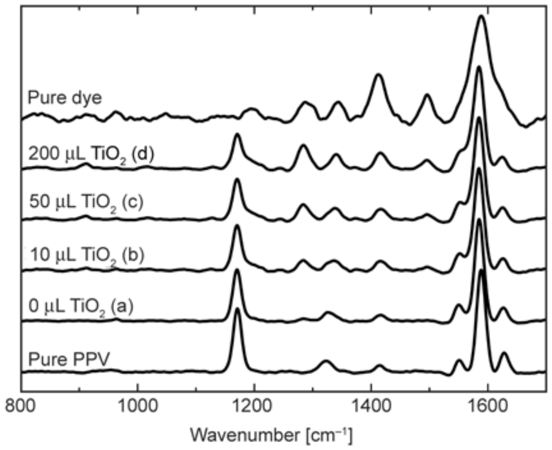

Figure 3. Raman spectra of the samples. Anatase and rutile peaks of TiO_2 are only visible in the range of 600 cm^{-1} (not showed here).

The assignments of the most important Raman peaks are shown in Table 1 [22–24]. The peaks at 1284 and 1496 cm^{-1} are exclusive from the dye, since the naphthalene group and the C–N bound are only present in Reactive Black 5's structure. The introduction of TiO_2 nanoparticles leads to an increase of intensity of these peaks, suggesting that a portion of dye molecules is remaining intact after the thermal treatment. Another important aspect is the behavior of the peak at 1170 cm^{-1}, which is exclusive from PPV. Its intensity decreases as the quantity of TiO_2 increase, showing that less converted films are produced. This indicates that a portion of dye molecules can be adsorbed on the surface of TiO_2 and is not participating in the chemical reaction with the PPV precursor.

We believe that the dye is adsorbing in the TiO_2's very rough surface, since its particles dimensions are in the range of 20 nm. These small particles however, form large clusters of approximately 200 nm, as shown in SEM image of sample (d) (Fig-

Table 1. Assignment of important peaks of Raman spectra of samples [22–24]

Wavenumber [cm⁻¹]	Attribution
1170	C–C stretching + C–H bending of the phenyl ring
1284	C=C stretching of the naphthalene group
1323	C=C stretching + C–H bending of the vinyl group
1496	C–N vibration
1550	C=C stretching of the phenyl ring
1585	C–C stretching of the phenyl ring
1625	C=C stretching of the vinyl group

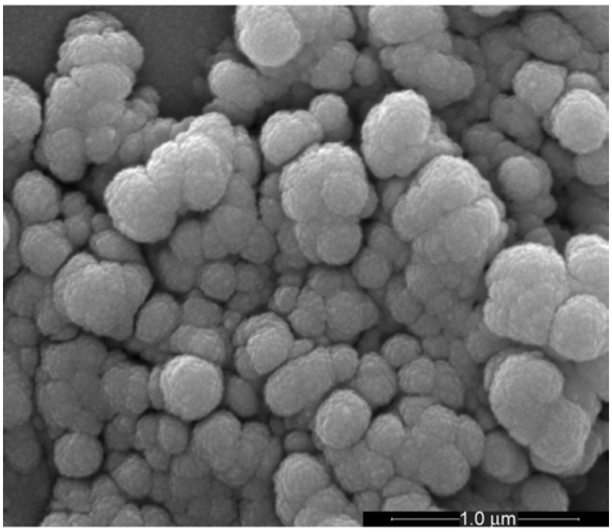

Figure 4. SEM images of TiO_2 nanoparticles in sample d). The large clusters (around 200 nm) are formed by the small particles (approximately 20 nm).

ure 4). We observed, as expected, that as the amount of TiO_2 increased, the number of clusters also increased. Although these large clusters can result in films with high surface roughness, the polymer could easily penetrate this matrix and have a substantial contact with the inorganic particles, which is extremely important to rapidly dissociate the excitons [25].

The presence of TiO_2 interferes in the photoluminescence spectra, as seen in Figure 5. Even the smallest quantity results in a blue-shift of approximately 17 nm. As the number of nanoparticles increases, the photoluminescence intensity increases up to 7 times. This is contrary to the PL quenching expected due to donor-acceptor interaction [7, 12, 14, 26, 27]. However, the PL enhancement was also observed in other works using different materials mixed with PPV [28–30].

Son *et al.* [31] and Zhang *et al.* [32] showed that a break on the conjugation length of PPV leads to an enhanced photoluminescence. In the work of Son, they engineered cis linkages into the PPV chain. These cis linkages interrupt the conjugation and interfere with the packing of the polymer chains, resulting in a gain of photoluminescence [31]. Zhang *et al.* made several thermal treatments on PPV's precursor using different temperatures. They observed that as the temperature increases, the PL intensity decreases, indicating that partially conjugated PPV have enhanced photoluminescence [32]. Our observations corroborates with these works: both PL blue shift and enhanced PL intensity is showing that PPV:dye mixed with TiO_2 results in smaller conjugated segments than pure PPV. The presence of dye molecules adsorbed on the TiO_2 surface, as suggested by the results of Raman scattering, may indicate that the amount of dye participating in the ion exchange with the pre-PPV decreased, resulting in less conjugated PPV chains after the thermal conversion, which explains the PL blue shift. Moreover, the formation of large agglomerates of TiO_2 may be affecting the inter-chain polymer interaction, resulting in a greater localization of the photogenerated carriers and therefore increasing the PL intensity. Thus, both agglomeration of TiO_2 nanoparticles and the availability of dye molecules to participate in the PPV conversion process must be controlled to produce PPV:dye:TiO_2 blends in which the polymer chains have larger effective conjugation length.

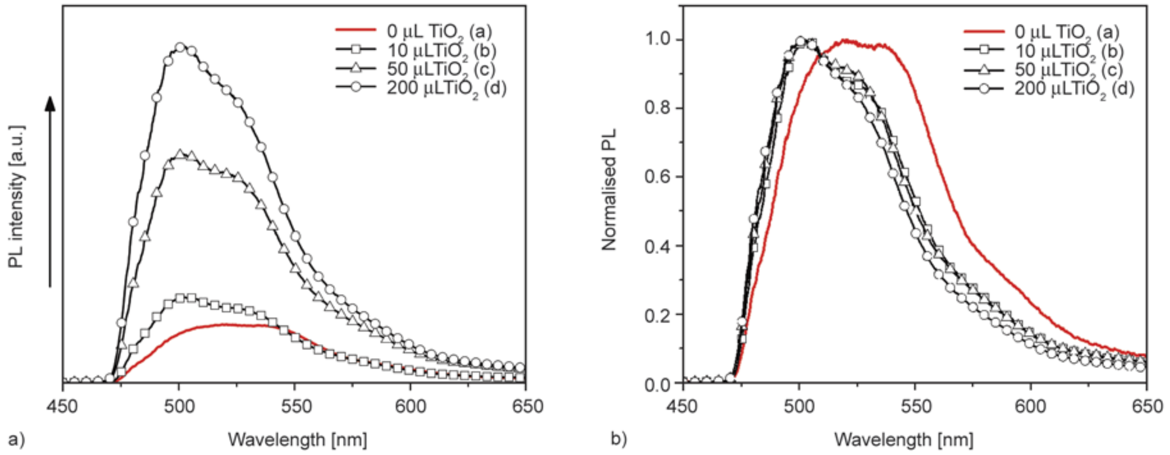

Figure 5. Photoluminescence spectra (a) and normalized photoluminescence spectra (b) of the samples

4. Conclusions

PPV thin films were produced by an alternative route, adding Reactive Black 5 dye to the precursor polymer solution. The dye enabled the conversion of PPV at lower temperatures than that used conventionally, and led to a gain of absorption at the region of 550–700 nm, where the pure PPV is optically inert. Raman scattering analysis showed that more dye molecules remain intact after the thermal conversion when TiO_2 nanoparticles are incorporated into pre-PPV:dye mixture. The SEM images showed the formation of TiO_2 agglomerates with diameter around 200 nm. The enhanced intensity and the blue-shift observed in the PL spectra were due to the formation of partially conjugated PPV when TiO_2 is introduced. However, the additional absorption band towards longer wavelengths increases the light harvesting capacity of the film, therefore enhancing the possibility to use this blend as active layer in free organic solvent photovoltaic devices.

Acknowledgements

The authors would like to acknowledge the financial support granted by the Brazilian agencies Conselho Nacional de Desenvolvimento Científico e Tecnológico (CNPq) and Coordenação de Aperfeiçoamento de Pessoal de Nível Superior (CAPES). We would also like to acknowledge the Laboratório de Microscopia Eletrônica e Microanálise/UEL for the SEM images.

References

[1] Günes S., Neugebauer H., Sariciftci N. S.: Conjugated polymer-based organic solar cells. Chemical Reviews, **107**, 1324–1338 (2007). DOI: 10.1021/cr050149z

[2] Bian L., Zhu E., Tang J., Tang W., Zhang F.: Recent progress in the design of narrow bandgap conjugated polymers for high-efficiency organic solar cells. Progress in Polymer Science, **37**, 1292–1331 (2012). DOI: 10.1016/j.progpolymsci.2012.03.001

[3] Thejo Kalyani N., Dhoble S. J.: Organic light emitting diodes: Energy saving lighting technology – A review. Renewable and Sustainable Energy Reviews, **16**, 2696–2723 (2012). DOI: 10.1016/j.rser.2012.02.021

[4] Yersin H., Rausch A. F., Czerwieniec R., Hofbeck T., Fischer T.: The triplet state of organo-transition metal compounds. Triplet harvesting and singlet harvesting for efficient OLEDs. Coordination Chemistry Reviews, **255**, 2622–2652 (2011). DOI: 10.1016/j.ccr.2011.01.042

[5] Ito S., Murakami T. N., Comte P., Liska P., Grätzel C., Nazeeruddin M. K., Grätzel M.: Fabrication of thin film dye sensitized solar cells with solar to electric power conversion efficiency over 10%. Thin Solid Films, **516**, 4613–4619 (2008). DOI: 10.1016/j.tsf.2007.05.090

[6] Kim M. S., Park D. H., Cho E. H., Kim K. H., Park Q-H., Song H., Kim D-C., Kim J., Joo J.: Complex nanoparticle of light-emitting MEH-PPV with Au: Enhanced luminescence. ACS Nano, **3**, 1329–1334 (2009). DOI: 10.1021/nn900071w

[7] Szymanski C., Wu C., Hooper J., Salazar M. A., Perdomo A., Dukes A., McNeill J.: Single molecule nanoparticles of the conjugated polymer MEH−PPV, preparation and characterization by near-field scanning optical microscopy. The Journal of Physical Chemistry B, **109**, 8543–8546 (2005). DOI: 10.1021/jp051062k

[8] Saikia G., Murugadoss A., Sarmah P. J., Chattopadhyay A., Iyer P. K.: Tuning the optical characteristics of poly(p-phenylenevinylene) by in situ Au nanoparticle generation. The Journal of Physical Chemistry B, **114**, 14821–14826 (2010). DOI: 10.1021/jp104452z

[9] Chen X. C., Green P. F.: Control of morphology and its effects on the optical properties of polymer nanocomposites. Langmuir, **26**, 3659–3665 (2010). DOI: 10.1021/la903108u

[10] Wu C., Szymanski C., McNeill J.: Preparation and encapsulation of highly fluorescent conjugated polymer nanoparticles. Langmuir, **22**, 2956–2960 (2006). DOI: 10.1021/la060188l

[11] Huynh W. U., Dittmer J. J., Alivisatos A. P.: Hybrid nanorod-polymer solar cells. Science, **295**, 2425–2427 (2002). DOI: 10.1126/science.1069156

[12] Dong Q., Yu W., Li Z., Yao S., Zhang X., Yang B., Im C., Tian W.: All-water-solution processed solar cells based on PPV and TiO_2 nanocrystals. Solar Energy Materials and Solar Cells, **104**, 75–80 (2012). DOI: 10.1016/j.solmat.2012.04.024

[13] Vats T., Sharma S. N., Kumar M., Kar M., Jain K., Singh V. N., Mehta B. R., Narula A. K.: Comparison of photostability, optical and structural properties of TiO_2/conjugated polymer hybrid composites prepared via different methods. Thin Solid Films, **519**, 1100–1105 (2010). DOI: 10.1016/j.tsf.2010.08.051

[14] Wang M., Wang X.: PPV/TiO_2 hybrid composites prepared from PPV precursor reaction in aqueous media and their application in solar cells. Polymer, **49**, 1587–1593 (2008). DOI: 10.1016/j.polymer.2008.01.061

[15] Søndergaard R., Helgesen M., Jørgensen M., Krebs F. C.: Fabrication of polymer solar cells using aqueous processing for all layers including the metal back electrode. Advanced Energy Materials, **1**, 68–71 (2011). DOI: 10.1002/aenm.201000007

[16] Wei H., Zhang H., Sun H., Yang B.: Preparation of polymer–nanocrystals hybrid solar cells through aqueous approaches. Nano Today, **7**, 316–326 (2012).
DOI: 10.1016/j.nantod.2012.06.005

[17] Halliday D. A., Burn P. L., Friend R. H., Holmes A. B.: A study on the elimination reaction of sulfonium polyelectrolyte precursor polymers to poly(*p*-phenylenevinylene). Journal of the Chemical Society, Chemical Communications, **1992**, 1685–1687 (1992).
DOI: 10.1039/C39920001685

[18] Poças L. C., Nogueira S. L., Nobuyasu R. S., Dalkiranis G. G., Pires M. J. M., Tozoni J. R., Silva R. A., Marletta A.: Decreased degradation of poly(*p*-phenylene vinylene) films at the indium–tin oxide interface. Journal of Materials Science, **46**, 2644–2648 (2011).
DOI: 10.1007/s10853-010-5119-7

[19] Marletta A., Gonçalves D., Oliveira O. N., Faria R. M., Guimarães F. E. G.: Rapid conversion of poly(*p*-phenylenevinylene) films at low temperatures. Advanced Materials, **12**, 69–74 (2000).
DOI: 10.1002/(sici)1521-4095(200001)12:1<69::aid-adma69>3.0.co;2-6

[20] Marletta A., Silva G. B., Silva R. A., dos Santos Jr D. S., Oliveira Jr O. N.: Influence from the sulfonate group (RSO_3^-) on the conversion process and emission efficiency of poly(p-phenylene vinylene). Journal of Luminescence, **130**, 1230–1237 (2010).
DOI: 10.1016/j.jlumin.2010.02.030

[21] Laureto E., da Silva M. A. T., Fernandes R. V., Duarte J. L., Dias I. F. L., Marletta A.: Thickness effects on the optical properties of layer-by-layer poly(*p*-phenylene vinylene) thin films and their use in energy-modulated structures. Current Applied Physics, **12**, 870–874 (2012).
DOI: 10.1016/j.cap.2011.11.023

[22] Mulazzi E., Ripamonti A., Wery J., Dulieu B., Lefrant S.: Theoretical and experimental investigation of absorption and Raman spectra of poly(paraphenylene vinylene). Physical Review B, **60**, 16519–16525 (1999).
DOI: 10.1103/PhysRevB.60.16519

[23] Abbott L. C., Batchelor S. N., Smith J. R. L., Moore J. N.: Resonance raman and UV–visible spectroscopy of black dyes on textiles. Forensic Science International, **202**, 54–63 (2010).
DOI: 10.1016/j.forsciint.2010.04.026

[24] Lucilha A. C., Bonancêa C. E., Barreto W. J., Takashima K.: Adsorption of the diazo dye Direct Red 23 onto a zinc oxide surface: A spectroscopic study. Spectrochimica Acta Part A: Molecular and Biomolecular Spectroscopy, **75**, 389–393 (2010).
DOI: 10.1016/j.saa.2009.10.046

[25] Brabec C. J., Gowrisanker S., Halls J. J. M., Laird D., Jia S., Williams S. P.: Polymer–fullerene bulk-heterojunction solar cells. Advanced Materials, **22**, 3839–3856 (2010).
DOI: 10.1002/adma.200903697

[26] Peng F., Wu J., Li Q., Wang Y., Yue G., Xiao Y., Li Q., Lan Z., Fan L., Lin J., Huang M.: Semiconducting polymer-incorporated nanocrystalline TiO_2 particles for photovoltaic applications. Electrochimica Acta, **56**, 5184–5188 (2011).
DOI: 10.1016/j.electacta.2011.03.045

[27] Sang G., Zou Y., Huang Y., Zhao G., Yang Y., Li Y.: All-polymer solar cells based on a blend of poly[3-(10-*n*-octyl-3-phenothiazine-vinylene)thiophene-co-2,5-thiophene] and poly[1,4-dioctyloxyl-*p*-2,5-dicyanophenylenevinylene]. Applied Physics Letters, **94**, 193302/1–193302/3 (2009).
DOI: 10.1063/1.3134490

[28] Chang W-P., Whang W-T.: The electroluminescence and photoluminescence characteristics of films of poly(phenylene vinylene)/gel-glass interpenetrating networks. Polymer, **37**, 4229–4234 (1996).
DOI: 10.1016/0032-3861(96)00271-6

[29] Lee C-Y., Choi Y-J., Yoon S., Park H-H.: Effect of Ag nanoparticles on the electron energy structure and electrical properties of poly(*p*-phenylene vinylene) (PPV). Synthetic Metals, **160**, 621–624 (2010).
DOI: 10.1016/j.synthmet.2009.12.018

[30] Lee C-Y., Choi Y-J., Park H-H.: Electrical properties of poly(*p*-phenylene vinylene) films with an incorporation of platinum metal nanoparticles. Journal of Applied Polymer Science, **119**, 811–815 (2011).
DOI: 10.1002/app.32788

[31] Son S., Dodabalapur A., Lovinger A. J., Galvin M. E.: Luminescence enhancement by the introduction of disorder into poly(*p*-phenylene vinylene). Science, **269**, 376–378 (1995).
DOI: 10.1126/science.269.5222.376

[32] Zhang C., Braun D., Heeger A. J.: Light-emitting diodes from partially conjugated poly(*p*-phenylene vinylene). Journal of Applied Physics, **73**, 5177–5180 (1993).
DOI: 10.1063/1.353794